Challenge Journal of STRUCTURAL MECHANICS

Vol.4 No.4 (2018)

buckling building codes columns continuous girder bridge durability dynamic analysis dynamic response earthquake finite element analysis finite element method meridional stresses operational modal analysis optimization reinforced concrete seismic analysis seismic design seismic isolation seismic response shallow foundations smart concrete teaching-learning based optimization

ISSN 2149-8024

TULPAR ACADEMIC PUBLISHING

Challenge Journal of Structural Mechanics

E-mail: *cjsmec@challengejournal.com*

Web page: *cjsmec.challengejournal.com*

TULPAR Academic Publishing
www.tulparpublishing.com

Challenge Journal of Structural Mechanics

CONTENTS

Research Articles

TULPAR ACADEMIC PUBLISHING

Challenge Journal of Structural Mechanics

Research Article

An insight into design of prefabricated and prestressed concrete monoblock railway ties for service loads

Niyazi Özgür Bezgin *

Department of Civil Engineering, İstanbul University-Cerrahpaşa, 34320 İstanbul, Turkey

ABSTRACT

Ballasted railway track ties support the wheel forces of a train that are transferred onto them by the rails, maintain the track gauge and provide lateral and longitudinal track stability. Prestressed concrete ties provide the required track bearing to the applied wheel loads and constitute a major part of the track self-weight. Design of prestressed concrete ties involves an evaluation of their structural interaction with the ballast and an understanding of prestressed concrete design for service loads and beyond-service loads. This paper aims to provide an insight for the design of a prestressed concrete ballasted railway tie under service loads and highlight the genuine qualities of tie design in terms geotechnical engineering, materials engineering and structural engineering. Through the analysis of a finite element model, this paper presents estimations for bending moment values under service conditions for a prestressed concrete high-speed railway tie under varying track support conditions. The paper then compares the estimated values with those suggested by the relevant design guidelines for railway ties.

ARTICLE INFO

Article history:
Received 1 June 2018
Revised 8 September 2018
Accepted 25 September 2018

Keywords:
High-speed railways
Prefabrication
Prestressing
Monoblock railway ties
Finite element method
Soil-structure interaction
Service load design

1. Introduction

Modern guided ways for trains provide service through ballasted railway tracks, railway slab tracks, monorails and more recently, the maglev tracks and the hyperloop. The first three types of tracks rely on the adhesion between track rail and train wheel for motion whereas the maglev relies on the magnetic field between the levitating electrified trains over the electrified track exposed to open air. The hyperloop also relies on magnetic levitation where the guided motion takes place in a vacuumed tube. However, maglev tracks are yet to achieve design maturity and economic viability whereas the hyperloop is in early stages of research and development. Albeit their higher initial construction costs compared to ballasted tracks, increasing uses of slab-track railways through tunnels, over the bridges and along railway routes with frequent high-speed railway service, provide weight and structural gauge reduction and reduced maintenance costs (Lichtberger, 2011).

Ballasted railway tracks with monoblock concrete ties, which are the highlight of this paper, currently provide an economical and a reliable solution to most railway transportation needs today. Fig. 1 that is modified by the author to show the sloping subballast layer for drainage, shows a common cross-section of a single ballasted track on a fill (Ebrahimi et al., 2011). Ballasted railway track superstructure consists of rails, elastomeric bearing pads underneath the rails, attachment and bearing elements for rails to ties, the ties that support the rails via bearing on ballast layer, the ballast layer and subballast layer The platform grade achieved by the fill or reached and prepared by the cut constitutes the substructure or the subgrade under which lies the natural or existing ground.

The tie shown in Fig. 1 is a monoblock type of tie. The elastomeric bearing pads between the rails and the concrete tie reduce the bearing stiffness of the steel rails on the concrete tie and reduce the dynamic impact force on the tie depending on their attenuation characteristics. Ties interact with the supporting ballast layer through bearing and bending under vertical loads and shear under lateral loads.

The ballast and the sub-ballast layers consist of aggregates that reduce the bearing pressures exerted by the tie

* *Corresponding author*. Tel.: +90-212-4737070 ; E-mail address: ozgur.bezgin@istanbul.edu.tr (N. Ö. Bezgin)
ISSN: 2149-8024 / DOI: https://doi.org/10.20528/cjsmec.2018.04.001

to pressure values allowed on the subgrade. The sub-ballast has the primary duties of providing drainage and filtering for the ballast layer above and frost protection for the subgrade below in addition to their added benefit for reducing bearing pressures on the subgrade (Navikas et al., 2016).

Contemporary railway tracks have performance requirements with respect to service speeds and service loads. International Union of Railways (UIC) recommends track design values for member and affiliated states. Table 1 presents the static design axle loads and train speeds for modern railway tracks (UIC-713R, 2004).

This study concentrates on the evaluation of the design bending moments for the tie under ordinary service load conditions. A finite element model developed for the analysis of the tie under the pseudo-dynamic action of the service loads provides an estimate for the required design bending moments under service loads and the prestressing force required to maintain the stress values at acceptable levels under the service load condition. The study provides a comparison of the UIC service design recommendations with the estimates obtained from the finite element analysis.

Table 1. Combined axle forces and train speeds.

	Static axle force (kN)		
Speed (km/h)	180	225	250
120	♦	♦	♦
200	♦	♦	None
300	♦	None	None

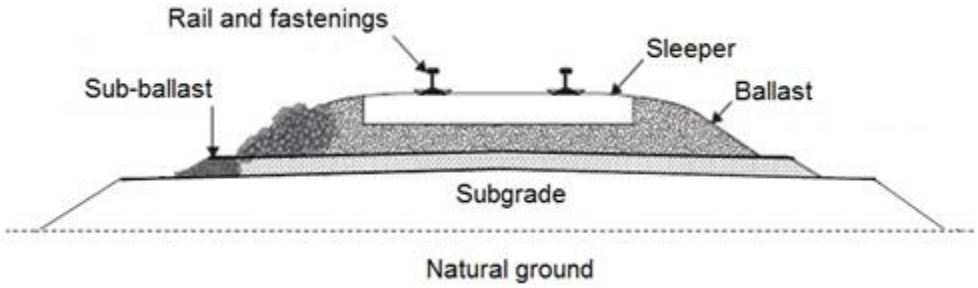

Fig. 1. Cross-section of a single ballasted track on a fill (Modified from Ebrahimi et al., 2011).

2. Prestressed Concrete Ties

Following their introduction in 1950's, many countries developed their unique geometric designs of prefabricated high performance concrete ties. For instance in Germany, concrete ties has unique notations such as B58, B70, B90 and B07 where the letter B denotes the word "beton" and the last two digits signifies the last two digits of their year of introduction (Kerr, 2003). A prestressed monoblock tie shown in Fig. 2 has a length of 2600 mm and an approximate mass of 290 kg. C60 grade concrete and an initial prestressing load of 350 kN under very low design humidity conditions that result in 30% prestress losses, provide the sufficient strength and stiffness for the stresses that occur under a design axle force of 225 kN and a design speed of 250 km/hour.

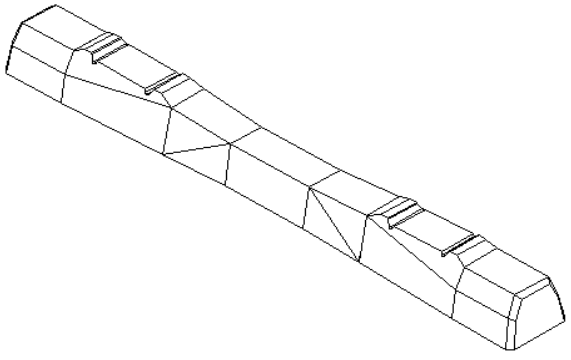

Fig. 2. Perspective view of a prestressed monoblock tie.

Along with bending moment strengths of the tie at the rail seat section and the central section, the ties must have sufficient mass to provide lateral track stability against track buckling and lateral axle loads at curvatures. The tie mass is approximately 2.5 times higher than a creosote infused pinewood tie. The self-weight of the track and the embedment within the ballast layer provides lateral resistance against buckling and lateral forces. A heavier track provides a more stable guide-way for high-speed travel and improves the lateral resistance against track buckling (Kish and Samawedam, 1991).

3. Estimation of Design Moment Values through Finite Element Analysis

Analysis and design of a prestressed concrete tie under vertical wheel forces requires a soil-structure interaction analysis of an axially prestressed non-prismatic concrete element bearing on a ballast layer under the vertical axle loads of a railway vehicle. The first step in the tie analysis is the determination of the distribution of the wheel forces on the ties by the rails followed by an analysis of the bearing stress distribution along the tie base that influence the magnitude and the variation of the bending moments along the tie. Design of the ties must also take into account environmental issues such as seasonal ambient relative humidity values as they heavily influence the effective prestressing force values that remain in the tie in time (Bezgin, 2015). The following sections highlight these issues in detail.

4. Wheel Load Transfer

Rails transfer the vertical forces from the wheels to the ties. Fig. 3 shows a profile sketch of a ballasted railway on a fill. The wheel positioned on the rail right above a tie does not transfer its full vertical load on the tie directly below but transfers parts of the vertical load to the ties neighbouring the centre tie through the bending stiffness of the rail with respect to the compressive stiffness of the supporting ballasted track.

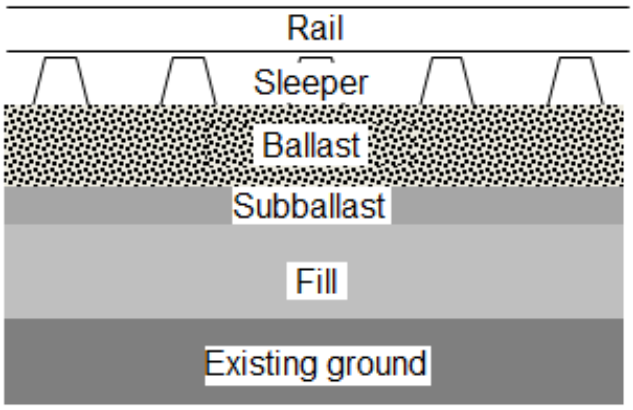

Fig. 3. Profile of a ballasted railway superstructure and substructure on a fill.

For a given combined stiffness of ballast, sub-ballast and subgrade, the transferred amounts of vertical wheel load relates to the bending stiffness (K) of the rail, which directly relates to the bending rigidity of the rail (EI) and inversely relates to the centerline spacing of the ties (L). An increase in the value of L for a given rail rigidity lowers the bending stiffness of the rail, which results in a lower amount of load transfer to neighbouring ties. For a given L and E value, the reduced moment of inertia of a shallower rail also lowers its bending stiffness.

A UIC-60 type rail is 172 mm deep and 150 mm wide at its base. It has a cross-sectional area of 76.7 cm^2, moment of inertia of 3038.3 cm^4 and a mass of 60.2 kg/m (EN 13674, 2002). Existing research indicates that for a UIC-60 type rail supported by ties positioned at 60 cm center-to-center, the wheel loads transfer such that the center-tie that is immediately under the acting wheel receives 50% of the wheel load and the left and right ties neighboring the center tie receive 25% of the wheel loads respectively. Figure 4 shows a two-dimensional linear-elastic model of a UIC-60 rail supported by ties spaced at 60 cm center to center spacing. The static wheel force acting on the rail is 122.5 kN or 12.5 Ton-f, representing the wheel force of a freight train. The coefficient of subgrade reaction (C) for the ballast supporting the ties is 0.3 N/mm^3 representing a newly laid and tamped typical ballasted track.

Fig. 5 shows the developed reactions under the ties in units of kg-f. The tie immediately under the acting wheel load provides a reacting force of 58 kN, which is approximately 48% of the acting wheel force and the neighbouring ties provide about 31 kN reactive force each, which are 26% of the acting wheel force. Therefore, the results of the static analysis of the linear-elastic model presented in Fig. 4 shows that with the given configuration, an estimation of 50% of the wheel load for the heaviest loading on the tie is acceptable.

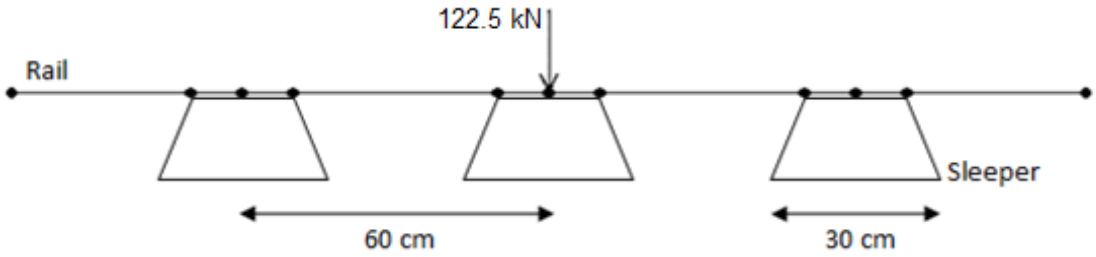

Fig. 4. Two-dimensional load distribution model (ballast support not shown).

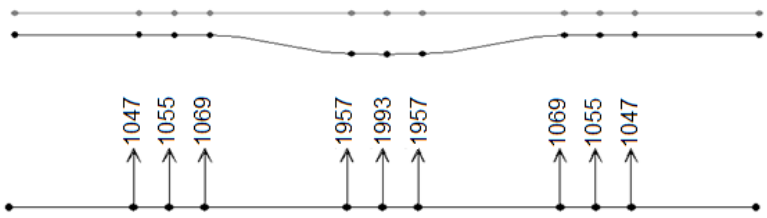

Fig. 5. Reaction distributions under the ties.

One can deduct from the above analysis that wheel load transfer varies by varying tie spacing and/or the section properties of the rail. Theoretically, if the rail had zero bending stiffness, that is to say if the rail was infinitely flexible, the acting wheel load on the rail would completely act onto the tie immediately below. At the other theoretical extreme, if the rail was infinitely stiff compared to the combined stiffness of the track elements below, all three ties in this model would settle the same amount under the acting wheel load and thus each would share one third of the acting wheel load.

5. Bearing Stress and Bending Moment Distribution along the Tie

Upon estimating the transferred maximum value of the wheel load acting on a tie, one needs to investigate the distribution of bearing pressures under the tie and bending moment values along the length of the tie under different bearing conditions. The coefficient of subgrade reaction (C) of a supporting granular medium is a fundamental parameter that influences the amount of settlement in the medium, which occurs under an acting pressure. This coefficient is also an indicator of the compressive stiffness of the granular medium. Based on extensive test data on existing tracks, a properly tamped and stabilized ballast layer of a new track can provide a C value as high as 0.3 N/mm³ (MPa/mm) (Lichtberger, 2005; Ebrahimi et al., 2015). A weakened ballast layer due to infiltration of thin granular materials, known as fouled ballast can be as low as 0.02 N/mm³ (MPa/mm) (Ebrahimi et al., 2015). Distribution of bearing pressures and bending moments relates to the compressive stiffness of the ballast layer, the bending stiffness of the prestressed concrete tie and their relative value.

Fig. 6 shows the perspective and top views of finite element model of the tie that is 260 cm long. The width of the tie at its base varies from 30 cm at the ends to 22 cm at the tie centre. The depth of the tie varies from 21.5 cm at the rail seat to 17.5 cm at the tie centre. The meshing includes 45 layers along the length of the tie, 5 layers along the width of the tie and 10 layers along the depth of the tie that amounts to a finite element model with 2250 elements. The model generated by SAP2000® is a linear-elastic model. The tie rests on a ballasted track represented by linear-elastic vertical springs. The bottom view of the tie shows the linear-elastic springs attached to the base nodes of the tie. The solid elements that generate the model are 8-node solid elements. The number of layers along the depth of the tie is selected to prevent the occurrence of the phenomenon known as shear-locking observed in finite element models built with 8-node solid elements.

Design modulus of elasticity (E) for the tie is E=38,000 MPa for a minimum C60 grade concrete produced with hard limestone aggregate. The high strength is necessary in order to provide sufficient early strength for prestressing transfer into the tie. The method of introducing prestressing forces into the tie is using end-bearing plates attached to the prestressing wires by cold-formed buttoning of the wires to the plates. It is important to note that the concrete elastic modulus is very important in prestressed concrete design and varies with the type of aggregate for a given class of concrete. The cross-sectional area along the tie length is variable and the cross section area at the rail seat is A_1 = 555 cm² and the cross section area at the tie centre is A_2 = 333 cm². Moment of inertia of the tie cross section area is variable along the tie axis of symmetry and varies from I_r = 15,724 cm⁴ at the rail seat to I_c = 8,465 cm⁴ the tie centre.

Multiple counts of finite element analysis of this tie under 225 kN static axle force distributed by 50% on to the tie by the rails took place over supporting ballast layers with varying coefficient of subgrade reaction values of C = 0.02, 0.05, 0.1, 0.2, 0.3 and 0.4 MPa/mm. The lower bound of these values represents highly fouled ballast bed and the upper bound selected by the author to represent a new ballast bed of granite aggregates with full aggregate interlock. The multiple analyses under the wheel forces transferred by the rails yielded bearing pressure values and bending moment values along the 260 cm length of the tie determined at 26 data points. Figs. 7 and 8 present the respective analyses results for C = 0.02, 0.1, 0.2 and 0.4 MPa/mm.

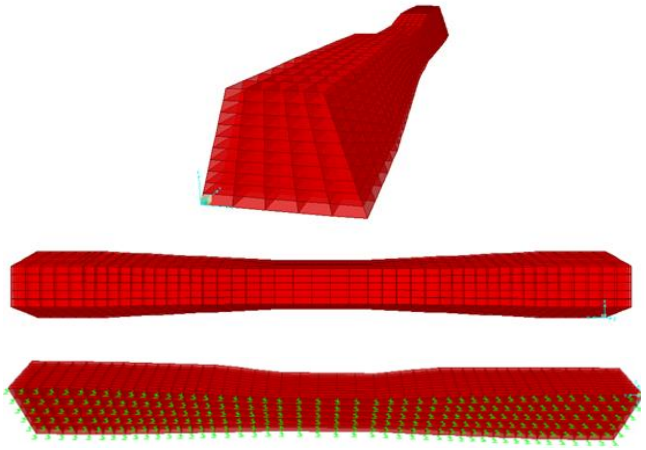

Fig. 6. Perspective views and plan of finite element model of the tie.

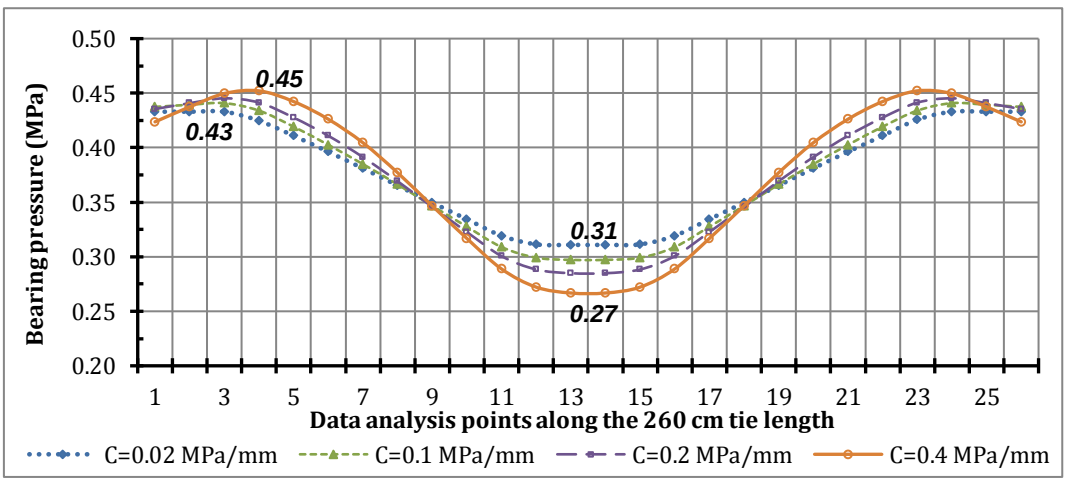

Fig. 7. Pressure variations under ties on ballast layers with varying C values.

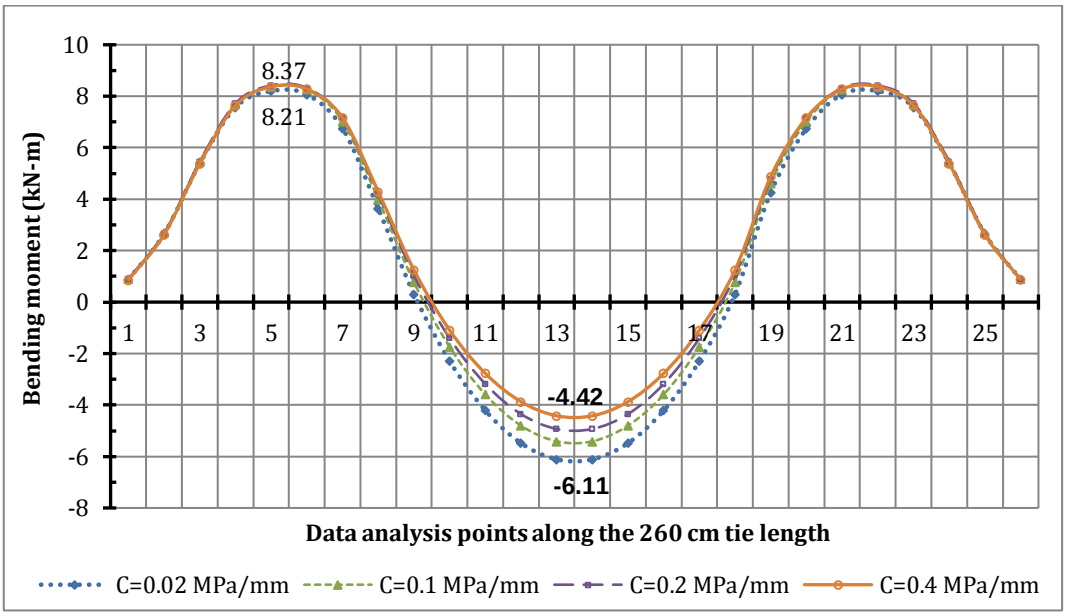

Fig. 8. Bending moments along ties bearing on ballast layers with varying C values.

For a given type of tie, variation of the compressive stiffness of the ballast layer for different coefficient of subgrade reaction values influences the distribution of the ballast bearing pressure and bending moment along the tie. For a given tie bending stiffness, as the compressive stiffness of the supporting layer increases the relative stiffness of the tie with respect to the supporting layer decreases. Therefore, the bearing pressure distribution along the bottom of the tie concentrates and increases along the regions that are under the rails and decreases at the center of the tie. One can think of a theoretical case where the bending stiffness of the tie is negligible and the tie rests on an infinitely rigid ballast layer. Under such conditions, the reactive forces to the acting rail forces on the tie will concentrate right under the rails. However, as the compressive stiffness of the ballast decrease and the relative stiffness ratio of the tie with respect to the ballast increase, the bearing pressures does not concentrate under the rails and increase in the center of the tie and tend to distribute more evenly along the tie. Figs. 7 and 8 clearly show this behavioral tendency for ties under a fixed value of distributed wheel forces supported by ballast layers with varying stiffness values. When the coefficient of subgrade reaction changes from C=0.4 MPa/mm to C=0.02 MPa/mm, the maximum bearing pressure at the middle of the tie increases roughly 13% and maximum bearing pressure at the rail seat regions decrease roughly 4.5%.

Variation of the bending moment also changes with the bearing stress distribution. For the mentioned change of the coefficient of subgrade reaction, the bending moment at the tie center increases roughly 38% whereas the rail seat moments decreases 2%. The effects of the variation of bearing stress values at the tie centre and the rail seats on the bending moment values at the respective locations are not the same due to varying moment of inertia values of the tie cross section area between the rail seat and the tie centre. Fig. 9 shows the variation of the highest rail seat (M_r^+) and tie center (M_c^-) bending moment values along the tie with increasing values of coefficient of subgrade reaction from typical low levels to high levels encountered in practice. With increasing ballast layer stiffness, the tie center moment values reduce profoundly and and the rail seat bending moment values increase slightly.

Previous analytical findings show that for a given tie material and geometry, tie response relates to the stiffness of the supporting granular medium. Determination of stresses due to tie bending under axle loads requires a definition of the support conditions. Table 2 summarizes the findings presented in Fig. 9 and shows the sensitivity of the bending moments at the rail seat and the tie center to coefficient of subgrade reaction of the track. The normalized values are with respective to C=0.02 kN/mm^3 and the related moment values.

One can see with these results that there is a practical limit to track stiffness. Decreased C values increase the bending moment values at the tie centre profoundly and they have a negligible effect on the bending moment values at the rail seat. However, increasing the C values beyond C=0.3 kN/mm^3 does not produce a substantial benefit with respect to the reduction of bending moments at the tie centre.

Within the analysis range for varying coefficient of subgrade values, the underlined highest tie centre moment in Table 2 is M_c^-max=6.11 kN-m which occurs for the low value of C=0.02 MPa/mm. The underlined highest rail seat moment is M_r^+max =8.44 kN-m which occurs for the high value of C=0.4 MPa/mm. Tie design must account for possible variations in the ballast support conditions and must therefore consider the maximum bending moment values that may occur as a result of these variations. The presented analysis results based on the moment envelope indicates a ratio of maximum moments M_r^+max / M_c^-max ~ 1.38 for the tie.

The next section introduces a stress analysis of a tie through a finite element model. The ballast support conditions for the tie is C=0.3 MPa/mm, which is a representative value of a newly constructed and consolidated track.

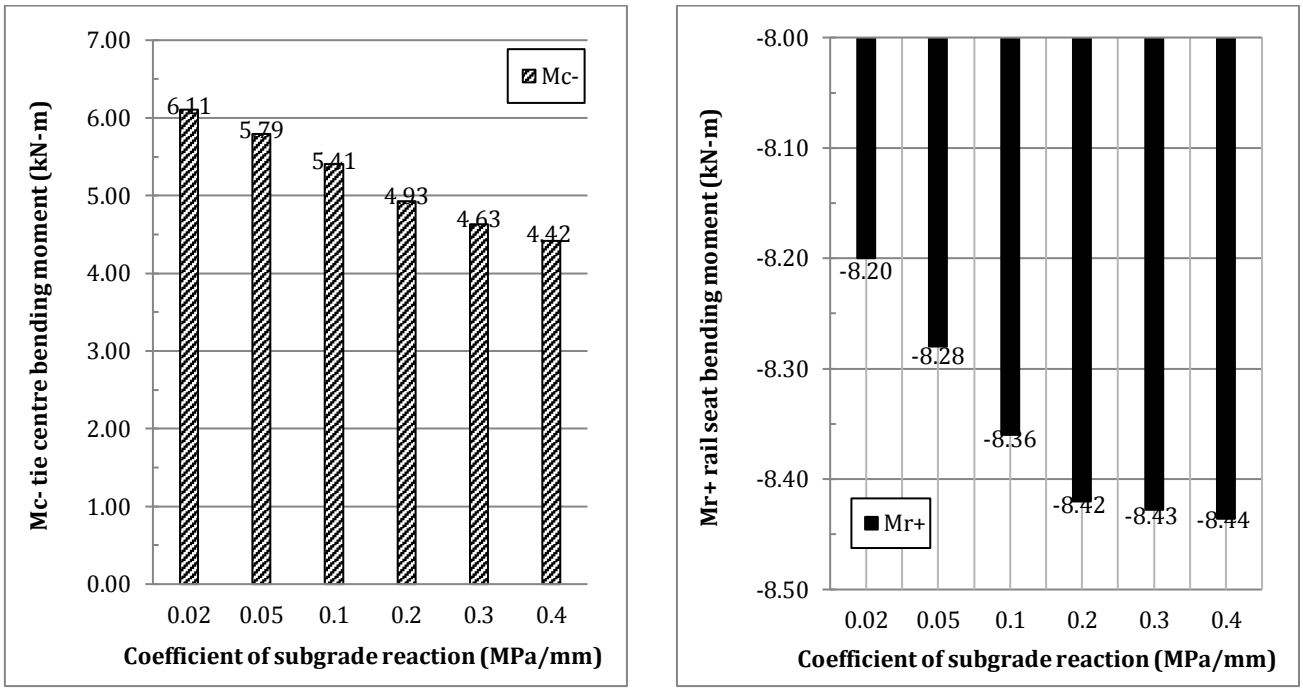

Fig. 9. Variation of maximum rail seat (M_r^+) and tie centre (M_c^-) moment values with C.

Table 2. Tabulation of bending moment values with respect to varying coefficient of subgrade reaction values.

C (kN/mm³)	M_c^- (kN-m)	M_r^+ (kN-m)	$C_{\text{normalized}}$	$M_c^-{}_{\text{normalized}}$	$M_r^+{}_{\text{normalized}}$
0.02	-6.11	+8.20	1.0	1.000	1.000
0.05	-5.79	+8.28	2.5	0.948	1.010
0.1	-5.41	+8.36	5.0	0.885	1.020
0.2	-4.93	+8.42	10.0	0.807	1.027
0.3	-4.63	+8.43	15.0	0.758	1.028
0.4	-4.42	+8.44	20.0	0.723	1.029

6. Stress Analysis of the Tie through a Finite Element Model with respect to Design Conditions

Tie design requires the determination of the location of the prestressing wires in the tie and the value of the prestressing force. The static design axle force on the tie supported over a newly consolidated stiff ballast layer with a design coefficient of subgrade reaction value of C=0.3MPa/mm is Q_{0s}=225 kN.

The static value of the axle force increases due to motion of the train and the unavoidable vertical irregularities along the track caused by the variations in track profile and/or track stiffness. Numerous procedures estimate the possible dynamic impact forces of the moving train wheels on the track and the supporting ties (AREMA, 2006; Bezgin, 2017, 2018). These procedures approach the problem through the interaction of the wheels of a speeding train with the irregularities of the track due to settlements and stiffness variations along the track and with the stiffness and damping properties of the wheel and bogie configuration of the train. All of these procedures may assist the designer to estimate the dynamic axle loads of a moving train on the track. Upon a thorough consideration of the existing approaches, the designer of the presented tie elected to use a conservative dynamic load estimation procedure based on train speed and wheel diameter, which yielded the highest dynamic load estimate. The design speed (v) and wheel diameter (D) of the train is 250 km/h and 920 mm respectively. Eq. (1) empirically presents the dynamic axle load coefficient (ø) based on the estimation by the American Railway and Maintenance Right of Way (AREMA).

$$\emptyset = \left(1 + 5.21\frac{v}{D}\right) = \left(1 + 5.21\frac{250}{920}\right) = 2.4\,. \quad (1)$$

Eq. (2) presents the design service dynamic axle force on the rail supported by the tie:

$$Q_{0d} = Q_{0s} \cdot \emptyset = 225 \cdot 2.4 = 540 \text{ kN}\,. \quad (2)$$

The distributed value of the axle force on the supporting tie is 270 kN, based on a distribution factor of 50% confirmed earlier. Depending on its characteristics, the elastomeric bearing pad between the rail and the tie reduces the transferred dynamic wheel load by the rail onto the tie. The elastomeric bearing pad is an important component of railway superstructure and thus an important

analytical parameter on its own, and therefore the following finite element model excludes the bearing pad to remove a parameter that affects the analysis.

The fundamental design requirement for the tie behaviour under design service loads is to remain uncracked under bending. The finite element model generated by the solid elements and analyzed by the elastic un-cracked analytic capability of the SAP 2000® program determined the bending stresses for the tie under service load conditions. The tensile bending stresses formed the basis for the introduction of the prestressing forces and determination of the prestressing force value. Under the combined action of the 270 kN axle force on the rails, distributed to the tie, tensile stresses occur along the tie bottom underneath the rails and the tie top face at the tie centre. Fig. 10 highlights the tensile bending stresses.

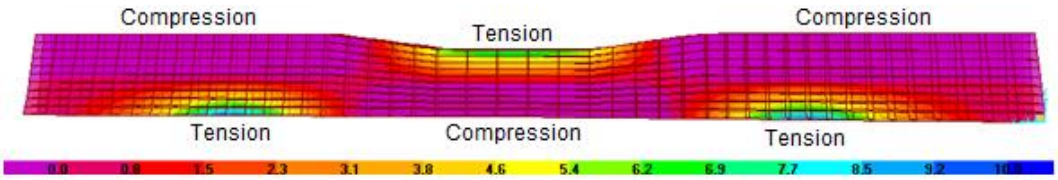

Fig. 10. Tensile and compressive stresses within the tie under 122.5 kN axle force.

Flexural tensile stress values vary from 5 MPa at the top surface of the tie middle to approximately 7 MPa at the tie bottoms under the rail seats, which would crack the C60 grade concrete with a characteristic flexural tensile strength value of 4.3 MPa. Therefore, the prevention or the limitation of these bending stresses is the reason for introducing prestressing forces into the tie.

Fig. 11 conceptually presents the application of the initial prestressing force (P_i) longitudinally into the tie through the center of the force and the longitudinal tie contraction. The tie contracts approximately 0.5 mm under the 350 kN initial prestressing force generating compressive longitudinal stresses along the length of the tie. The compressive stresses vary up to 10 MPa at the tie center, 7 MPa at the rails seats and 12 MPa to 33 MPa at the tie ends. In the particular case, bearing plates anchored into the tie ends introduces the 350 kN prestressing force into the tie generating a bearing stress of approximately 33 MPa. The design and selection process for the anchor plates is the subject of another study. Fig. 12 presents the cross section view of the tie section at the tie ends where the end-bearing plates introduce the prestressing forces into the tie by the BBRV system (plates not shown). BBRV stand for the initials of the last names of the developers “Brandestini, Birkenmaier, Ros and Vogt” who developed the system in the early 1960’s.

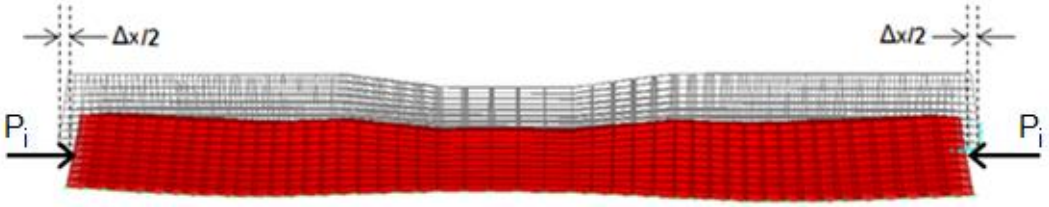

Fig. 11. Longitudinal prestressing force on the tie.

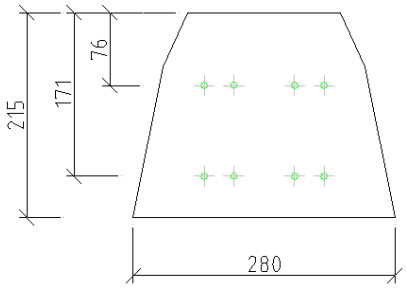

Fig. 12. Placement of prestressing wires within the ties.

Under service conditions, the joint action of the horizontal prestressing forces and vertical forces on the tie, induces bending around the lateral axis and compression along the longitudinal axis of the tie. Fig. 13 shows the resultant longitudinal compressive stresses due to bending and axial compression.

The joint action of 350 kN prestressing force and 270 kN vertical axle force induces longitudinal compressive stresses along the tie length varying up to 20 MPa. Fig. 13 shows that the 350 kN prestressing force diminishes the tensile longitudinal stresses.

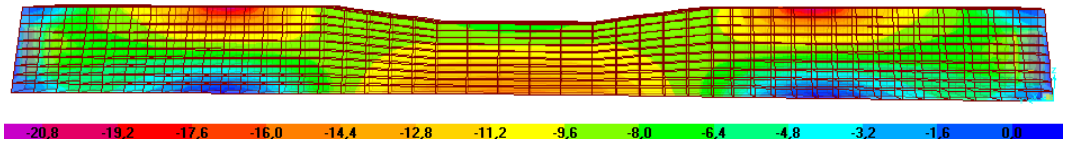

Fig. 13. Compressive stress distributions along tie due to axle and prestressing loads.

High strength prestressing strands with characteristic tensile strength f_{pk} = 1860 MPa with 0.1% proof stress of $f_{p0.1k}$ = 1290 MPa and 1% elongation stress of $f_{p1.0k}$ = 1440 MPa support the design prestressing force of P_i = 350 kN. The allowable tensile prestressing stress is the smaller of $0.9f_{p0.1k}$ = 1160 MPa or $0.8f_{p1.0k}$ = 1152 MPa. Eq. (3) shows the total prestressing area requirement.

$$A_{ts} = {P_i}/{0.8f_{p1.0k}} = 303 \text{ mm}^2 . \quad (3)$$

A steel strand with 7-mm diameter has an area of A_s = 38.4 mm². Eq. (4) shows the total number of strands needed to provide an initial prestressing force of P_i = 350 kN to the tie.

$$n = \frac{A_{ts}}{A_s} = \frac{303}{38.4} = 7.9 = 8 . \quad (4)$$

However, the introduced value of the initial prestressing into the tie does not remain constant but decrease in time due to elastic shortening of the tie with the prestressing, shrinkage and creep effects of concrete and the stress relaxation of the prestressing steel. Therefore, the designer must take into account the effective prestressing force that remains in the tie and gauge the occurrence of longitudinal tensile stresses in time. This particular design considered the performance of the tie under extreme dry conditions with a predicted prestress loss of 30% (Bezgin, 2015). The estimation of the prestress loss is the subject of another study.

7. Specification of Design Bending Moment Values for Ties under Service Conditions

The study presented up to this point summarizes the depth and extent of interactions of multiple parameters that are effective in the design of a railway tie under the action of service-level axle forces. The designer can reflect his or her understanding of the design requirements on the design of the tie in many ways with differing levels and depths of expertize. Understanding and estimation of the ballast support magnitudes and distributions, time dependent losses, axle forces and dynamic force estimations are dependent on the designer and different designs are possible for a given train speed and axle force.

However, a railway network consists of many individual routes. In today's world, transportation is a global matter extending beyond national borders. Therefore, differing designs between routes based on individual estimations of design parameters may generate railway lines with varying structural characteristics. These structural variations may limit service rate and service speed within or across networks and may generate difficulties in planning a track maintenance schedule. Such being the case, in order to provide a seamless integration of networks to the best extent possible, a cooperative approach among nations resulted with the formation of a Union of International Railways (UIC) with the aim of providing a common understanding of a design basis of railway tracks. Therefore, a unified methodology to determine tie design values is useful. The following subsections introduce the UIC-713R approach to estimate the tie design values for service level.

8. Service Load Design Values for the Ties

The design speed for the tie studies in this paper is 250 km/hour and its design static axle force is 225 kN. These values are typical in many countries in Europe, Turkey and the Middle East. Minimum ballast depth of the ballasted track is 350 mm and sub-ballast depth is 200 mm. Tie spacing with respect to their centers is 60 cm. Design track includes UIC-60 type rails with 60 kg/m mass and 172 mm depth. Tie service life is 40-years. The subsequent sections will present the dynamic axle loads and the related design moment values based on the UIC-713R suggestions.

8.1. Design axle force

Design moment values constitute the basis for tie design. The first set of design moment values are the ones that occur under ordinary service conditions. Service conditions relates to estimated rail support and track conditions. Eq. (5) relates the dynamic wheel load to static wheel load amplified by factors that reflect train speed and track conditions.

$$P_d = \frac{Q_0}{2}\left(1 + g_p . g_v\right) . g_d . g_r . g_i . \quad (5)$$

In the equation above, Q_0 = Static axle force, g_p = Impact attenuation factor by the bearing pad, g_v = Speed factor, g_d = Load distribution factor, g_r =Tie reaction variation factor due to support faults, g_i =Tie bottom irregularity factor. Impact attenuation factor relates to the characteristics of the elastomeric pads situated between the rails and the tie that reduce the impact of the rail onto the tie. Elasticity modulus of C60 grade high strength concrete used in this study is up to 6 times higher than the elasticity modulus of pinewood ties. Unlike the transition between a steel rail and wooden tie, the transition between a steel rail and high performance concrete tie is much stiffer due to higher stiffness of the concrete. Therefore, elastomeric pads reduce the magnitude of the

dynamic loads transferred from the steel rail to the concrete tie. Load distribution factor relates to the spacing of the ties and the attached rail bending rigidity and determines the percentage of the wheel force resisted by the tie underneath the wheel. Tie irregularity factor reflects possible production irregularities at the tie bottom that may amplify the applied loads.

The design values are: Q_0 = 225 kN, g_p = 1.0 for low attenuation, 0.89 for medium attenuation and 0.78 for high attenuation, g_v = 0.75, g_d = 0.5, g_r =1.35, g_i = 1.6. Eqs. (6) and (7) show the service level dynamic design wheel forces on ties supporting rails with medium impact attenuation and low impact attenuation elastomeric rail support pads, respectively.

$$P_{d-medium} = \frac{225}{2}\left(1 + 0.75 \cdot 0.89\right) \cdot 0.5 \cdot 1.35 \cdot 1.6 = 203 \text{ kN}, \quad (6)$$

$$P_{d-low} = \frac{225}{2}\left(1 + 0.75 \cdot 1.0\right) \cdot 0.5 \cdot 1.35 \cdot 1.6 = 213 \text{ kN}. \quad (7)$$

The dynamic estimate of the wheel force is 80% higher than the static wheel force for medium attenuated wheel forces and 90% higher for un-attenuated wheel forces. The particular design in this study included medium-attenuated bearing pad, the following section includes their force reducing effects.

8.2. Design moment values for service loads

Design dynamic service moment value relates to the dynamic wheel design forces determined in the previous section and the estimated support condition. Fig. 14 shows a proposed support condition that ignores the bearing pressure along the tie central region and considers the ballast bearing pressure underneath the rail seat uniformly distributing along to both sides of the rail seat. This reflects a reasonable consideration where most of the ballast support concentrates underneath the rail seats for a newly tamped track.

Fig. 15 shows half of the free body diagram of the rail seat region of the tie, hypothetically detached from its bearing pressure free central part. L_p is the distance between the rail seat central line and the tie end. Distance "e" considers the concrete confinement effect underneath the rail, thereby reducing the effective moment arm (L_e) with respect to the rail seat as, $L_e = L_p - e$. For a B70 type tie, L_p = 55 cm and for a UIC Type 60 rail bearing on the tie, e = 18 cm.

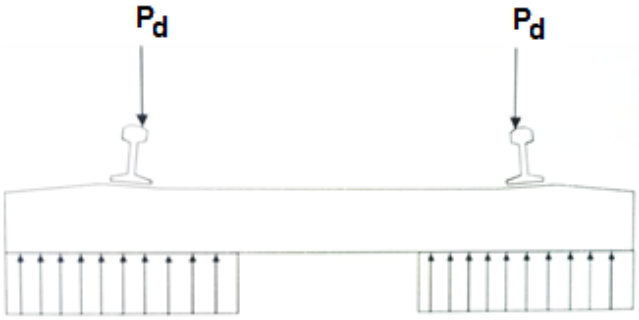

Fig. 14. Assumed ballast bearing pressure distribution underneath the tie (UIC-713R, 2004).

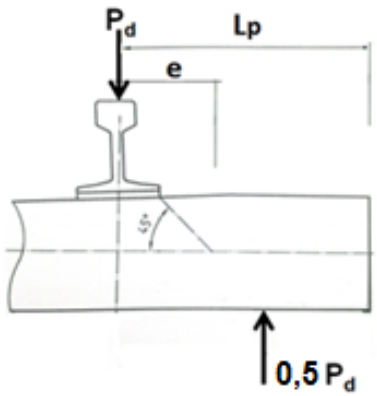

Fig. 15. Assumed ballast bearing pressure distribution underneath the tie (UIC-713R, 2004).

Eq. (8) relates the positive rail seat design bending moment under ordinary service conditions to the resultant ballast bearing force.

$$M_{dr}^{+} = P_d\left(\frac{L_p - e}{4}\right) = 203 \cdot \left(\frac{0.55 - 0.18}{4}\right) = 18.75 \text{ kNm}. \quad (8)$$

Based on the tie deformation shown in Fig. 3, the negative design bending moment at the tie center relates to the positive rail seat design bending moment and the ratio of the moment of inertia values of the tie central cross section and the rail seat cross section of the tie through Eq. (9).

$$M_{dc}^{-} \sim 1{,}2 . M_{dr}^{+} \, {}^{I_c}/_{I_r}. \quad (9)$$

I_c and I_r are the moment of inertial values of the tie cross section at the tie center and at rail seats. Fig. 16 shows the longitudinal perspective of the 2600 mm long tie with its cross section dimensions at the rail seats and the middle of the tie.

The moment of inertia values of the tie at cross section A and B are I_r = 15,724 cm^4 and I_c = 8,465 cm^4 respectively. The ratio of the moment of respective moment of inertia values is 0.54 and the tie center negative design bending moment is determined in Eq. (10).

$$M_{dc}^{-} = 1.2 \cdot 18.75 \cdot 0.54 = 12.25 \text{ kNm}. \quad (10)$$

The positive sign for the moment at the rail seat signifies that the tie bottom at the rail seat is under tension. The negative sign for the moment at tie centre signifies that the tie bottom at the middle part of the tie is under compression.

An interesting finding through the estimated service values of maximum design bending moment service values is that the ratio of maximum design moments based on the UIC guidelines is $M_{dr}^{+}\text{max} / M_{dc}^{-}\text{max} \sim 1.53$, which is quite comparable to the ratio of maximum moments found earlier with the finite element analysis as $M_{r}^{+}\text{max} / M_{c}^{-}\text{max} \sim 1.38$. In other words, although UIC basis its tie design on a newly tamped track, it also accounts for the moment envelope bound by the possible variation of the ballast support stiffness and increased bending moments at the tie centre due to weakened ballast support.

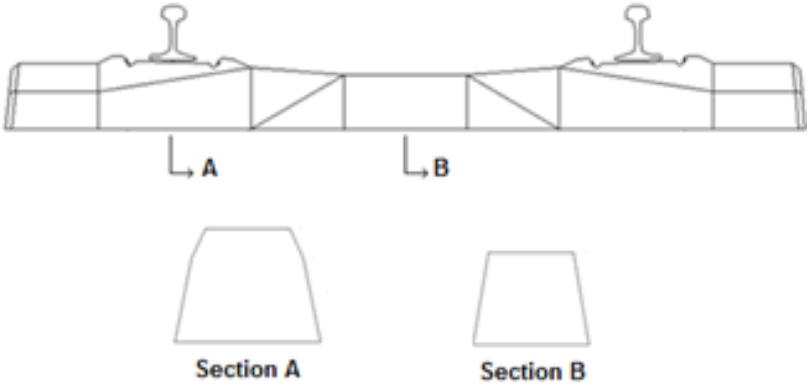

Fig. 16. Longitudinal profile and cross-section dimensions of the tie in mm.

One other useful finding is the comparison of the design service moment values found according to the UIC-713R with respect to findings based on an individually executed finite element analysis earlier and presented in Table 2. Unlike the UIC approach, the finite element approach in did not include the dynamic factor attenuation factor to account for the elastomeric bearing pads. In other words, the maximum design bending values included only the static value of the wheel forces. Therefore, in order to compare the results estimated by the two approaches, one must determine the static values of the M_{dr}^{+} and M_{dc}^{-} suggested by the UIC method.

Table 3 summarizes and compares the maximum static rail seat and tie centre design service moment values based on the two approaches. The static estimates of the two approaches for the rail seat and tie centre moment values are similar. The FEM estimates for the rail seat moment and the tie centre moments are respectively 85% and 95% of the UIC estimates. The lower aggrement for the rail seat moments is due to the fact that the finite element method approach considers a variable soil bearing pressure underneath the tie along rail seat whereas the UIC method assumes a constant bearing pressure at its maximum value.

Table 3. Comparison of static design service bending moment values of UIC and the FEM.

		UIC-713R estimates		FEM estimates		% ratio of FEM/UIC estimates
		Dynamic design moment (kN-m)	Load factor	Static design moment (kN-m)	Static design moment (kN-m)	
Tie rail seat moment	M_{dr}^{+}	18.75	1.90	9.87	8.44	85%
Tie centre moment	M_{dc}^{-}	12.25	1.90	6.45	6.11	95%
Moment ratio	M_{dr}^{+}/M_{dc}^{-}	1.53	-	1.53	1.38	90%

9. Conclusions

This paper presented an insight into the service load design of prestressed concrete high-speed railway ties. The first part presented the distribution of wheel loads to the ties and the variation of bending moments along a tie supported on ballast layers with different coefficient of subgrade reaction values. Determination of the required prestressing force for a tie under certain wheel loads and support conditions commenced. The study then compared the analytically estimated design moment values for the service load conditions to the values suggested by the UIC. The following list summarizes the numeric findings and recommendations resulting from this study.

- The maximum percentage of the wheel load transferred to a ties spaced at 60 cm center-to-center through a supporting a UIC-60 type rail is 48%, which confirms the existing recommendation of maximum wheel load transfer percentage of 50%.

- The sensitivity of the design moment value of the tie centre to ballast support conditions is higher than the rail seat due to a distinct variation of the ballast support bearing pressure distribution along the tie centre with varying coefficient of subgrade reaction.
- Tie centre moment linearly varies approximately by 0.22 kN-m and rail seat moment varies approximately by 0.03 kN-m per 0.05 N/mm^3 change in coefficient of subgrade reaction up to a value of 0.2 N/mm^3.
- The sensitivity of bending moment variations along the tie diminish above coefficient of subgrade reaction values above 0.2 N/mm^3.
- Bending analysis conducted on ties supported on ballast layers with coefficient of subgrade reaction values varying from C=0.02 MPa/mm and C=0.4 MPa/mm yielded ballast bearing pressure variations of 13% and 4% for the tie centre and tie rail seat respectively.
- The resultant bending moment variations for the tie centre and tie rail seat was 38% and 2% respectively.
- An overly stiff track bedding producing a coefficient of subgrade reaction beyond C=0.3 kN/mm^3 is unnecessary since the effect of higher C values on the generated moments diminish beyond this value.
- An overly stiff track bedding producing a coefficient of subgrade reaction beyond C=0.3 kN/mm^3 is unnecessary since the effect of higher C values on the generated moments diminish beyond this value.
- The ratio between maximum tie rail seat and tie centre moments based on the finite element analysis is approximately 1.38, which is close to and slightly less conservative than the UIC evaluation of 1.53.
- UIC design moment recommendations for the rail seat and tie centre is respectively 18% and 6% higher than the values obtained by the FEM, indicating estimations that are reasonably more conservative.

REFERENCES

American Railway Engineering and Maintenance of Way Association (2006). Manual for Railway Engineering. AREMA, Volume 1, Chapter 30, Part 1, "Ties – General Considerations".

Bezgin NÖ (2015). Climate effects on the shoulder width measurements of prestressed concrete high speed railway ties of ballasted tracks. *Measurement*, 75, 201–209.

Bezgin NÖ (2017). Development of a new and an explicit analytical equation that estimates the vertical impact loads of a moving train. *Procedia Engineering*, 189, 2-10.

Bezgin NÖ (2018). Proposal of a new analytical method to estimate the vertical impact forces on railway tracks due to changes in track profile and track stiffness. *CETRA 2018*, 837-843.

Ebrahimi A, Tinju MJ, Edil BT (2015). Deformational behavior of fouled railway ballast. *Canadian Geotechnical Journal*, 52(3), 344-355.

EN 13674 (2002). - Railway applications - Track - Rail - Part 1: Vignole railway rails 46 kg/m and above.

Indraratna B, Salim W, Rujikiatkamjorn C (2011). Advanced Rail Geotechnology – Ballasted Track. Taylor and Francis.

International Union of Railways (2004). Design of Monoblock Concrete Ties. UIC CODE, 713 R, 1st Edition.

Kerr A (2003). Fundamental of Railway Track Engineering. Simmons Boardman Pub Co, First Edition.

Kish A, Samavedam G (1991). Dynamic Buckling of Continuous Welded Rail Track: Theory, Tests, and Safety Concepts. Transportation Research Record 1289.

Lichtberger L (2005). Track Compendium: Formation, Permanent Way, Maintenance, Economics. Eurailpress.

Navikas D, Bulevičius M, Sivilevičius H (2016). Determination and evaluation of railway aggregate sub-ballast gradation and other properties variation. *Journal of Civil Engineering and Management*, 22(5), 699-710.

Challenge Journal of Structural Mechanics

Research Article

Monitored structural behavior of a long span cable-stayed bridge under environmental effects

Alemdar Bayraktar [a,*], Ashraf Ashour [b], Halil Karadeniz [c], Altok Kurşun [d], Arif Erdiş [d]

[a] *Department of Civil Engineering, Karadeniz Technical University, 61080 Trabzon, Turkey*
[b] *Department of Civil and Structural Engineering, University of Bradford, Bradford, West Yorkshire BD7 1DP, UK*
[c] *Department of Civil Engineering, İstanbul Esenyurt University, 34510 İstanbul, Turkey*
[d] *Gülsan Inc., Cumhuriyet St. No:22, Beykoz, 34805 İstanbul, Turkey*

ABSTRACT

An accurate numerical analysis of the behavior of long-span cable-stayed bridges under environmental effects is a challenge because of complex, uncertain and varying environmental meteorology. This study aims to investigate in-situ experimental structural behavior of long-span steel cable-stayed bridges under environmental effects such as air temperature and wind using the monitoring data. Nissibi cable-stayed bridge with total length of 610m constructed in the city of Adıyaman, Turkey, in 2015 is chosen for this purpose. Structural behaviors of the main structural elements including deck, towers (pylons) and cables of the selected long span cable-stayed bridge under environmental effects such as air temperature and wind are investigated by using daily monitoring data. The daily variations of cable forces, cable accelerations, pylon accelerations and deck accelerations with air temperature and wind speed are compared using the hottest summer (July 31, 2015) and the coldest winter (January 1, 2016) days data.

ARTICLE INFO

Article history:
Received 6 August 2018
Revised 21 September 2018
Accepted 12 October 2018

Keywords:
Long span cable-stayed bridges
Environmental effects
Temperature effects
Wind effects
Monitoring of bridges

1. Introduction

The number of constructed long span cable-stayed bridges has increased over the last few decades in the World. These bridges have a complicated structural system because their main structural elements including decks, towers (pylons) and main cables have different structural characteristics. The cable-stayed bridges inevitably suffer from traffic loads and even natural disasters, such as earthquakes and typhoons. In addition to, the cable-stayed bridges are subject to daily, seasonally, and annually varying environmental effects such as air temperature, humidity, wind etc. It has been seen that structural behavior of bridges is more significantly affected by environmental thermal effects than by external operational loads (Zhou et al., 2016). Therefore, the importance of the bridge structural monitoring is highlighted during their service life. Because, structural monitoring systems installed on cable-stayed bridges have the potential to generate large data repositories from which a deeper understanding of bridge behavior can be obtained under environmental effects.

Structural health monitoring of bridges using environmental-induced responses has received increasing attention from researchers. Sohn et al. (1999) prepared an experimental study of temperature effect on modal parameters of the Alamosa Canyon Bridge. They indicated that a linear four-input filter to temperature can reproduce the natural variability of the frequencies with respect to time of day. Peeters and De Roeck (2001) implemented one-year monitoring of the Z24 Bridge. Tong et al. (2001) and (2002) investigated temperature distribution and extreme thermal loading and the design temperature profiles for various types of steel bridge deck with different thickness of bituminous surfacing developed. Fujino and Yoshida (2002) investigated wind-induced vibration and control of Trans-Tokyo Bay Crossing Bridge. It was shown that the results from the field

* *Corresponding author*. E-mail address: alemdarbayraktar@gmail.com (A. Bayraktar)
ISSN: 2149-8024 / DOI: https://doi.org/10.20528/cjsmec.2018.04.002

and from the wind tunnel tests are fairly consistent regarding the amplitudes and wind speed range of the vortex-induced vibration in the first vertical vibrational mode of the bridge. Lucas et al. (2003) determined the thermal actions on a steel box girder bridge. Mondal and DeWolf (2007) developed a computer-based system for the temperature monitoring of a post-tensioned segmental concrete box-girder bridge. Li and DeWolf (2007) investigated the effect of temperature on modal variability of a curved concrete bridge under ambient loads. The results of the study showed that the variability of measured modal parameters due to temperature should be well understood and quantified prior to the establishment of a baseline for use in damage assessment algorithms. Catbas et al. (2008) implemented structural health monitoring and reliability estimation of a long span truss bridge under environmental data. It was seen that the responses due to temperature have a significant effect on the overall system reliability of long span truss bridges. Xu et al. (2010) monitored temperature effect on a long suspension bridge. The statistical relationship between the effective temperature and the displacement of the bridge was developed by the authors. Kim and Laman (2010) determined integral abutment bridge response under thermal loading. The study revealed that the thermal expansion coefficient, bridge length and pile soil stiffness significantly influence the integral abutment bridge response. Li et al. (2010) identified modal behavior of bridges under varying temperature and wind effects. Xia et al. (2011) determined variation of structural vibration characteristics versus non-uniform temperature distribution. Cao et al. (2011) investigated temperature effects on a cable-stayed bridge using health monitoring data. They expressed that temperature gradient in the steel girder was larger than the design specification. Ding et al. (2012) and Ding and Wang (2013) estimated extreme temperature differences and analyzed thermal field characteristic of steel box girders based on long-term measurement data. It was shown that horizontal temperature differences in top plate and vertical temperature differences between top plate and bottom plate are considerable. Li et al. (2014) investigated field monitoring and validation of vortex-induced vibrations of a long-span suspension bridge. It was found that the inhomogeneity of the wind field along the span-wise direction of the bridge is also a critical factor that affects vortex-induced vibrations of full-scale bridge. Faravelli et al. (2014) investigated the temperature effects on the response of the bridge "ÖBB Brücke Großhaslau". de Battista et al. (2015) measured and modelled the thermal performance of the Tamar suspension bridge using a wireless sensor data. Westgate (2012) and Westgate et al. (2015) investigated environmental and solar radiation effects on suspension bridge performance. They demonstrated that peak temperatures of the suspended structure and cables occur at different times. Yarnold and Moon (2015) determined temperature-based structural health monitoring baseline for long-span bridges. Zhou et al. (2013), (2014) and (2015) investigated thermal load effects on the bridges. The transversal and vertical thermal gradients were developed by the authors. Zhou et al. (2016) performed temperature analysis of a long-span suspension bridge based on field monitoring data. Zhang et al. (2017) performed long-term modal analysis of wireless structural monitoring data from a suspension bridge under varying environmental and operational conditions. The study proposed an automated stochastic subspace identification approach for the extraction of bridge modal properties for the large amount of data. Xia et al. (2013) and (2017) investigated in-service condition assessment of a long-span suspension bridge using temperature-induced strain data. A new structural damage identification method using temperature-induced responses was proposed by the authors and applied to a long-span suspension bridge. Li et al. (2017) performed cluster analysis of winds and wind-induced vibrations on a long-span bridge based on long-term field monitoring data. It was shown that the nonuniformity of the wind speed along the span-wise direction has a significant influence on the vortex-induced vibrations mode.

This study aims to investigate in-situ monitored structural behavior of long-span steel cable-stayed bridges under environmental effects. Structural behavior of main structural elements including decks, towers (pylons) and main cables of a long span cable-stayed bridge under environmental effects such as air temperature, humidity and wind are determined by using daily monitoring data. Nissibi cable-stayed bridge constructed in Adıyaman, Turkey, in 2015 is selected as an example. After structural and monitoring systems of the bridge are briefly introduced, the effects of air temperature and wind speed on the behaviors of cables, pylons and deck are investigated by using monitored forces and accelerations.

2. Nissibi Bridge and Its Structural Monitoring System

The long span Nissibi cable-stayed bridge spans the reservoir of Atatürk Dam on the Euphrates River in South Eastern Anatolia (Bayraktar et al. 2017). The bridge was constructed on the 80th km of the Adıyaman-Diyarbakır highway between 2012-2015 in Turkey. A plan, section and view of the bridge are shown in Fig. 1. The bridge total length is 610m. The 400m main span between the two pylons consists of a 380m long, 26.5m wide and 2.70m height orthotropic steel box section and 20m prestresed concrete deck. The each side of prestresed concrete deck is length of 105m. The structural system of the bridge is founded entirely on rock by means of spread footings. The two invert Y pylons have a structural height of 97.78m from top of footing to the top of pylon. The pylon is made of reinforced concrete except for the top region of the 14-cable stay anchors. The side span piers and abutment are designed as reinforced concrete structures supporting the heavy side span prestressed concrete deck. The cable system consists of the typical 7 wire 0.6" galvanized strand and the cable sizes vary depending on the force in the stay cable. Dampers were installed on some of the cables used in the bridge. The deck is carried by 20 double cables (80 cables in total). The deck is supported by lead rubber bearings located on the pylons, side span piers and abutments for

the earthquake protection. In addition to, dilatation joints are used at the beginning and end of the deck. The probability of exceedance of the design earthquake within a period of 50 years was considered as 2% (2475 years) in the seismic analyses. The wind velocity considered in design was 33.6m/s (120km/h).

The monitoring system of the bridge consists of 28 sensors located on the foundations, deck, pylons and cables including load cell, accelerometers, wind, temperature and humidity sensors. Bridge structural monitoring system and some views of the sensors are shown in Figs. 2 and 3.

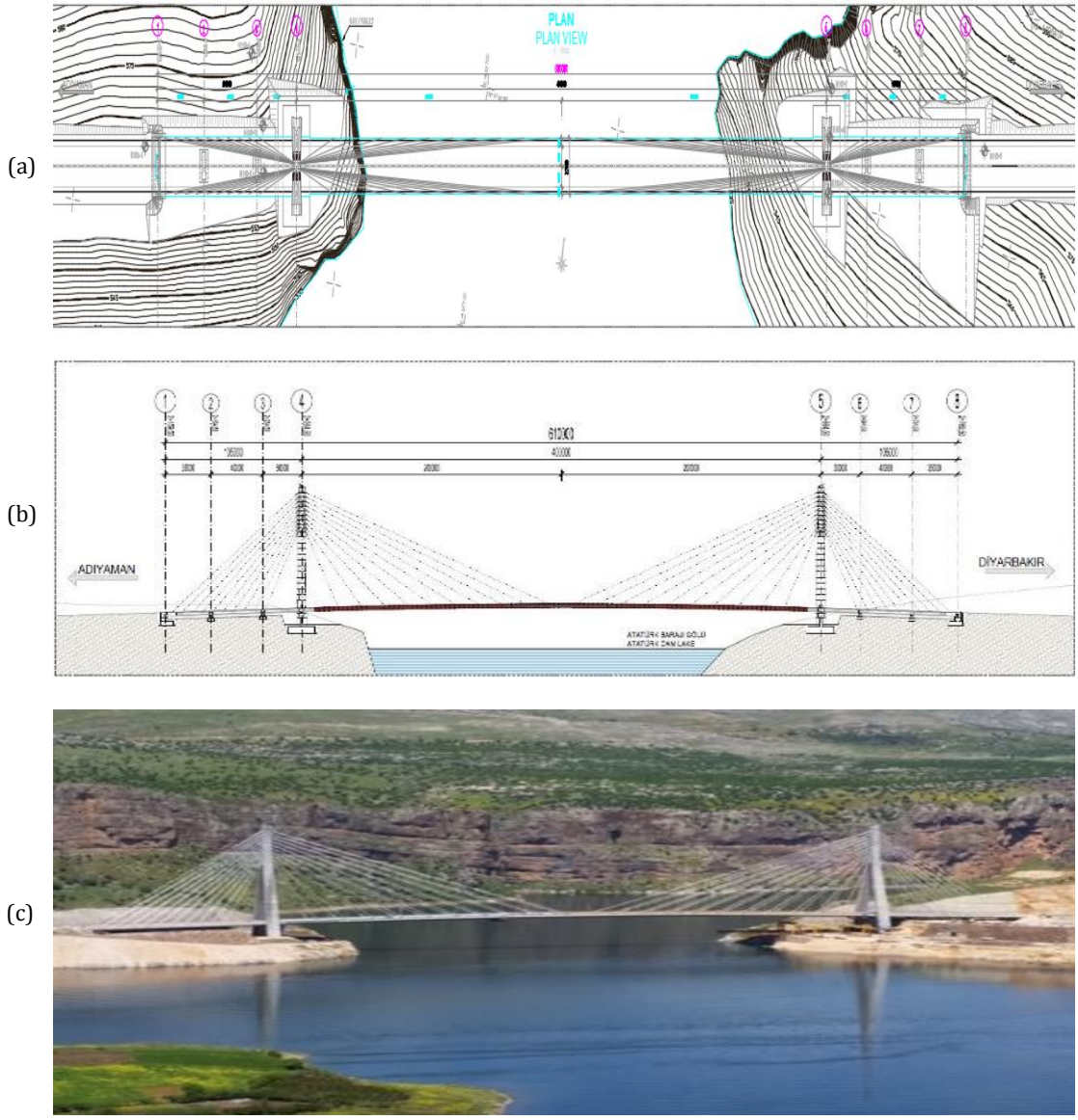

Fig. 1. (a) Plan; (b) longitudinal section; and (c) view from Nissibi Bridge (NBP, 2012; NBR, 2015).

3. Structural Behaviors of Main Structural Elements under Environmental Effects

The cables, pylons and deck behaviors under environmental effects such as air temperature, humidity and wind speed are investigated in this section. The forces and acceleration responses of bridge elements measured from the bridge monitoring system are compared for various environmental meteorology. The data recorded in the hottest summer (July 31, 2015) and the coldest winter (January 1, 2016) days are chosen for the comparisons. The daily variations of air temperature, humidity and wind speed with time are shown in Fig. 4. It can be seen from Fig. 4a that air temperature is above 30°C on July 31 and below 3°C on January 1. The temperature slightly decreases and reaches the minimum in the early morning in both day. The temperature then increases to the maximum in the early afternoon and decreases in the evening and at midnight. The temperature reaches a minimum of approximately 0°C at around 05:00 hrs on January 1 and a maximum of approximately 36°C at around 16:00 hrs on July 31. The relative humidity ratio on January 1 is higher than the ratio on July 31. The humidity decreases and reaches minimum in the evening in both days. Maximum wind speed is observed over 12 m/s on January 1, whereas the maximum wind speeds occur in the afternoon on July 1 and at midnight on January 31. In general, the change in temperature between

July 31 and January 1 is the most significant among all environmental effects measured. The variation of the cables, pylons and deck responses of the bridge due to the above explained environmental effects are discussed below. It is noted that the monitoring data for these elements include the combination of the dead and traffic loads and environmental effects. The traffic-induced component could not be separated from the data.

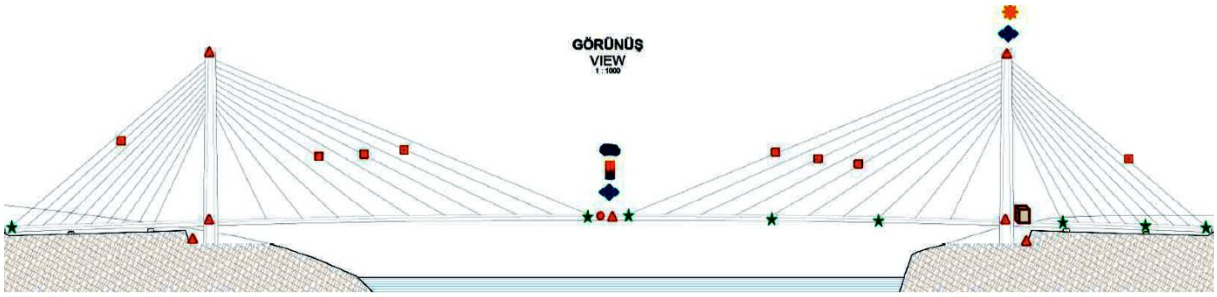

Pos.	Sensorgroup	Abbr.	Nos. of Sensors	Nos. of Channels
1	Ultrasonic wind 3D	UW	2	6
2	Air Temperature/Humidity	AT_H	1	2
3	Solar Radiation	SOL	1	1
4	Accelerometer 3D	A3	7	21
5	Accelerometer 1D	A1	1	1
6	Cable Accelerometer 2D	CA	8	16
7	Transmitter for Cable Load Cell	T-LC	8	8

Fig. 2. The sensor types and locations in Nissibi Bridge (VCE, 2012).

Fig. 3. Some views from sensors located in Nissibi Bridge (NBR, 2015).

3.1. Environmental effects on cable behaviors

The properties of cables on the pylons P4 and P5 are shown in Fig. 5. The prestressed concrete and steel deck are carried by 20 double cables (80 cables in total) in the left and right of pylons P4 and P5. Cables 160, 260, 360 and 451 are selected for the investigation of the response of the cable forces under temperature and wind effects.

It can be seen from Fig. 5 that Cables 160 is with length of 130m, 55 strands and 200mm diameter; and Cable 260 and 360 is with length of 205m and 50 strands and 200mm diameter. Both cables have dampers and are in the right side of the deck. Cable 160 is in the Adıyaman side of pylon P4. Cable 260 at pylon P4 and Cable 360 at pylon P5 are in the middle of the deck span. Cable 451 is with length of 63m, 37 strands and 180mm diameter and is in the Adıyaman side of pylon P5. The environmental effects on cable forces are investigated for an individual strand force in each cable.

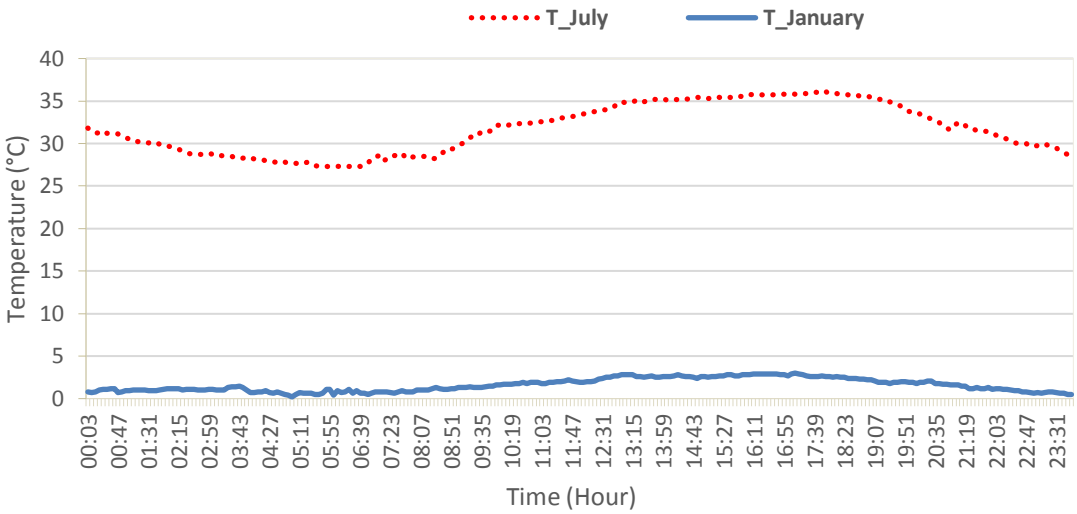

(a) Daily temperature

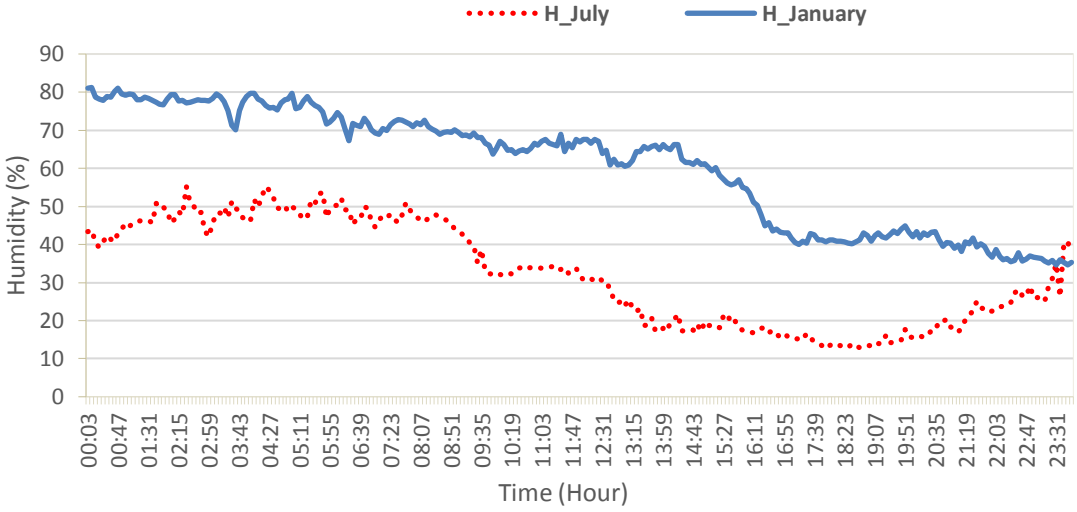

(b) Daily humidity

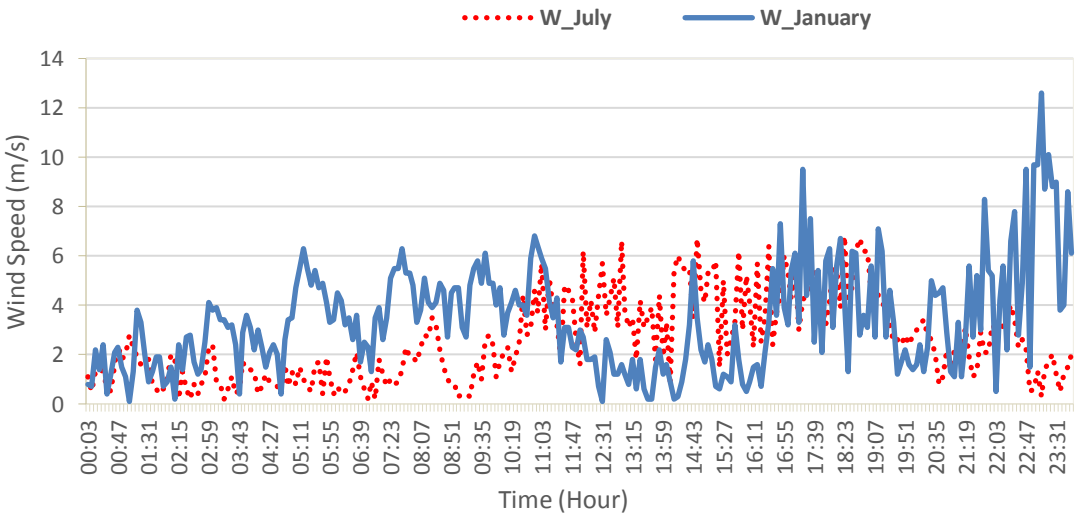

(c) Daily wind speed

Fig. 4. Variations of air temperature, humidity and wind speed on July 31, 2015 and January 1, 2016.

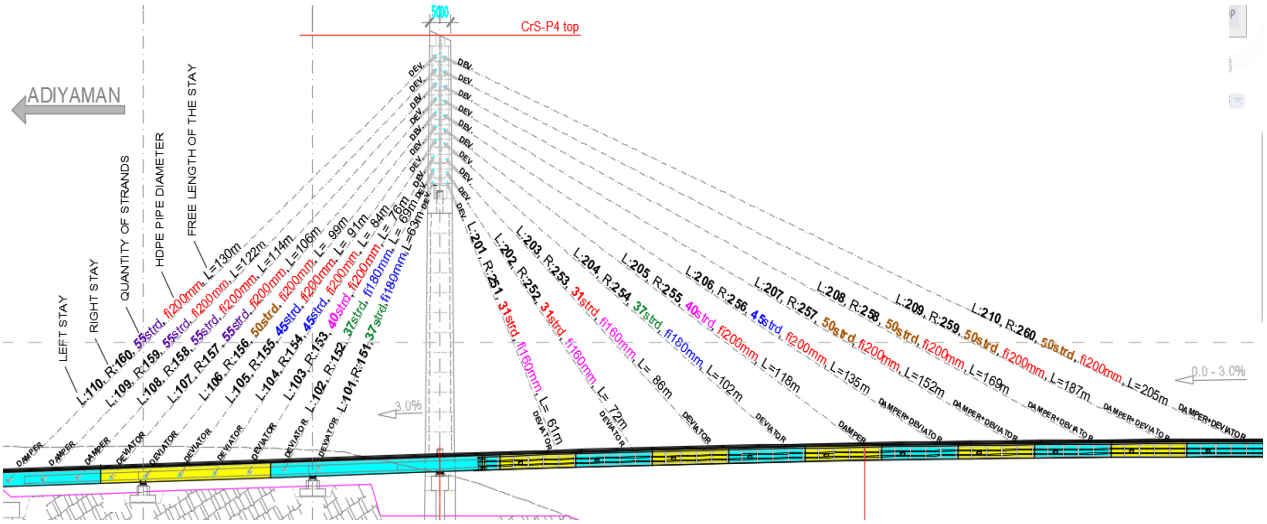

(a) Pylon P4

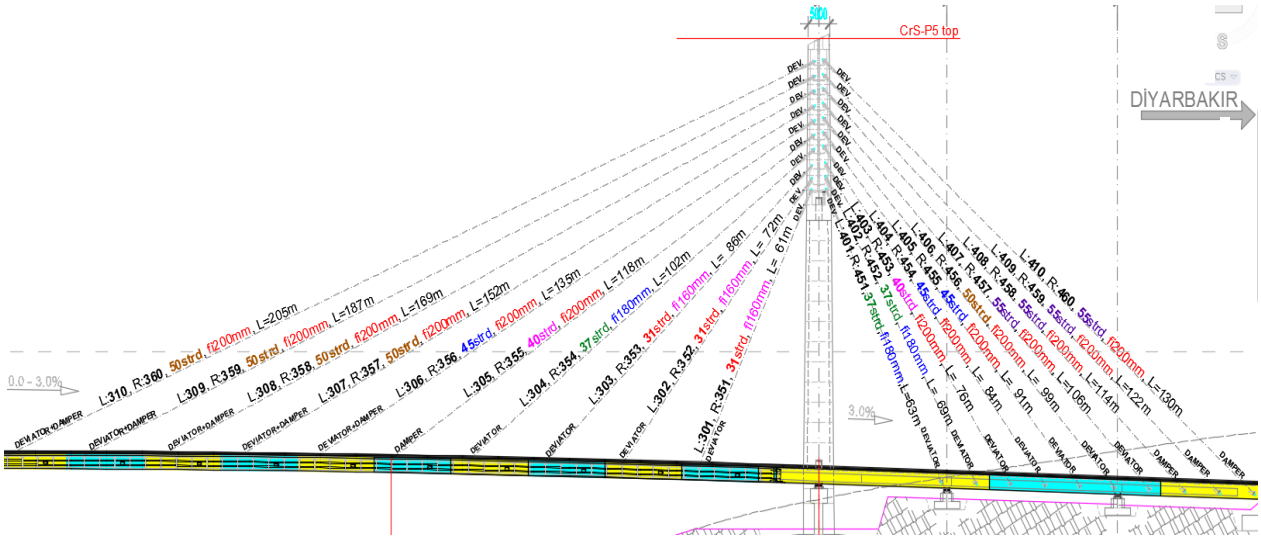

(b) Pylon P5

Fig. 5. Cable properties on the pylons P4 and P5 (NBP, 2012; NBR, 2015).

3.1.1. Temperature effects on cable forces

The variations of temperature and humidity in January 1 and July 31 are shown in Figs. 4a and 4b. The variation of cable forces with air temperature on July 31 and January 1 are depicted for cables 160, 260, 360 and 451 in Figs. 6 and 7. It can be seen from Figs. 6 and 7 that the values of cable forces slightly change in July 31 and January 1 throughout the day. The cable forces increase and reaches the maximum values in the early morning on January 1, in which temperature has smallest values. Besides cable 160, cables forces recorded in July 31 have maximum values in the afternoon, in which temperature has maximum values.

The cable forces in Adıyaman and Diyarbakır sides at pylon P4 and P5, respectively, have different values as shown in Figs. 6 and 7. When compared the forces for cable 260 at pylon P4 and Cable 360 at pylon P5, which has the same length and section properties, the forces recorded for Cable 360 at pylon P5 are larger than those of Cable 260 in January 1 and July 31. However, similar results cannot be obtained for Cable 160 at pylon P4 and Cable 451 at pylon P5.

Comparison of cable forces for Cables 160, 260, 360 and 451 in July and January are shown in Fig. 8. It can be seen from Fig. 8 that while the forces of Cables 160 at pylon P4 and 451 at pylon 5 carrying prestressed concrete deck show approximately constant variation, the forces of Cables 260 and 360 carrying steel deck show more variation through day. Temperature difference between July 31 and January 1 is about 30^0C (Fig. 4a). It can be generally stated that the daily temperature differences in the hottest summer and the coldest winter days changes the cable forces by up to 10%.

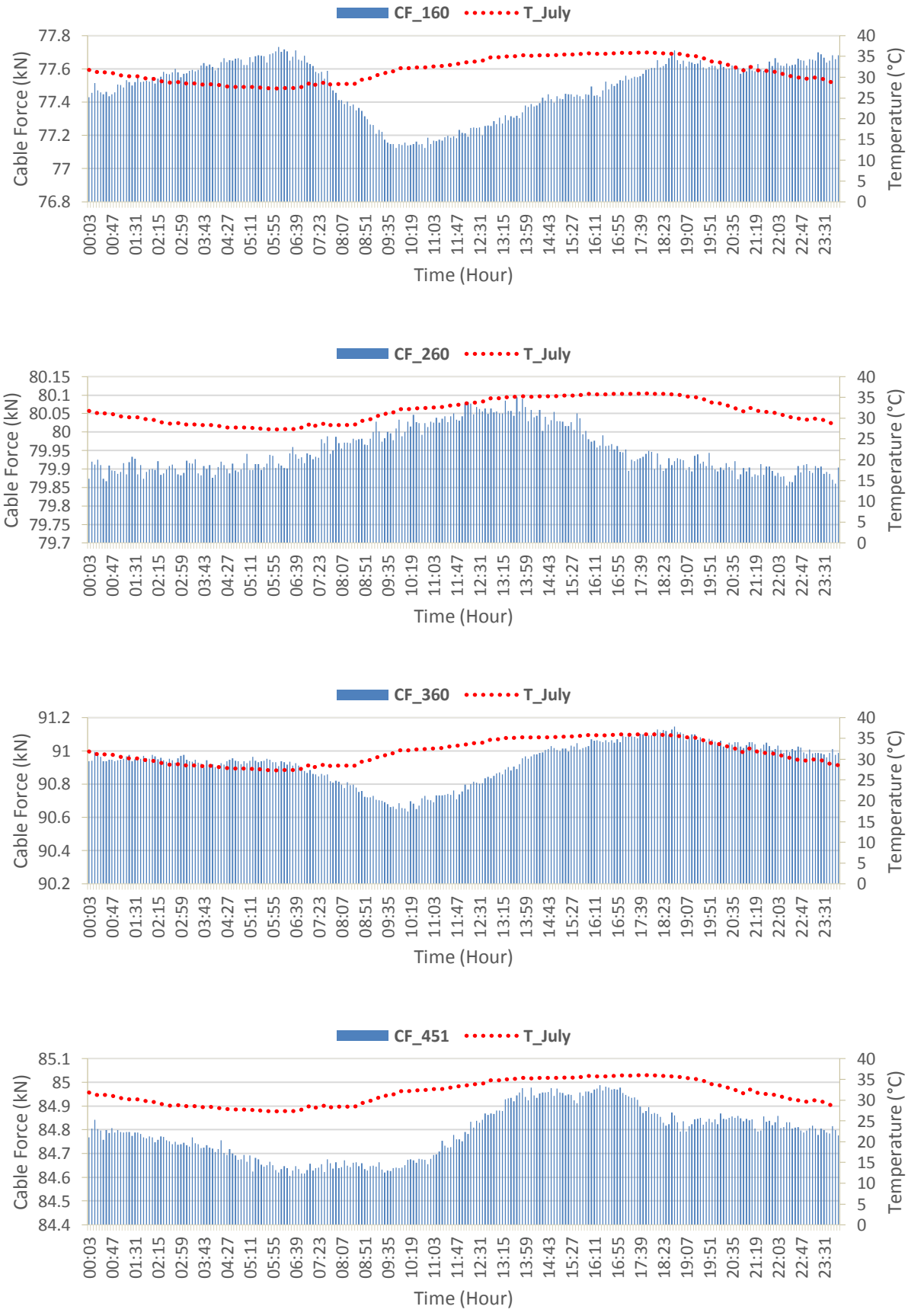

Fig. 6. The variation of cable forces with air temperature on July 31 for cables 160, 260, 360 and 451.

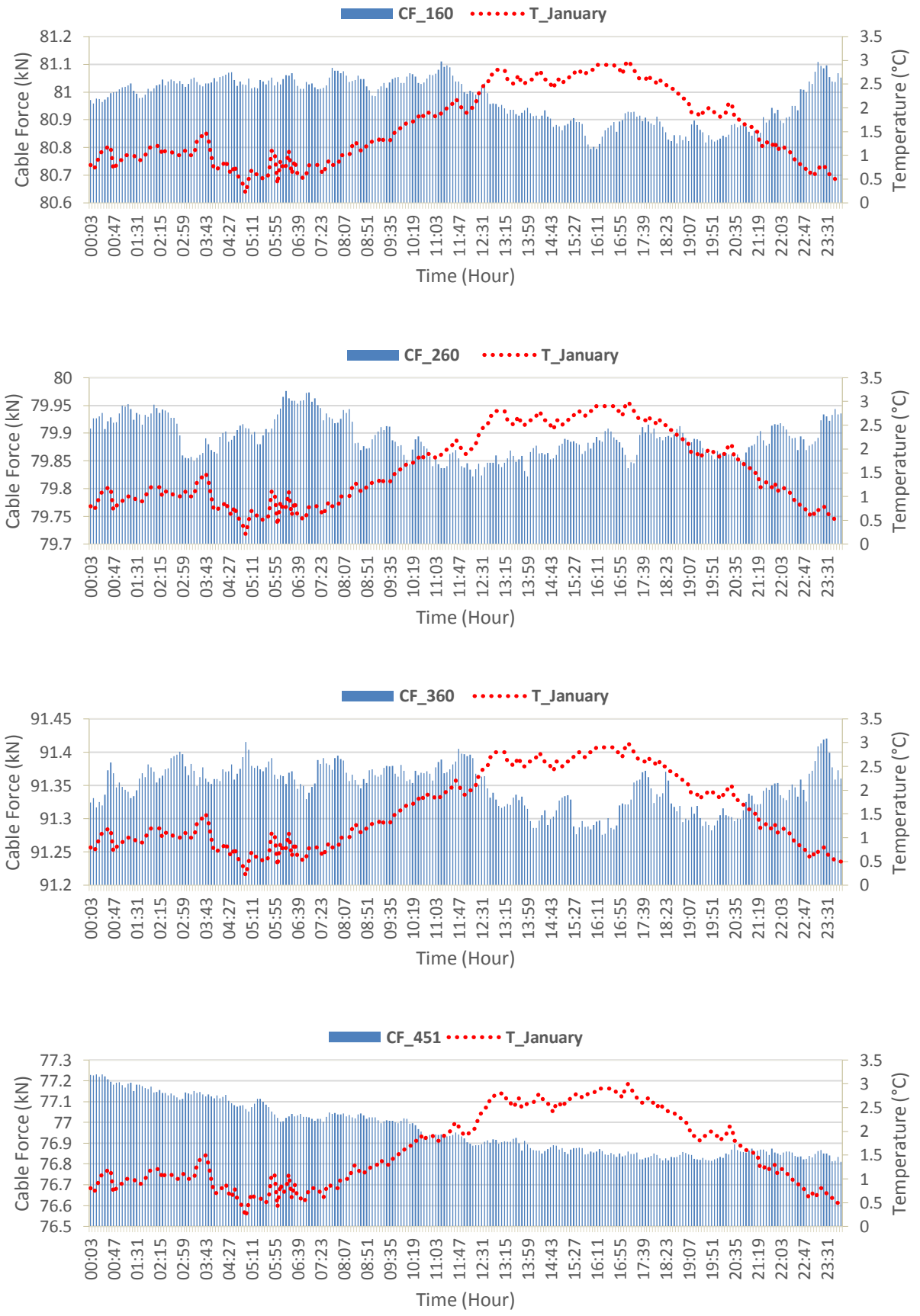

Fig. 7. The variation of cable forces with air temperature on January 1 for cables 160, 260, 360 and 451.

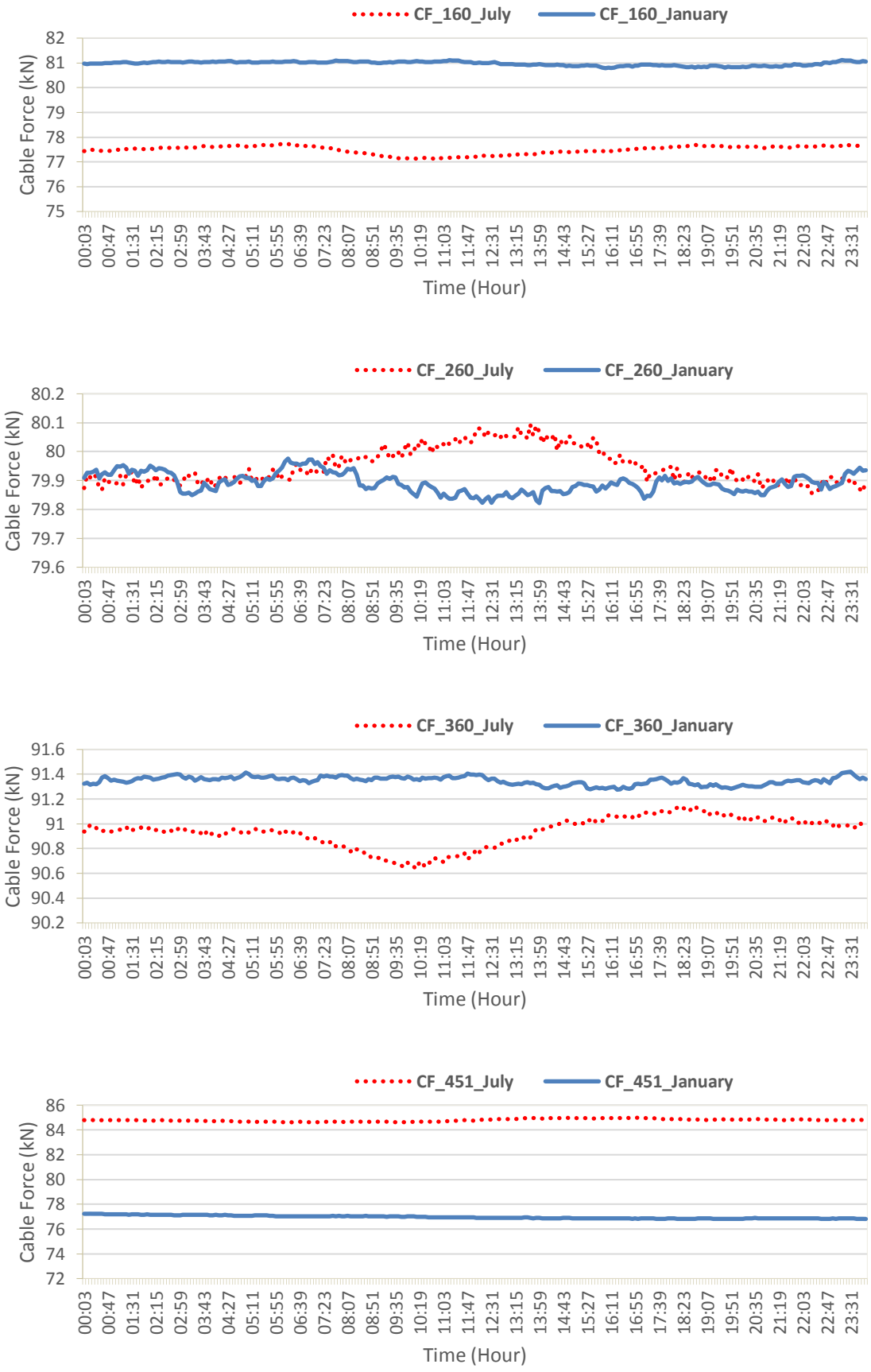

Fig. 8. Comparison of cable forces for 160, 260, 360 and 451 on July 31 and January 1.

3.1.2. Wind speed effects on cable forces

The design wind speed was taken into account as 33.6m/s (120km/h) at the design stage of the bridge. Variations of wind speed on July 31 and January 1 are shown in Fig. 4c. Maximum wind speed recorded was slightly over 12m/s in January 1. The variation of forces for Cable 160, 260, 360 and 451 on July 31 and January 1 are shown in Figs. 9 and 10. It is seen from the figures that wind speeds are more effective on January 1. The cable forces increase with increasing wind speed in the afternoon in July 31 and at the midnight on January 1. It can be generally stated that the daily wind speeds in the hottest summer and the coldest winter days affect the cable forces slightly.

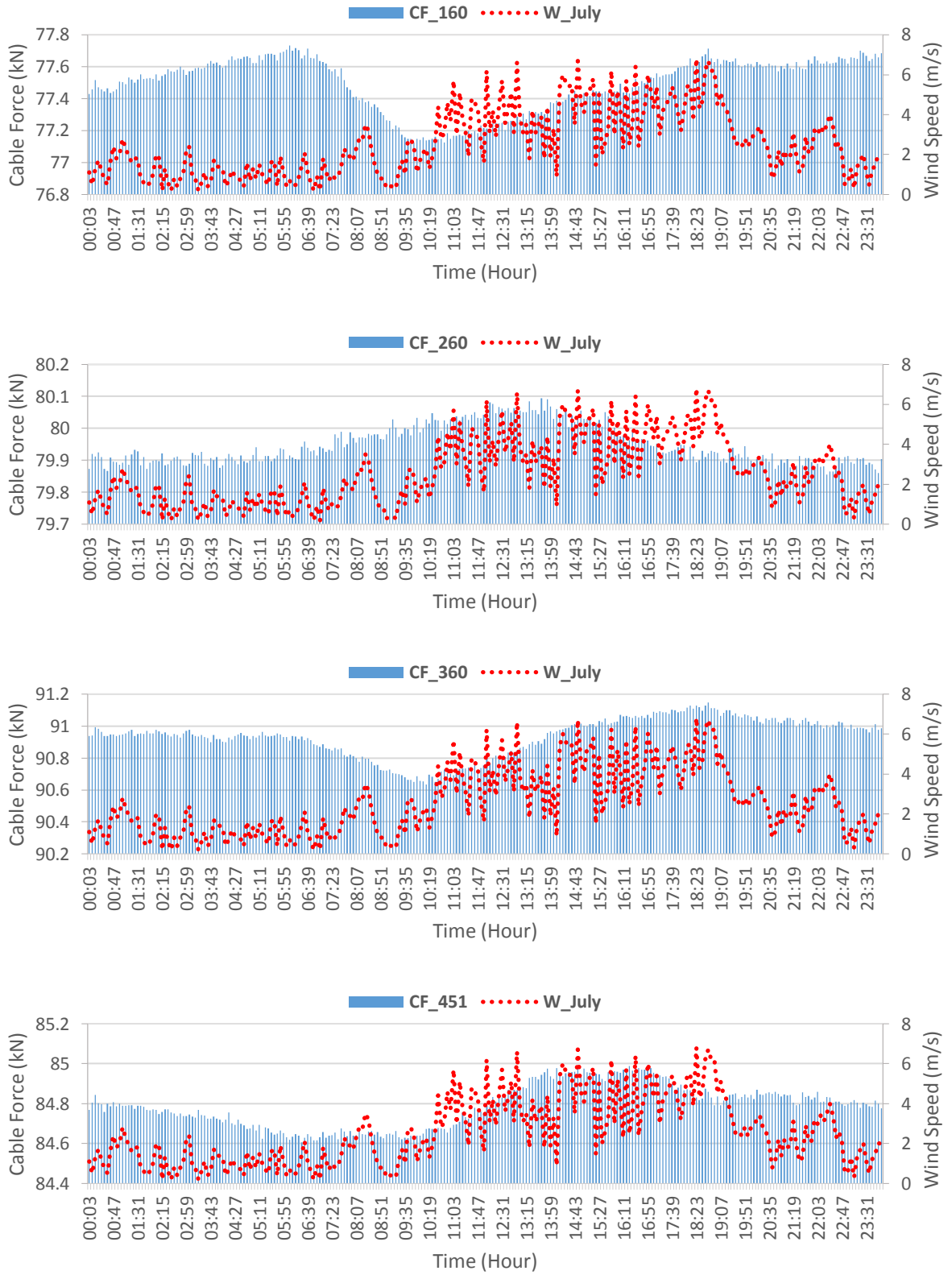

Fig. 9. The variation of cable forces with wind speed on July 31 for cables 160, 260, 360and 451.

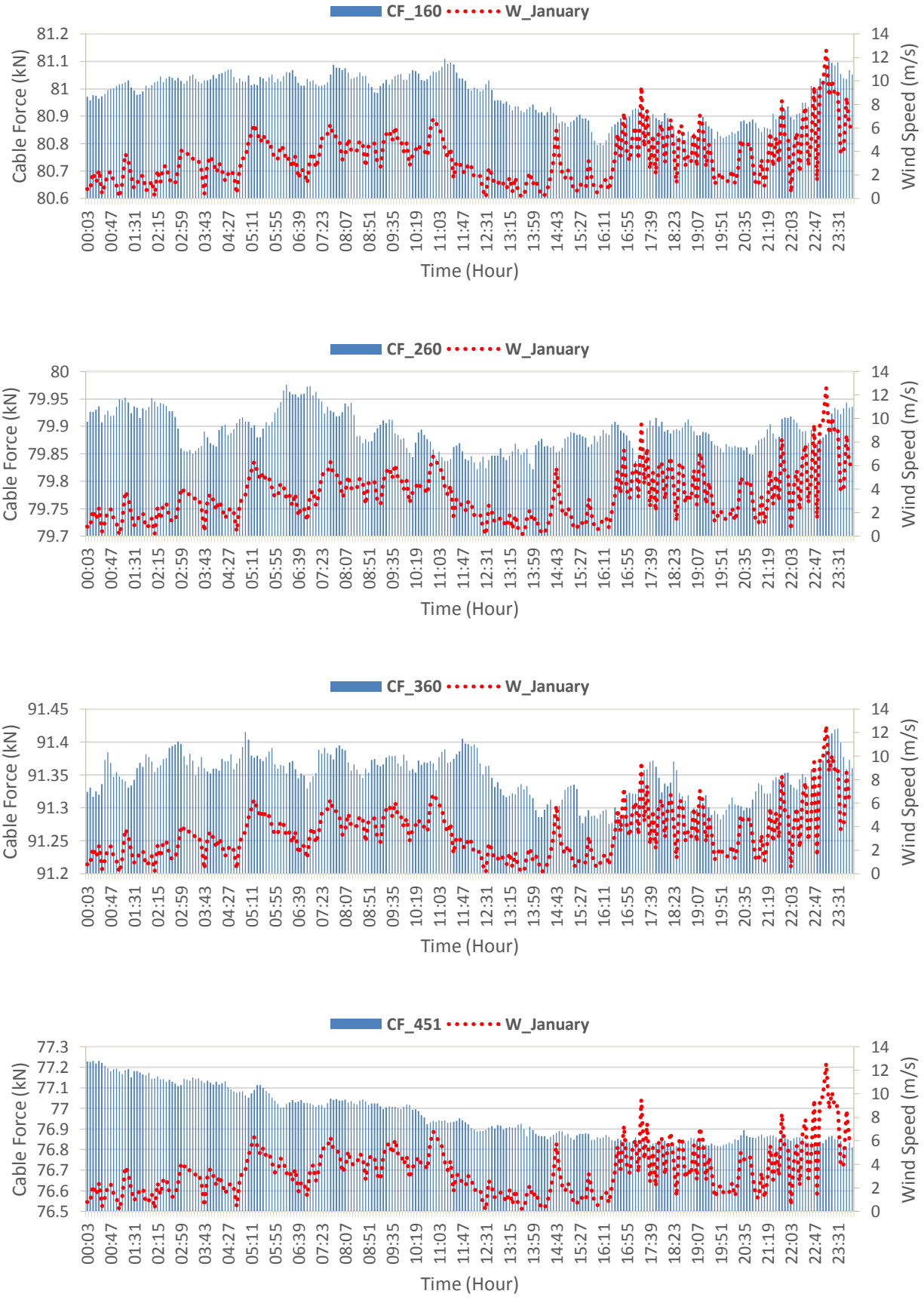

Fig. 10. The variation of cable forces with wind speed on January 1 for 160, 260, 360 and 451.

3.1.3. Environmental effects on cable accelerations

Cables 159 and 259 at pylon 4 are selected to investigate the environmental effects on cable accelerations. The variations of accelerations recorded on Cable 159 and 259 in transverse (1) longitudinal (2) directions of the cables on July 31 and January 1 are given in Fig. 11.

The accelerations in longitudinal (2) direction are smaller than those of the transverse (1) direction. Besides the accelerations in 1 (transverse) direction in Cable 259, all cable accelerations change slightly along the day of January 1. However, accelerations recorded in July 31 show increasing and decreasing changes throughout the day.

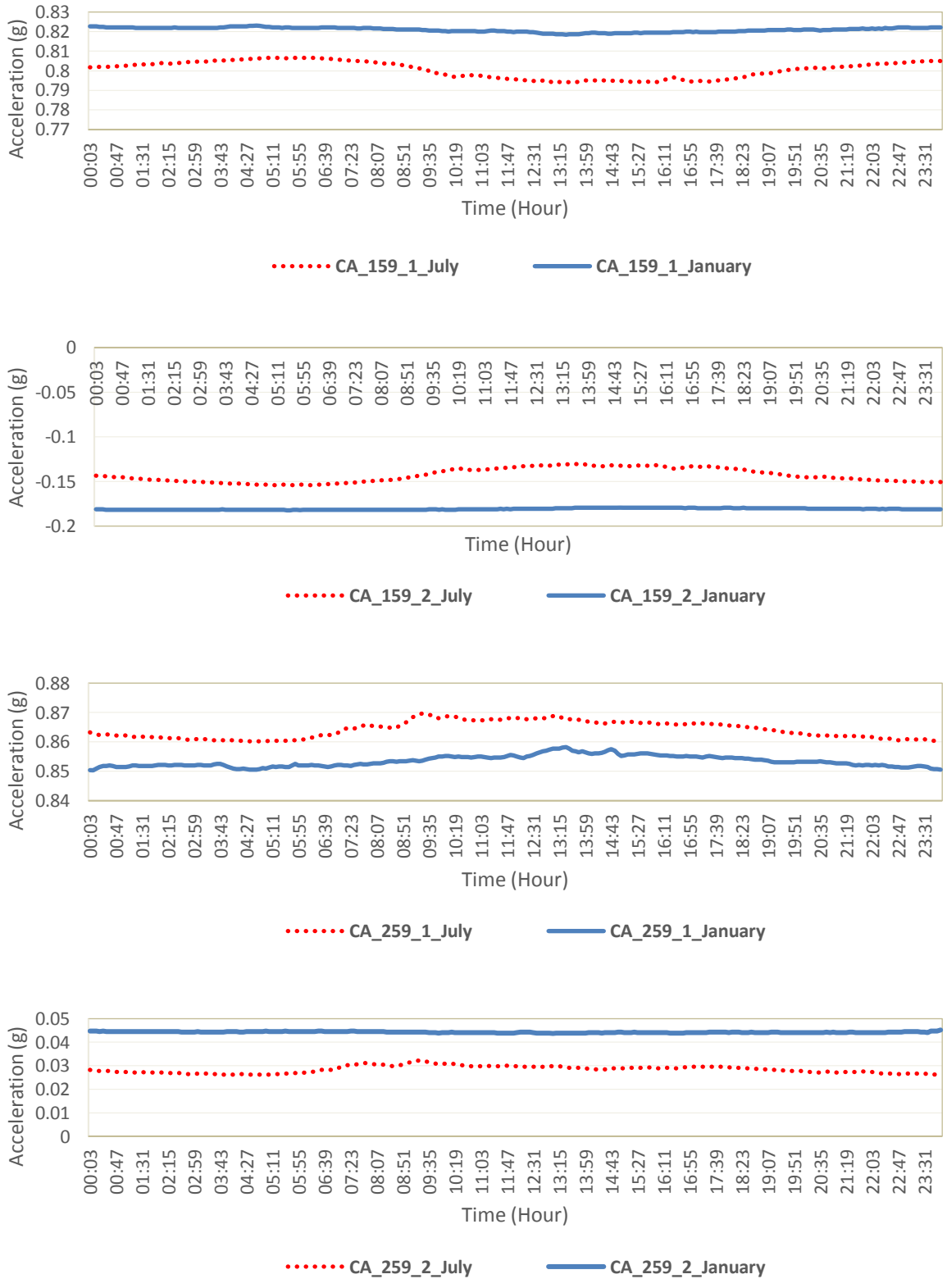

Fig. 11. Comparison of cable accelerations in transverse (1) and longitudinal (2) directions for 159 and 259 on July 31 and January 1.

3.2. Environmental effects on pylon behaviors

Bridge has two pylons named P4 and P5. P4 is in Adıyaman side and P5 is in the Diyarbakır side (Fig. 5). The accelerometers mounted on the top levels of the pylons are shown in Fig. 12. Each accelerometer can take data in three directions such as longitudinal (x), transverse (y) and vertical (z).

The acceleration components recorded on the top of pylons P4 and P5 in July 31 and January 1 are depicted in Figs. 13 and 14. It can be seen from Figs. 13 and 14 that the biggest accelerations occurred in the vertical (z) direction in both July 1 and January 31. The pylon accelerations in Adıyaman and Diyarbakır sides at pylon P4 and P5, respectively, have different values. The acceleration values recorded at the top of pylon P5 are higher than those of the pylon P4. Although accelerations show almost constant variation in January 1, they behave changeable in July 31 in pylon P4 and P5. The values of accelerations in July 31 generally decrease towards noon and increase towards night.

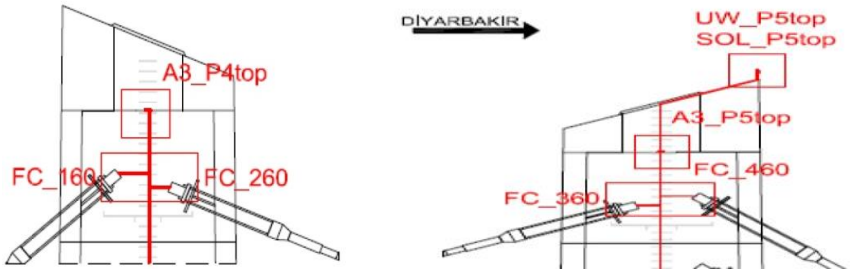

Fig. 12. Accelerometer locations on the P4 and P5 pylons (NBP, 2012; NBR, 2015).

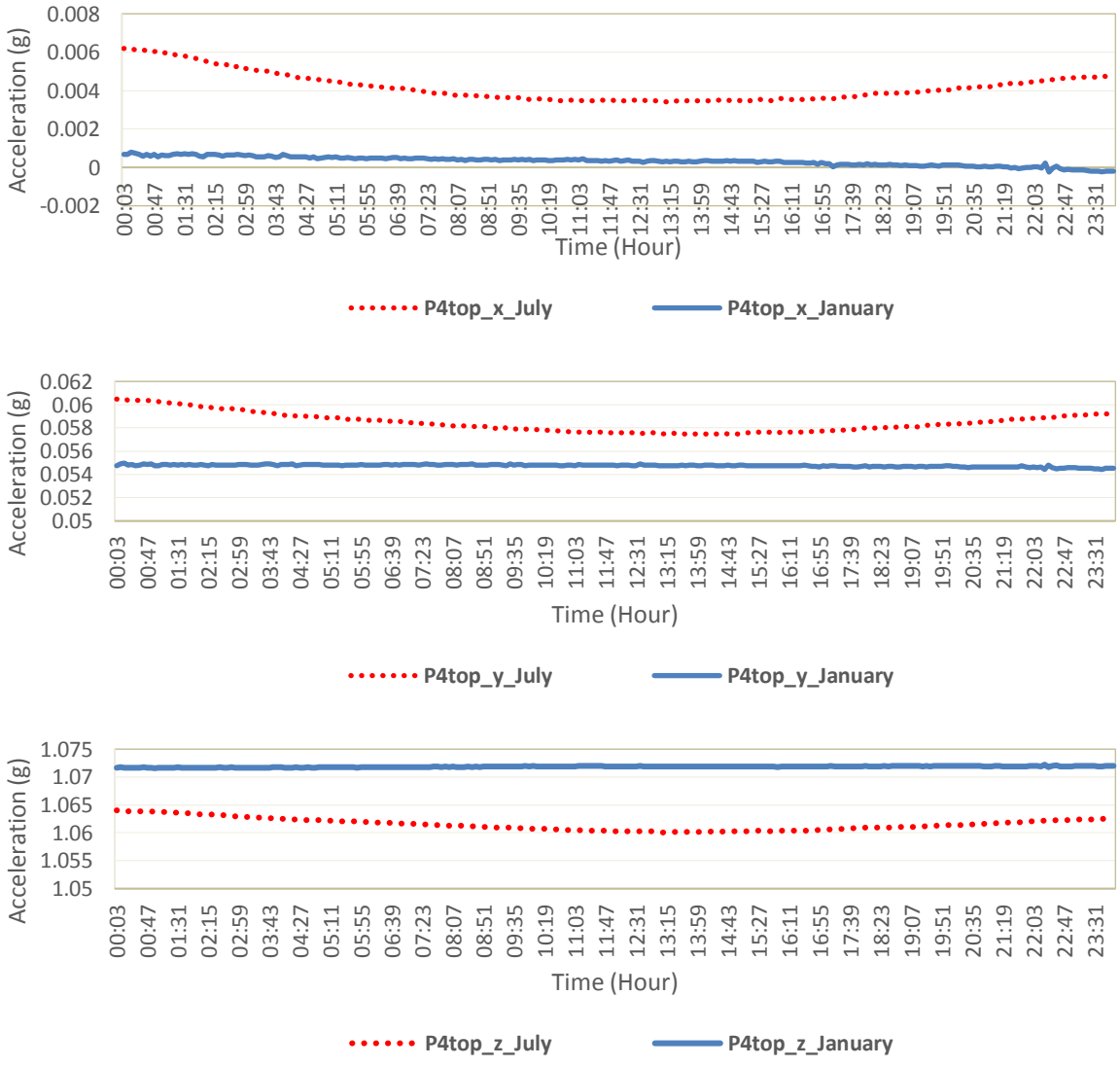

Fig. 13. Comparison of accelerations recorded on the top of pylon P4 in longitudinal (x), transverse (y) and vertical (z) directions on July 31 and January 1.

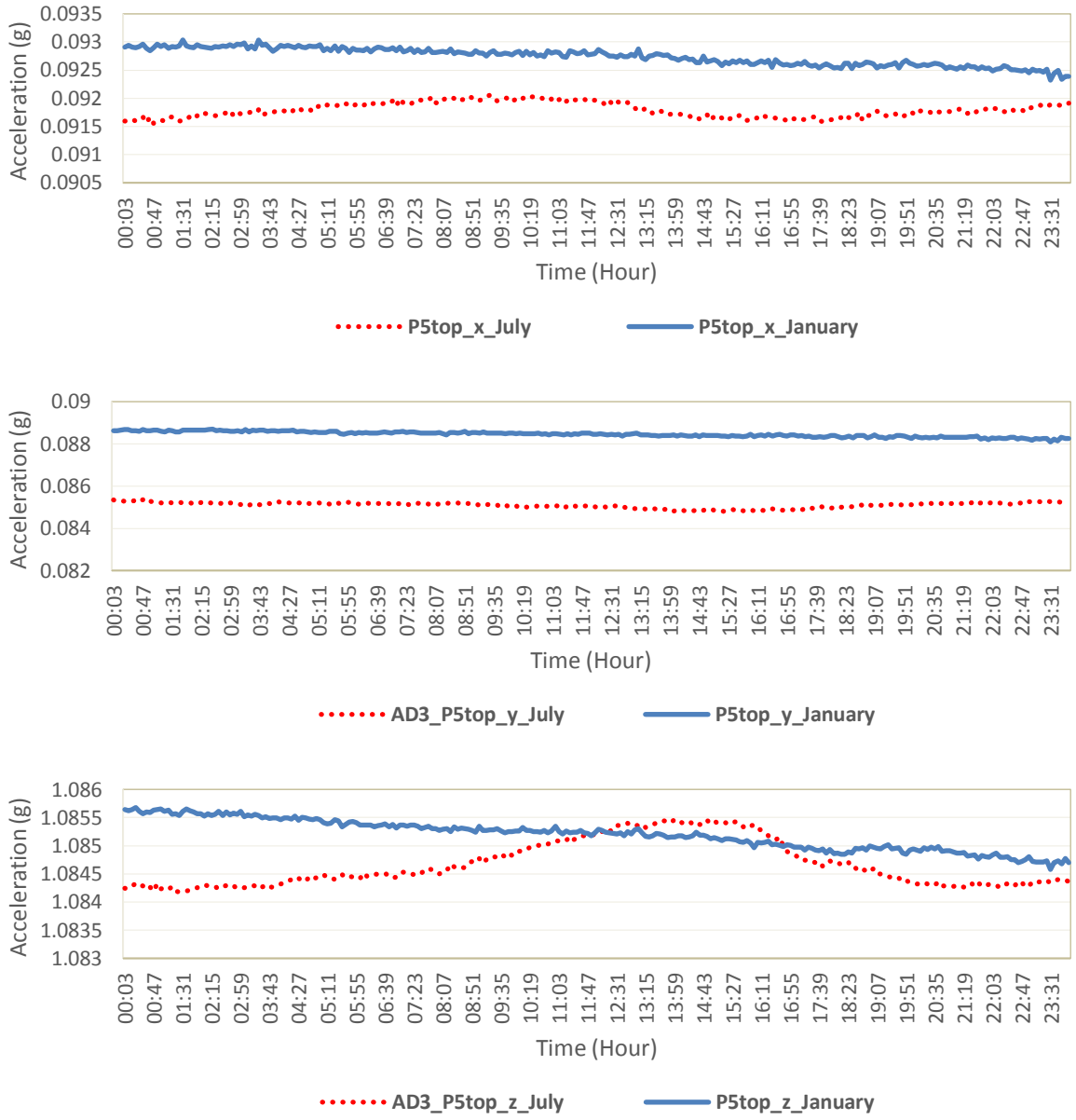

Fig. 13. Comparison of accelerations recorded on the top of pylon P5 in longitudinal (x), transverse (y) and vertical (z) directions on July 31 and January 1.

3.3. Environmental effects on deck behavior

The accelerometer mounted on the deck center is given in Fig. 15. The accelerations recorded on the deck center in longitudinal (x), transverse (y) and vertical (z) directions are plotted in Fig. 16. The largest acceleration occurred in the vertical (z) direction in both July 31 and January 1. While accelerations in January 1 show almost constant variation, the accelerations in July 31 increase towards to noon and decrease to the night.

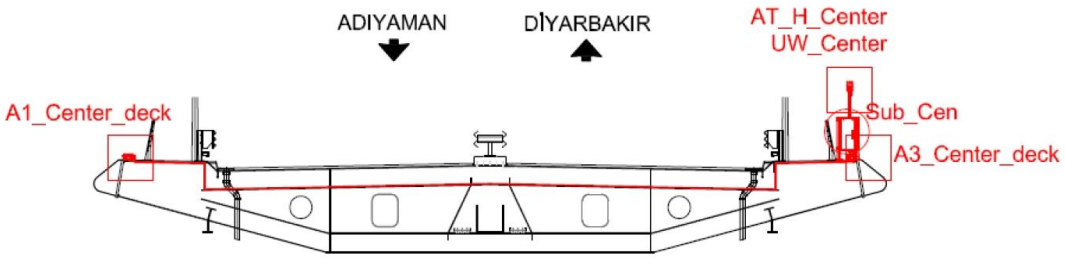

Fig. 14. Accelerometer locations at the deck center (NBP, 2012; NBR, 2015).

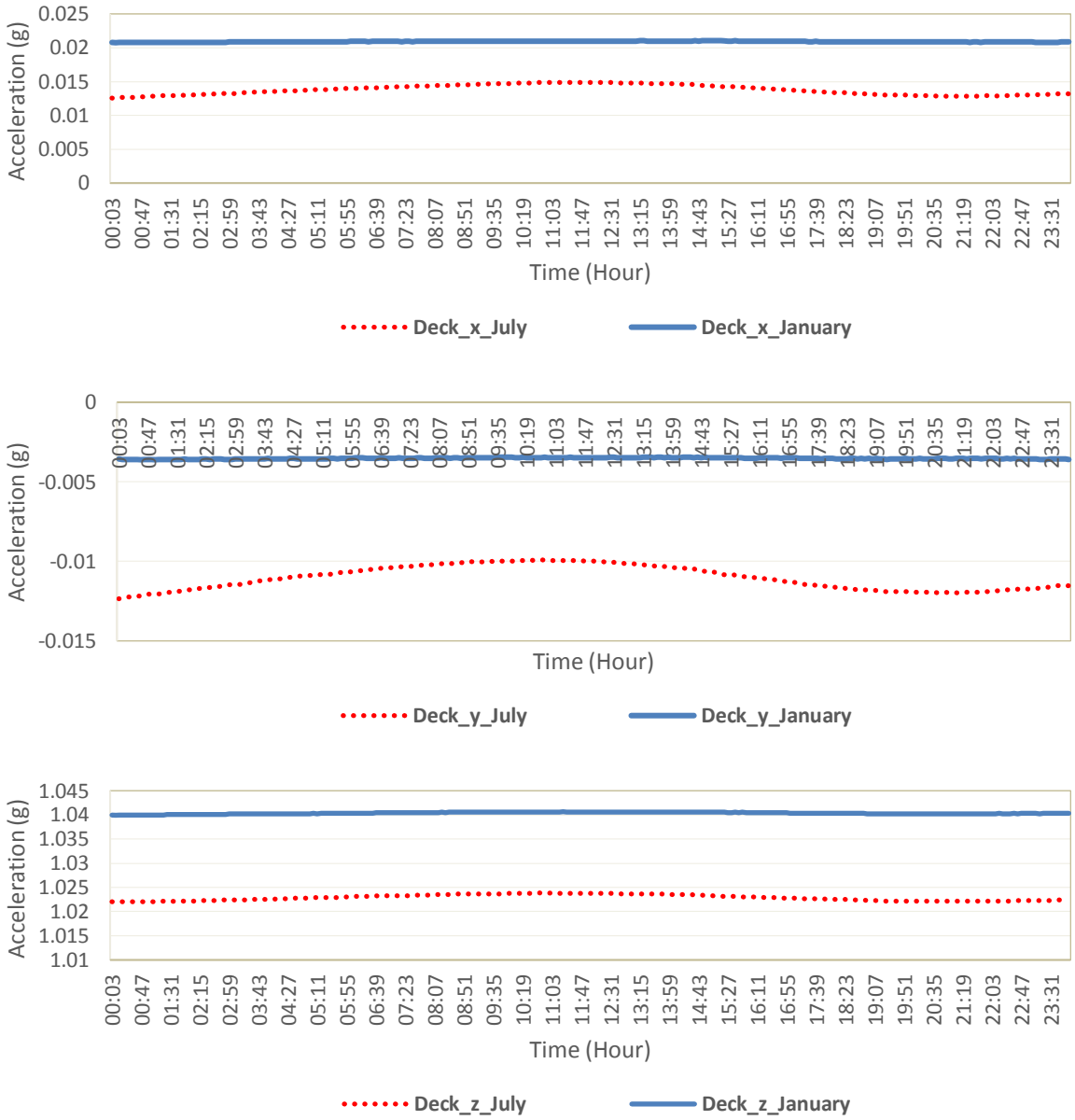

Fig. 16. Comparison of accelerations recorded on the deck center in longitudinal (x), transverse (y) and vertical (z) directions on July 31 and January 1.

4. Conclusions

The monitored structural behavior of cables, pylons and deck of a long span cable-stayed bridge are investigated under environmental effects such as air temperature and wind speed. The daily variations of cable forces and accelerations, and pylon and deck accelerations are obtained for the hottest summer (July 31, 2015) and the coldest winter (January 1, 2016) days. The results obtained from the study are summarized below as:

- The values of cable forces changes depending the daily air temperature. The cable forces increased and reached the maximum values in the early morning of January 1, in which temperature has the lowest values. Cables forces recorded on July 31 generally have maximum values in the afternoon, in which temperature has also the maximum values.
- The wind speed has more effect on the cable forces on January 1. The forces of the long cables increase with increasing wind speed in the afternoon for both July 31 and January 1.
- The cable accelerations in longitudinal direction are smaller than those of the transverse direction. While the cable accelerations recorded on July 31 show an increasing and decreasing changes, they change slightly in January 1 throughout the day.
- The pylon accelerations in Adıyaman and Diyarbakır sides at pylon P4 and P5, respectively, have different values. The values of the acceleration recorded in pylon P5 are higher than those of pylon P4. Although accelerations show almost constant variation in January 1, they exhibited more variation in July 31. The values of accelerations in July 31 generally decrease towards noon and increase towards night.

- While accelerations recorded in the deck center in January 1 show almost little variation, the accelerations in July 31 increase towards noon and decrease towards the night.
- The maximum accelerations in the deck and pylons occur in vertical directions. The cable accelerations in longitudinal direction are smaller than those of the transverse direction.

It is generally stated from the results that the structural behaviors of cable-stayed bridges are sensitive to the changing environmental load distributions due to their highly statically indeterminacy. Therefore, special attention must be given during the data taken from the bridge monitoring system and evaluated by experienced engineers.

Acknowledgements

The authors would like to express sincere thanks to General Directorate of Highways, the 9th Regional Directorate of Highways, GÜLSAN Inc. and EMAY Inc. for their contributions.

References

Bayraktar A, Türker T, Tadla J, Kurşun A, Erdiş A (2017). Static and dynamic field load testing of the long span Nissibi cable-stayed bridge. *Soil Dynamics and Earthquake Engineering,* 94, 136-157.

Cao Y, Yim J, Zhao Y, Wang ML (2011). Temperature effects on cable stayed bridge using health monitoring system: a case study. *Structural Health Monitoring,* 10(5), 523-537.

Catbas FN, Susoy M, Frangopol DM (2008). Structural health monitoring and reliability estimation: Long span truss bridge application with environmental monitoring data. *Engineering Structures*, 30(9), 2347-2359.

de Battista N, Brownjohn JMW, Tan HP, Koo KY (2015). Measuring and modelling the thermal performance of the Tamar suspension bridge using a wireless sensor network. *Structure and Infrastructure Engineering,* 11(2), 176-193.

Ding Y, Wang G (2013). Estimating extreme temperature differences in steel box girder using long-term measurement data. *Journal of Central South University*, 20(9), 2537-2545.

Ding Y, Zhou G, Li A, Wang G (2012). Thermal field characteristic analysis of steel box girder based on long-term measurement data. *International Journal of Steel Structures*, 12(2), 219-232.

Faravelli L, Bortoluzzi D, Messervey TB, Sasek L (2014). Temperature effects on the response of the bridge "ÖBB Brücke Großhaslau. *Mechanics and Model-Based Continuum of Advanced Engineering System*, 85-94.

Fujino Y, Yoshida Y (2002). Wind-induced vibration and control of Trans-Tokyo Bay Crossing Bridge. *Journal of Structural Engineering*, 128(8), 1012-1025.

Kim W, Laman JA (2010). Integral abutment bridge response under thermal loading. *Engineering Structures*, 32(6), 1495-1508.

Li H, Laima SJ, Zhang QQ, Li N, Liu ZQ (2014). Field monitoring and validation of vortex-induced vibrations of a long-span suspension bridge. *Journal of Wind Engineering and Industrial Aerodynamics*, 124, 54-67.

Li H, Li S, Ou J, Li H (2010). Modal identification of bridges under varying environmental conditions: Temperature and wind effects. *Structural Control and Health Monitoring*, 17(5), 495-512.

Li S, Laima S, Li H (2017). Cluster analysis of winds and wind-induced vibrations on a long-span bridge based on long-term field monitoring data. *Engineering Structures*, 138, 245-259.

Liu C, DeWolf J (2007). Effect of temperature on modal variability of a curved concrete bridge under ambient loads. *Journal of Structural Engineering*, 133(12), 1742-1751.

Lucas JM, Berred A, Louis C (2003). Thermal actions on a steel box girder bridge. *Proceedings of the Institution of Civil Engineers: Structures and Buildings*, 156(2), 175-182.

Mondal P, DeWolf JT (2007). Development of computer-based system for the temperature monitoring of a post-tensioned segmental concrete box-girder bridge. *Computer-Aided Civil and Infrastructure Engineering,* 22(1), 65-77.

NBP (2012). Nissibi Bridge Project. Gülsan, Yüksel Proje and Wiecon Company, İstanbul, Turkey.

NBR (2015). Nissibi Bridge Reports. Gülsan Company, İstanbul, Turkey.

Peeters B, De Roeck G (2001). One-year monitoring of the Z24 Bridge: Environmental effects versus damage events. *Earthquake Engineering and Structural Dynamics*, 30(2), 149-171.

Sohn H, Dzwonczyk M, Straser, EG, Kiremidjian AS, Law KH, Meng T (1999). An experimental study of temperature effect on modal parameters of the Alamosa Canyon Bridge. *Earthquake Engineering and Structural Dynamics*, 28(8), 879-897.

Tong M, Tham LG, Au FT (2002). Extreme thermal loading on steel bridges in tropical region. *Journal of Bridge Engineering*, 7(6), 357-366.

Tong M, Tham LG, Au FTK, Lee PKK (2001). Numerical modelling for temperature distribution in steel bridges. *Compututers and Structures*, 79(6), 583-593.

VCE (2012). Bridge Monitoring System. Vienna.

Westgate RJ (2012). Environmental effects on a suspension bridge's performance. *Ph.D. thesis*, University of Sheffield, Sheffield, U.K.

Westgate R, Koo K, Brownjohn J (2015). Effect of solar radiation on suspension bridge performance. *Journal of Bridge Engineering*, 20(5), Article ID 04014077.

Xia Q, Cheng YY, Zhang J, Zhu FQ (2017). In-service condition assessment of a long-span suspension bridge using temperature-induced strain data. *Journal of Bridge Engineering*, 22(3), Article ID 04016124.

Xia Y, Chen B, Zhou XQ, Xu YL (2013). Field monitoring and numerical analysis of Tsing Ma Suspension Bridge temperature behavior. *Structural Control and Health Monitoring*, 20(4), 560-575.

Xia Y, Xu YL, Wei ZL, Zhu HP, Zhou XQ (2011). Variation of structural vibration characteristics versus non-uniform temperature distribution. *Engineering Structures*, 33(1), 146-153.

Xu YL, Chen B, Ng CL, Wong KY, Chan WY (2010). Monitoring temperature effect on a long suspension bridge. *Structural Control and Health Monitoring*, 17(6), 632-653.

Yarnold MT, Moon FL (2015). Temperature-based structural health monitoring baseline for long-span bridges. *Engineering Structures*, 86(1), 157-167.

Yarnold MT, Moon FL, Aktan E (2015). Temperature-based structural identification of long-span bridges. *Journal of Structural Engineering*, 141(11), Article ID 04015027.

Zhang Y, Kurata M, Lynch JP (2017). Long-term modal analysis of wireless structural monitoring data from a suspension bridge under varying environmental and operational conditions: System design and automated modal analysis. *Journal of Engineering Mechanics*, 143(4), Article ID 04016124.

Zhou GD, Yi TH (2013). Thermal load in large-scale bridges: a state-of-the-art review. *International Journal of Distributed Sensor Networks*, Article ID 217983.

Zhou GD, Yi TH (2014). A summary review of correlations between temperatures and vibration properties of long-span bridges. *Mathematical Problems in Engineering*, Article ID 638209.

Zhou GD, Yi TH, Chen B, Zhang H (2015). Analysis of three-dimensional thermal gradients for arch bridge girders using long-term monitoring data. *Smart Structures and Systems*, 15(2), 469-488.

Zhou L, Yong Xia Y, Brownjohn JMW, Koo KY (2016). Temperature analysis of a long-span suspension bridge based on field monitoring and numerical simulation. *Journal of Bridge Engineering*, 21(1), Article ID 04015027.

Challenge Journal of Structural Mechanics

Research Article

Necessary height of the vertical stiffeners in steel silos on discrete supports

Lyubomir A. Zdravkov *

Department of Metal, Wood and Plastic Structures, University of Architecture, Civil Engineering and Geodesy (UACEG), Sofia 1046, Bulgaria

ABSTRACT

The steel silos are interesting complex facilities. In order to ensure unloading of whole amount of stored product by gravity, the steel silos are often placed on supporting frame structure. Values of stresses in the joints between the thin walled shell and supporting frame elements are very high. It can causes local loss of stability in the shell. To prevent its local buckling, many designers put stiffening elements above the supports. Here the question is how high should be the stiffening elements? The right solution is that they should reach that level till which the values of the meridional normal stresses above the supports and in the middle between them are equalized. Under this level the cylindrical shell will be considered as a ring beam, stiffened by elements above the supports. Above it, the cylinder can be calculated as continuously supported shell. But where is this level? A lot of researchers worked on values and way of distribution of normal meridional stresses above the supports of the cylindrical shells. As a result of their efforts are determined critical height H_{cr} of the shell and the ideal position H_l of intermediate stiffening ring. But these heights are considerably different between each other. To which of them our vertical stiffening elements should achieve?

ARTICLE INFO

Article history:
Received 20 May 2018
Revised 12 October 2018
Accepted 30 October 2018

Keywords:
Steel silos
Meridional stress
Critical high
Vertical stiffener
Loss of stability

1. Introduction

Often steel silos are lifted facilities, placed on supporting structure. The purpose is to unload all stored product easily and completely by gravity. Supporting structure for every project is different, depending on real conditions of exploitation. The most popular are two types – built by horizontal girders and columns or by columns only. Both types frame structure cause concentration of meridional forces in the cylindrical body of the silos. As a result, the thin walled shell could loses local stability.

The simplest way to design steel silos is hypothetically to divide cylindrical shell on two parts - discretely supported ring beam and continuously supported shell above it. This conception is accepted by the European standard EN 1993-4-1, see Fig. 1. Obviously, to ensure continuous support of shell, bending stiffness of ring beam should be high. Unfortunately in EN 1993-4-1 is not mentioned the recommended stiffness of ring beam.

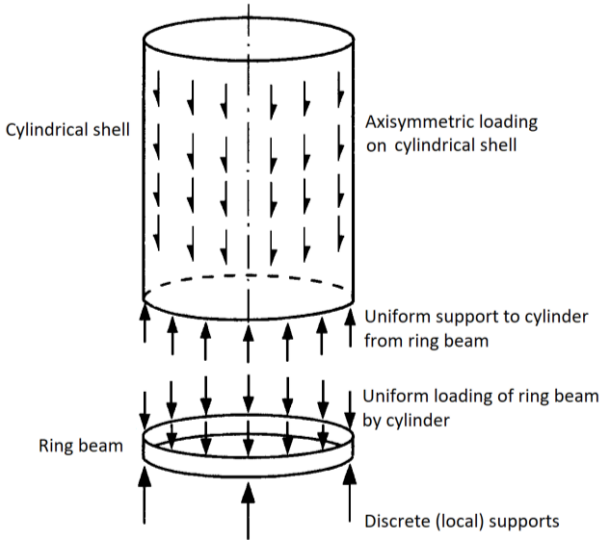

Fig. 1. Traditional design model for silos on discrete supports.

* *Corresponding author*. Tel.: +359-885-081-305 ; E-mail address: zdravkov_fce@uacg.bg (L. A. Zdravkov)
ISSN: 2149-8024 / DOI: https://doi.org/10.20528/cjsmec.2018.04.003

Rotter (1985) suggested that a value of ratio ψ = 0.25 might be suitable for adoption in design, where:

$$\psi = \frac{K_{shell}}{K_{ring}}, \quad (1)$$

in which: K_{shell} is stiffness of cylindrical shell; K_{ring} - stiffness of ring beam.

Based on English translation of study of Vlasov (1961) about of curved beams, stiffness of ring beam K_{ring} is expressed as:

$$K_{ring} = \frac{(n^2-1)^2 EI_r}{R^4}\frac{1}{f_r}, \quad (2)$$

where: n is number of uniformly spaced supports; E - modulus of elasticity; I_{r} - moment of inertia about a radial axis; R - radius of ring beam centroid.

$$f_r = 1 + \frac{EI_r}{n^2 K_T}, \quad (3)$$

in which:

$$K_T = GJ + n^2\frac{EC_w}{R^2}, \quad (4)$$

where: G is shear modulus; J - torsional constant; C_{w} - warping constant for an open sections.

Semimebrane theory of shells, proposed by Vlasov (1964), gives an expression of stiffness of cylindrical shell, as follow:

$$K_{shell} = n\sqrt{(n^2-1)}\frac{E}{\sqrt[4]{3}}\left(\frac{t}{R}\right)^{3/2}\frac{1}{f_s}, \quad (5)$$

where: t is a thickness of the cylindrical shell.

$$f_s = \frac{(e^\eta)^2 - 2e^\eta sin(\eta) - 1}{(e^\eta)^2 - 2e^\eta cos(\eta) + 1}, \quad (6)$$

in which:

$$\eta = \frac{2\pi H}{\mu}, \quad (7)$$

where: H is height of cylindrical shell; μ – expressed by Calladine (1983) long wave bending half-wavelength:

$$\mu = \frac{2\pi\sqrt[4]{3}}{n\sqrt{(n^2-1)}}\sqrt{\frac{R}{t}}R\,. \quad (8)$$

Based on Eqs. (2) and (5), stiffness ratio ψ will look like as:

$$\psi = \frac{K_{shell}}{K_{ring}} = \frac{0.76(Rt)^2}{I_r}\sqrt{\frac{R}{t}}\sqrt{\frac{n^2}{(n^2-1)^3}}\frac{f_r}{f_s}, \quad (9)$$

For simplification, the Eq. (6) could be represented by two simple relations:

$$f_s = \begin{cases} \frac{\eta}{3}, when\ H \le H_{cr} \\ 1.0, when\ H > H_{cr} \end{cases}, \quad (10)$$

where: H_{cr} is critical height of cylindrical shell. It could be determined by formula:

$$H_{cr} = \frac{3\sqrt[4]{3}}{n\sqrt{(n^2-1)}}\sqrt{\frac{R}{t}}R\,. \quad (11)$$

H_{cr} represents the height of shell which is effective of redistributing of discrete forces from supports and equalizing of axial normal stresses. When height of shell $H \le H_{\text{cr}}$, entire shell resists axial loads from supports. When $H > H_{\text{cr,}}$ only that part between bottom of shell and critical height H_{cr} is effective in redistributing of vertical reactions from discrete columns.

In their researches Topkaya and Rotter (2011a, 2011b) conducted extensive finite element analyses for verification of Rotter's criterion about stiffness of ring beam. With 1280 separate finite-element analyses (FEA), covering two different types of ring sections, various heights and radii of cylindrical shells, the authors checked validity of suggested by Rotter (1985) ratio ψ = 0.25. On basis of done FEA they concluded, when a stiffness ratio $\psi \le 0.1$, axial stresses will not deviate more than 25% from the uniform support assumption.

Later Topkaya and Rotter (2014) determined ideal location of intermediate stiffening rings on the shell. They expect a ring, placed at this ideal position, can effectively remove all circumferential nonuniformity in the axial membrane stress above it. The simple expression of ideal location H_{I} is:

$$H_I = \sqrt{12(1+\nu)}\frac{R}{n}, \quad (12)$$

where: ν is Poisson's ratio.

Eq. (12) is verified by the authors using a total of 2400 finite element analyses.

Necessary stiffness of intermediate stiffening rings is determined by Zeybek et al. (2015). Stiffness ratio χ could be expressed as:

$$\chi = \frac{K_{shell}}{K_{stiffener}} = \frac{Rt\left(AR^2 + I_x^2(n^2-1)\right)}{12\sqrt{3}(1+\nu)^{1.5}AI_x n(n^2-1)^2}, \quad (13)$$

where: K_{shell} is circumferential stiffness of the shell; $K_{\text{stiffener}}$ - circumferential stiffness of circular ring; A - cross sectional area of the stiffening ring; I_{x} - moment of inertia of the stiffening ring about vertical axis "*x*-*x*".

The results in research of Zeybek et al. (2015) indicate that ratios below about $\chi < 0.2$ provide a satisfactorily uniform axial membrane stress distribution above the intermediate ring stiffener, so this limit is recommended for practical design. In his later research Zeybek et al. (2017) confirmed, that correlation smaller than $\chi < 0.2$ are sufficient even when the rings are placed under their ideal position.

It should be noted that all above mentioned researches are done with smooth steel shells, without vertical stiffeners in them. On other side, common practice in design of steel structures is to place stiffening elements on the point, where are applied concentrated loads. In our case, the stiffeners should be placed above the discrete supports, see Fig. 2.

Fig. 2. Stiffening elements above discrete supports of the shell.

Here the question is, how tall could be these stiffeners? The reasonable approach is vertical stiffening elements to reach the level in which there is an equalization of the values of the meridional normal stresses above the supports and in the middle between supports. Under this level the cylindrical shell will be considered as a part of ring beam, stiffened by elements above the supports. Above it, cylinder can be modelled as continuously supported shell. But where is the position of this level? Values of critical height H_{cr} of the shell and ideal position H_l of intermediate stiffening ring are very different between themselves. Furthermore, in his research Zdravkov (2017a) shows that when there are vertical stiffening elements without stiffening ring in the upper end, the height of the critical zone in which are distributed vertical reactions of discrete supports, is increased. In other words as longer are the stiffeners, as higher will be the critical zone. Therefore, there is a certain level, placement of stiffening elements over it is not only pointless, but even harmful. In the present article the author will try to determine the limits of this level.

2. Finite Element Analysis

For the purpose of research, tree steel cylindrical shells are modelled, using software ANSYS. Their parameters are as follow:

a) dimensions:
- shell 1 – diameter D = 3 m, height H = 6 m;
- shell 2 – diameter D = 4 m, height H = 8 m;
- shell 3 – diameter D = 5 m, height H = 10m.

b) all shells are with constant thickness t = 5 mm.

c) all shells are supported by six immovable supports with dimensions in plane 125×125 mm, see Fig. 3.

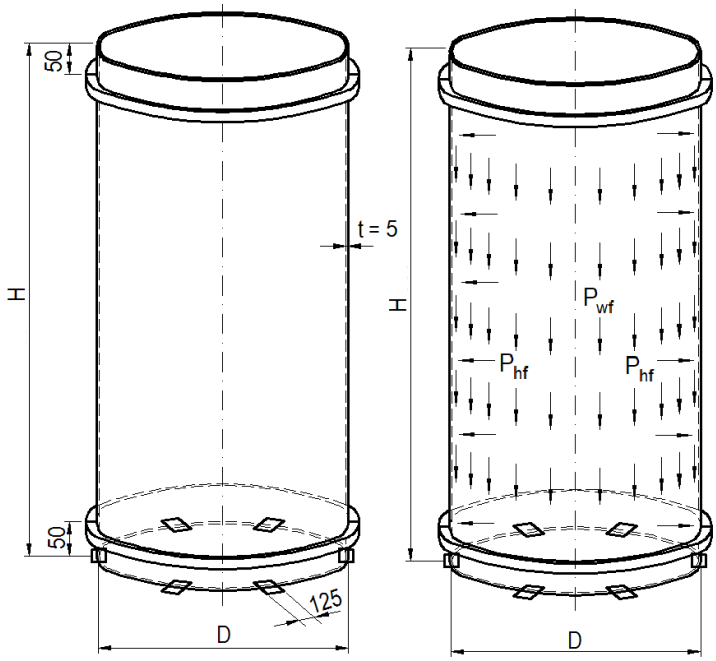

Fig. 3. Numerical models – dimensions and loading.

d) in order to strengthen the shells in radial direction, on 50mm above the lower edge and on 50mm below the upper edge are placed rings with section L100x8 mm, welded as is shown on Fig. 6 ;

e) the stored in the facilities product varies. For each shell it is as follow:
- shell 1 – cement;
- shell 2 – lime;
- shell 3 – sand.

Every product causes horizontal pressure P_{hf} and vertical P_{wf} load due to the friction between the stored material and the shell. Their values are determined for every particular product according to standard EN 1991-4. All loads are uniformly distributed and applied as a surface pressure on the shell. They are applied to internal surface of the shells.

f) shells 1, 2 and 3 are researched in six different types of the stiffening on the supports:

- models without stiffeners above the supports, see Fig. 4a;
- the shells are is stiffened with an intermediate ring with section L100x8 mm, see Fig. 4b. Above every support are placed 2 steel plates with section 8x100 mm, which reach the intermediate ring.

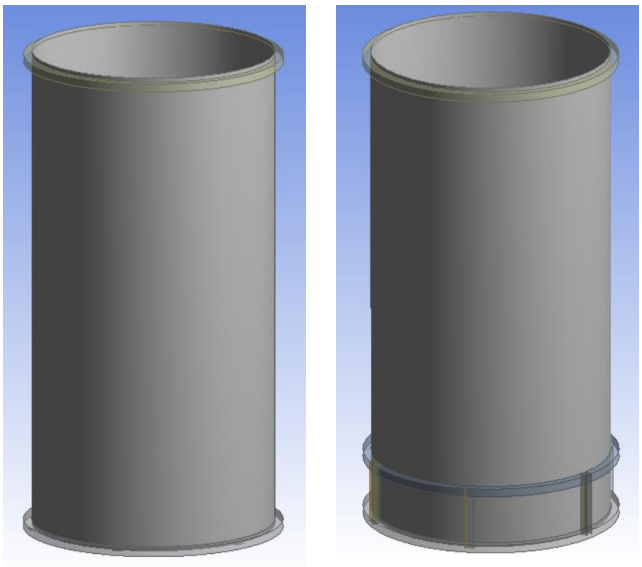

a) shell without vertical stiffeners

b) shell with vertical stiffeners

Fig. 4. Vertical stiffening elements on the cylindrical shell.

The levels of intermediate stiffening ring are calculated as follow:

- using an average value of distribution of discrete forces F_R from supports α = 45°, see Fig. 5. The height H_{45} is determined with the expression:

$$H_{45} = \frac{\pi R}{n}. \quad (14)$$

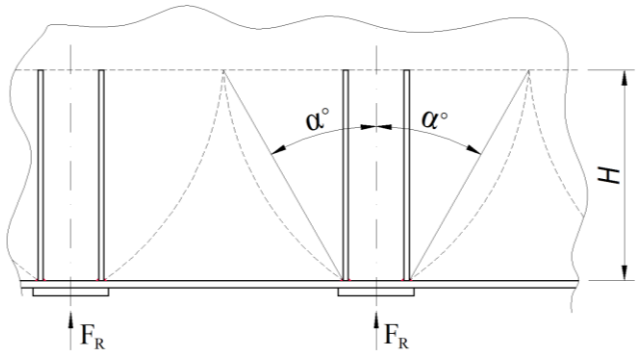

Fig. 5. Average angle α of distribution of the compressive forces on height.

- at ideal position of the intermediate stiffening ring on the shell. The height H_I will be calculated by the formula (12);
- using an average value of distribution of discrete forces F_R from supports α = 30°. The height H_{30} should be calculated by the formula:

$$H_{30} = \frac{\pi R}{n} tan(90° - \alpha°), \quad (15)$$

- the length of the stiffeners H_L is equal to distance between the supports. It is calculated according to the formula:

$$H_L = \frac{2\pi R}{n}, \quad (1)$$

- the height of the stiffeners is equal to the critical height H_{cr} of the shell, which is calculated according to the formula (11).

g) material of elements is steel S235, with a properties according to European standard EN 10025-2:2004.

The angular section L100x8 and a part of the cylindrical shell form an intermediate stiffening ring with a shape as is shown on Fig. 6.

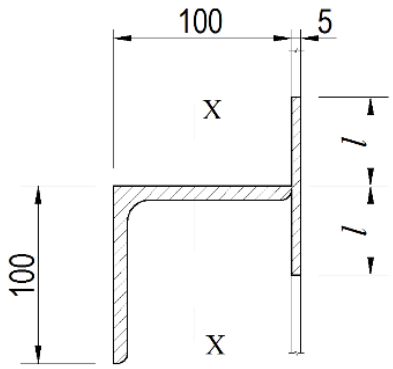

Fig. 6. Shape of the intermediate stiffening ring.

Effective width l of the steel sheets over and below the joint is calculated according to the standard API 650, by the expression:

$$l \leq 13.4\sqrt{Dt}, \quad (17)$$

where: D is a diameter of the cylindrical shell, m; t – thickness of the cylindrical shell, mm.

Effective width l for the shells with the smallest diameter, D = 3 m, is l = 51.9 mm. I accept to have effective width l = 50 mm for all shells. It is on way of safety.

The geometric characteristics of the obtained stiffening ring are:

a) area - A = 20.5 cm^2 ;

b) moment of inertia about vertical axis "x-x" - I_x=358.4 cm^4.

For different shells, the ratio of the stiffness's χ, calculated according to the formula (13), has the values as follow:

- shell 1 – χ = 0.042;
- shell 2 – χ = 0.0764;
- shell 3 – χ = 0.130.

The maximum value of the ratio χ = 0.130 < 0.2, so it could be expected that the stiffness of the intermediate ring will be sufficient to equalize the meridional stresses in the shell above it.

The shells are modeled by 2D quad elements "Shell 181" with maximum dimensions of 50 mm. The method of their creation is “All quad”. Element’s midside nodes are controlled by program.

Thin shell structures are sensitive for effect of changes of geometry during loading. On that reason geometrically nonlinear analyses (GNIA) are used, according to the recommendations of EN 1993-1-6.

ANSYS’s option “symmetry” is activated to reduce a calculation time. In analysis is used a quarter of silo only.

Axial normal stresses are accounted by the height of shell, in the middle between two supports and above the supports. After that are determined the values of ratio $\sigma_{x,m}/\sigma_{x,s}$, where:

$\sigma_{x,m}$ is meridional normal stress by height of the cylinder, in the middle between two supports;

$\sigma_{x,s}$ – meridional normal stress by height, above the supports.

The idea is that where the ratio $\sigma_{x,m}/\sigma_{x,s}$ =1.0 , is the upper border of the critical zone in the shell, in which are redistributed vertical reactions of supports. Above that border circumferential nonuniformity in the axial membrane stresses does not exists and the shell is continuously supported.

The study continues with a buckling analysis. This solution gives the load multiplier "k", which can be assumed as a reserve of the bearing capacity of the shell. The reserve k gives a quantity assessment of the influence of the different height of the vertical stiffeners on the bearing capacity of the shell.

3. Analysis Results

In the charts below, see Fig. 7, could be seen the accounted through numerical methods change in the ratio $\sigma_{x,m}/\sigma_{x,s}$ by the height of the shell.

Obviously, the presence of an intermediate stiffening ring above the supports is favourable. It limits the inequality of the meridional stresses above it.

The Fig. 7 shows ratios $\sigma_{x,m}/\sigma_{x,s} > 1.0$. It means that in part of the shell the axial stresses in the middle between the supports are bigger than the stresses above the supports. A similar phenomenon has been observed in previous researches of Zdravkov (2017a, 2017b). This effect is underlined in shells without intermediate rings, in which could be reported values of the ratio $\sigma_{x,m}/\sigma_{x,s} > 2.0$.

It could be seen that as longer are the vertical stiffening elements as bigger are the ratios $\sigma_{x,m}/\sigma_{x,s}$ above their upper end, i.e. the inequality of the stresses above them is smaller. Exceptions here are the stiffening elements with height $h = H_{cr}$.

The results of the performed Buckling Analysis for each of shells are as follows:

a) shell 1
- there are no vertical stiffeners – k = 8.809;
- H_{45} = 785 mm – k = 26.392;
- H_{I} = 1185 mm - k = 29.789;
- H_{30} = 1360 mm - k = 30.767;
- H_{L} = 1571 mm - k = 31.527;
- H_{cr} = 2890 mm - k = 32.072.

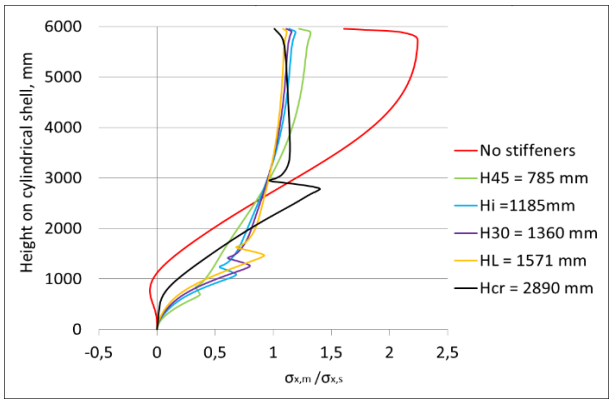

a) shell 1 – diameter D = 3 m, height H = 6 m

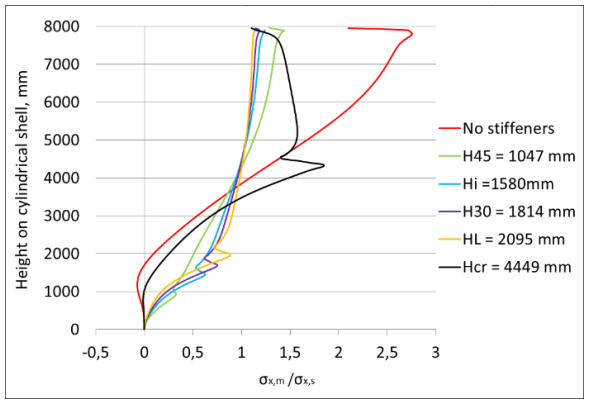

b) shell 2 – diameter D = 4 m, height H = 8 m

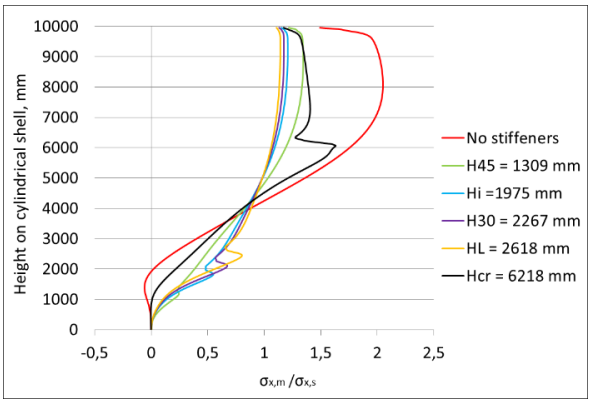

c) shell 3 – diameter D = 5 m, height H = 10m

Fig. 7. Change of ratio $\sigma_{x,m}/\sigma_{x,s}$ by the height of the cylindrical shell.

b) shell 2
- there are no vertical stiffeners – k = 5.719;
- H_{45} = 1047 mm – k = 19.478;
- H_{I} = 1580 mm - k = 21.872;
- H_{30} = 1814 mm - k = 22.387;
- H_{L} = 2095 mm - k = 22.731;
- H_{cr} = 4449 mm - k = 22.474.

c) shell 3
- there are no vertical stiffeners – k = 1.571;
- H_{45} = 1309 mm – k = 3.293;
- H_{I} = 1975 mm - k = 3.548;
- H_{30} = 2267 mm - k = 3.622;
- H_{L} = 2618 mm - k = 3.688;
- H_{cr} = 6218 mm - k = 3.835.

It is obvious that the using of vertical stiffening elements considerably increase bearing capacity of the shell on meridional loading. Longer stiffeners assure bigger reserve of bearing capacity. The effect is not linear and decrease with elongation of stiffeners. Therefore, the author would recommend the use of the vertical stiffening elements with length $H_l \le h \le H_L$.

When the researched shells do not have vertical stiffeners, loss of stability is caused by the axial stresses $\sigma_{x,s}$. The buckled zone is just above the supports, see Fig. 8a. When the shells have vertical stiffening elements and a horizontal ring above them, the loss of stability is caused by shear stresses. The zone of buckling is on both sides of the vertical stiffeners, see Fig. 8b.

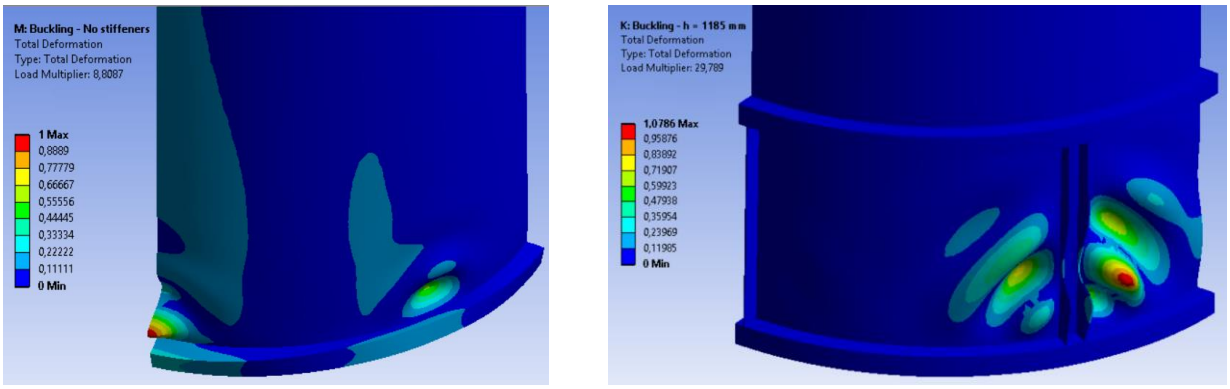

a) shell without vertical stiffeners b) shell with vertical stiffeners

Fig. 8. Modes of buckling of the cylindrical shell.

4. Conclusions

Common practice in design of steel silos is to place stiffening elements in applying point of concentrated loads. In our case the stiffeners are placed above the discrete supports. As a result, bearing capacity of the shell on meridional loads increases. Longer stiffeners assure bigger bearing capacity, but the effect decreases with elongation of stiffeners.

In his researches, Zdravkov (2017a, 2107b, 2018) shows that equalizing of the axial normal stresses on the height depends on a lot of factors. As a presence, by vertical stiffeners and/or intermediate rings, value of internal pressure, ratio D/t and other. On that reason the author cannot state exactly how long should be the stiffening elements. As a conclusion of this research can recommend the limits of the length h of the stiffeners. According to the author, it should be $H_l \le h \le H_L$. When the height $h \le H_l$, ratio $\sigma_{x,m}/\sigma_{x,s} < 0.6$, in other words there is a large inequality in the meridional normal stresses above the upper end of the stiffeners. There is no much sense to use stiffeners with a length $h > H_L$, because the effect of their elongation above these values is too small. Beside of it the longer stiffening elements lead to ratio $\sigma_{x,m}/\sigma_{x,s} > 1.0$ in their upper end.

References

ANSYS 17 (2016). Ansys Inc. Canonsburg, PA, USA.

API Standard 650 (2013). Welded Tanks for Oil Storage. Twelfth Edition, American Petroleum institute.

Calladine CR (1983). Theory of Shell Structures. Cambridge University Press, Cambridge, U.K.

EN 1991-4:2006 (2006). Actions on structures - Part 4: Silos and tanks, European committee for standardization, Brussels.

EN 1993-1-6:2007 (2007). Design of steel structures - Part 1-6: Strength and Stability of Shell Structures, European committee for standardization, Brussels.

EN 1993-4-1:2007 (2007). Design of steel structures - Part 4-1: Silos, European committee for standardization, Brussels.

EN 10025-2:2004 (2004), Hot rolled products of structural steels - Part 2: Technical delivery conditions for non-alloy structural steels.

Rotter JM (1985). Analysis and design of ringbeams. *Design of Steel Bins for Storage of Bulk Solids*, J. M. Rotter, ed., University of Sydney, Sydney, Australia, 164-183.

Topkaya C, Rotter JM (2011a). Ring beam stiffness criterion for column supported metal silos. *ASCE Journal of Engineering Mechanics*, 134, 846-853.

Topkaya C, Rotter JM (2011b). Stiffness of silo supporting ring beams resting on discrete supports. *6th International Conference on Thin-Walled Structures*, Timisoara, Romania.

Topkaya C, Rotter JM (2014). Ideal location of intermediate ring stiffeners on discretely supported cylindrical shells. *Journal of Engineering Mechanics*, 140(4), 04013001.

Vlasov VZ (1961). Thin-walled Elastic Beams. National Science Foundation, Washington, DC.

Vlasov VZ (1964). General Theory of Shells and Its Applications in Engineering. NASA Technical Translation, TTF-99, Washington, DC.

Zeybek Ö, Topkaya C, Rotter JM (2015). Strength and stiffness requirements for intermediate ring stiffeners on discretely cylindrical shells. *Thin- Walled structures*, 96, 64-74.

Zeybek Ö, Topkaya C, Rotter JM (2017). Requirements for intermediate ring stiffeners placed below the ideal location on discretely supported shells. *Thin-Walled structures*, 115, 21-33.

Zdravkov LA (2017a). Vertical stiffeners and internal pressure - influencing factors on distribution of meridional stresses in steel silos on discrete supports. *Challenge Journal of Structural Mechanics,* 3(3), 123-128.

Zdravkov LA (2017b). Influence of intermediate rings and height of skirt on effective width of compression zone in junction column - cylindrical shell of steel silo. *International Jubilee Scientific Conference "75th Anniversary of UACEG"*, Sofia.

Zdravkov LA (2018). Influencing factors on effective width of compressed zone in joint column - cylindrical shell of steel silo. *Challenge Journal of Structural Mechanics,* 4(1), 1-8.

Challenge Journal of Structural Mechanics

Research Article

Earthquake performance of collapsed school building under Van-Tabanli (Mw=7.2) earthquake

Cumhur Cosgun [a,*], Atakan Mangir [b]

[a] *College of Information Technology and Engineering, Marshall University, Huntington, WV 25755, USA*
[b] *Institute of Graduate Studies in Science and Engineering, İstanbul University, 34320 İstanbul, Turkey*

ABSTRACT

A majority of the present building stock of Turkey is under seismic risk. It is believed that a significant proportion of the existing structures will either collapse or will get heavily damaged during a possible strong earthquake. With this respect, as an initial stage in the betterment of the structurally deficient building stock, assessment of existing buildings is of vital importance. From this viewpoint, in this study, earthquake performance of a collapsed school building was investigated through numerical performance analysis based on codified rules. At the end of 2011, numerous ground motions of various intensities have been registered in city of Van in eastern Turkey starting from 23 October 2011. Two major earthquakes were experienced at the Tabanli and Edremit district of Van. The moment magnitudes of these earthquakes were announced as 7.2 and 5.6, respectively. The investigated school building in this study was located in the city of Van and collapsed after first major earthquake (Mw=7.2). Structural details of the load-bearing members of the investigated building including as-built drawings and specified material properties were obtained. Based on obtained data, a numerical model was created to simulate the behavior of the building under code specified earthquake effects. Earthquake performance assessment of the structure was carried based on the recommendations given in the related chapter of the Turkish Seismic Code. Pushover analyses were performed and expected member by member damage levels and overall structural damage were determined in accordance with Turkish Seismic Code. The results are discussed to enlighten the actual cause of the collapse.

ARTICLE INFO

Article history:
Received 5 September 2018
Revised 12 October 2018
Accepted 30 October 2018

Keywords:
Collapsed school building
Earthquake performance
Nonlinear static analysis
Damage evaluation

1. Introduction

A majority of the present building stock of Turkey is under seismic risk. With this respect, it is believed that a significant proportion of the existing structures will either collapse or will get heavily damaged during a possible strong earthquake. This is well supported by the consequences of the previous earthquakes that occurred in the region (1992 Erzincan, 1995 Dinar, 1998 Adana-Ceyhan, 1999 Kocaeli and Düzce).

At the end of 2011, numerous ground motions of various intensities have been registered in city of Van in Turkey starting from 23 October 2011. Two major earthquakes were experienced at the Tabanli and Edremit district of Van. The moment magnitudes of these earthquakes were announced as 7.2 and 5.6, respectively, by United States Geological Survey (USGS). In these seismic events 604 people lost their life and 1000 buildings were either heavily damaged or collapsed. More than 600,000 people were reported to have been affected by the earthquakes in that period (Cosgun et al., 2013).

A major part of earthquake prone areas in the world hold sub-standard building stocks. Buildings constructed with poor reinforcement details, low strength concrete (under 10 MPa) and reinforcing bars with plain surfaces generally suffer from earthquakes due to low

* *Corresponding author*. Tel.: +1-304-972-2699 ; Fax: +1-304-696-5454 ; E-mail address: cosgun@marshall.edu (C. Cosgun)
ISSN: 2149-8024 / DOI: https://doi.org/10.20528/cjsmec.2018.04.004

deformation and lateral load-carrying capacity (Ilki et al., 2009; Bedirhanoglu et al., 2010; Cosgun et al., 2013; Turk et al., 2013). These buildings are urgently needed to be either reconstructed or strengthened to reduce human losses in possible future strong seismic events. During the structural renewing of sub-standard buildings, efficient numerical simulation and assessment methodologies will considerably contribute to the reduction of damages in future earthquakes. On the other hand, the real cases experienced in past earthquakes are quite important to evaluate the efficiency of these numerical simulation approaches and code-specified member performance criteria. Isik and Kutanis (2015) have conducted performance-based assessment for existing residential buildings to investigate the seismicity of the region, recently.

During the aforementioned seismic events in the city of Van, unfortunately, some government buildings were heavily damaged or collapsed. One of these collapsed buildings is the Gedikbulak school building. This building is the only school building that collapsed in the region. Fortunately, at the time of collapse there were no students or staff nor any visitors inside the building. In this study, this building was chosen to investigate the earthquake performance by using numerical simulation based on present seismic code requirements for the assessment of existing RC buildings. Nonlinear pushover analyses were carried out for the building for both orthogonal lateral directions. During the nonlinear seismic performance assessment analyses, the design blue prints were taken into consideration. Therefore, the main purpose of the study is to check the suitability or safety of the design approach followed during the construction of the school building. Finally, seismic performance levels defined in the current code of practice were used to compare with strength and drift estimations from the numerical simulations. Inel and Meral (2016)'s study also shows the approach of Turkish Seismic Code (TSC, 2007) on the seismic performance of RC buildings subjected to past earthquakes in Turkey and encountered damage types from the effects of previous earthquakes.

2. Strong Ground Motion Records and Spectral Characteristics

Local coordinates of the Mw=7.2 Tabanli and Mw=5.6 Edremit earthquakes are reported as 38.689N–43.465E and 38.447N–43.263E, respectively (AFAD). While the maximum PGA values recorded during the Tabanli earthquake at the Muradiye station for NS, EW, and Vertical directions are 0.182g, 0.173g, and 0.081g, respectively, the maximum PGA values recorded during the Edremit earthquake at the Van Merkez station in the NS, EW, and Vertical directions, are 0.151g, 0.251g, and 0.153g, respectively. For the Tabanli earthquake, the processed time histories yield peak ground velocities of 27.3 cm/s, 14.8 cm/s, and 5.9 cm/s for the NS, EW, and Vertical components, respectively; whereas the maximum peak ground displacement is obtained as 5.5 cm for the NS component (Tapan et al., 2013). For the Edremit earthquake, peak ground velocities of 17.3 cm/s, 32.1 cm/s, and 6.3 cm/s are obtained for the NS, EW, and Vertical components, respectively; whereas the maximum peak ground displacement is calculated as 6.8 cm for the EW component (Tapan et al., 2013). The 5% damped acceleration response spectra obtained from the records of the Tabanli and Edremit earthquakes are compared with the 2007 Turkish Seismic Code (TSC, 2007) spectrum in Fig. 1, defined for seismic zone 1 (PGA=0.4g) for Van and for all soil classes, where Z1 represents the most stiff soil condition and Z4 the softest. In the TSC (2007), the shortest period range for a maximum spectral amplification value of 2.5 is defined between period values of TA=0.10s and TB=0.30s for soil class Z1, and the longest period range is defined between period values of TA=0.20s and TB=0.90s for soil class Z4. As seen in Fig. 1, none of the records exceed the design spectra.

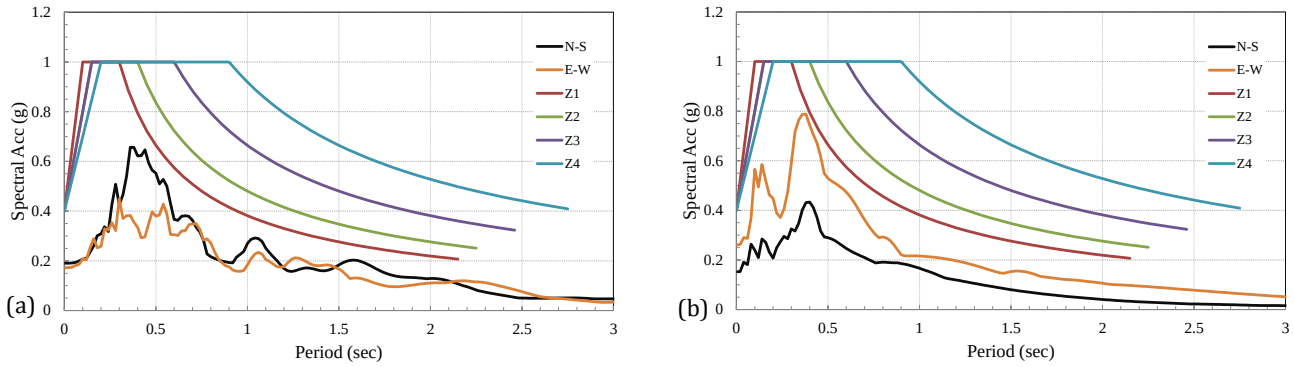

Fig. 1. Comparison of (a) first (Muradiye station) and (b) second earthquake (Van Merkez station) response spectrum with TSC (2007) design spectrum.

3. Outline of Investigated School Building

School buildings in the city center and districts are generally low-rise reinforced concrete structures with shear walls. While, owing to presence of sufficient amount of shear walls in two main orthogonal directions and the regular structural systems, most of these school buildings have performed well, without experiencing considerable damage, few school buildings have experienced widespread damage in partition walls. Considering the possibility of school buildings to be used as shelters after earthquakes, this type of non-structural damage

should also be avoided through proper construction of the partition walls. Few schools, particularly relatively older ones without shear walls, experienced slight to moderate structural damage as well. However, among all the above-mentioned school buildings, there was one school building (Gedikbulak school building) that totally collapsed.

The structure is a 3-storey building which was constructed in 1988 having dimensions 14.4 by 21.6 m in plan. It has four spans in both E-W (X) and N-S (Y) directions. The story height of all stories is 3.2 m. The typical architectural and structural floor plans of the building is shown in Fig. 2. View of the collapsed school building is also given in Fig. 3.

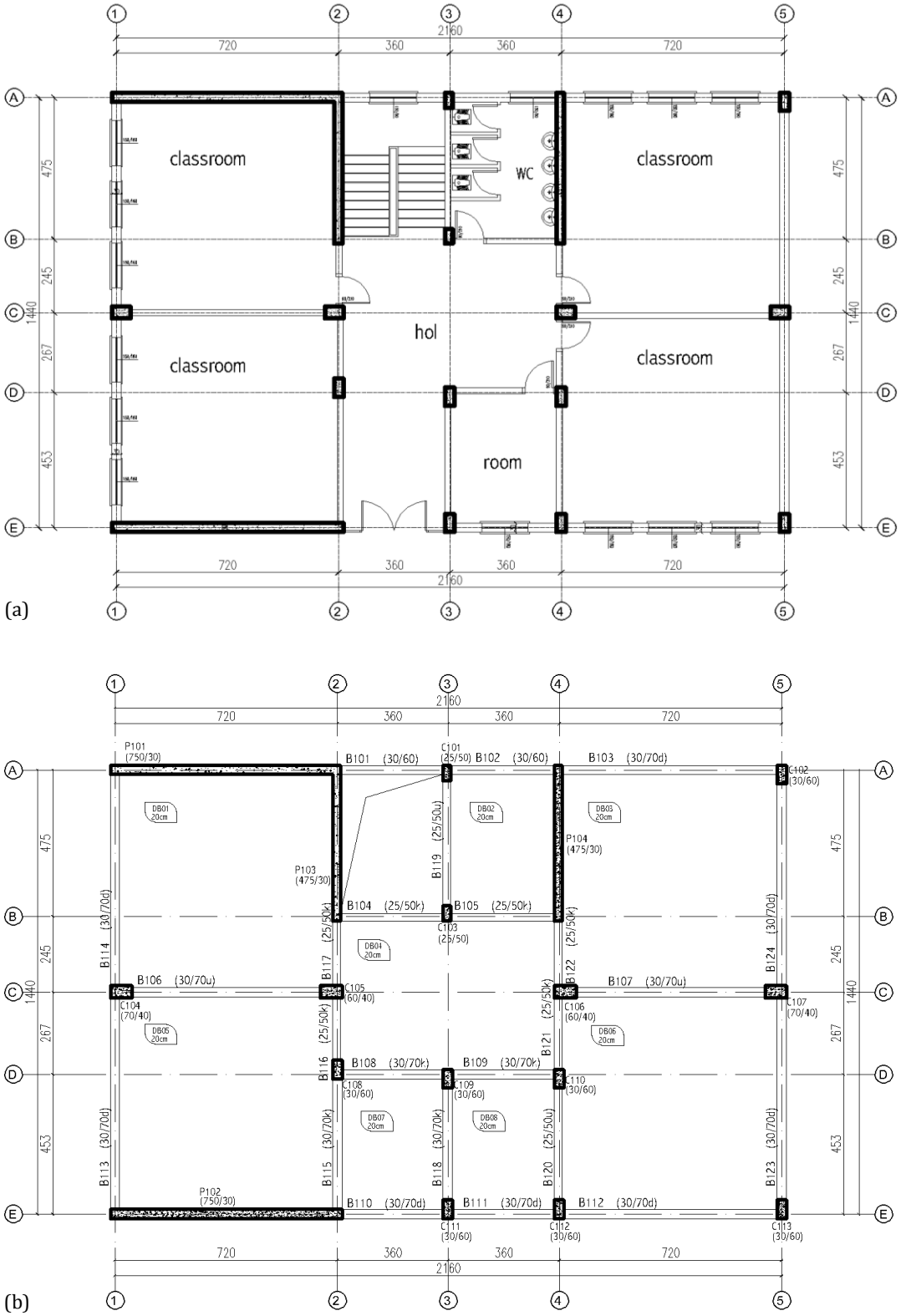

Fig. 2. (a) Architectural and (b) Structural floor plans of the collapsed school building.

Fig. 3. View of the collapsed school building.

Information regarding the structural system plan and geometric details of the structural members were obtained by in-situ investigation. As-built drawings of the building were also available and these were used to cross-check the in-situ investigation findings. The cross-section details of the building columns and beams are shown in Figs. 4 and 5. The building was constructed with two-way reinforced concrete slabs having thickness of 200 mm. Main differences between the section types are the dimensions and longitudinal reinforcement configuration. The building has 2 types of shear walls with two different cross-section geometries as rectangular and L-shaped. Both types of shear walls include ϕ18 bars as longitudinal reinforcement on first floor. On upper floors, shear walls have same dimensions but with ϕ14 bars. Layout of the geometric cross-sectional details of structural members is given on the floor plan in Fig. 2. Plain bar type reinforcements were used for all the structural members of the building

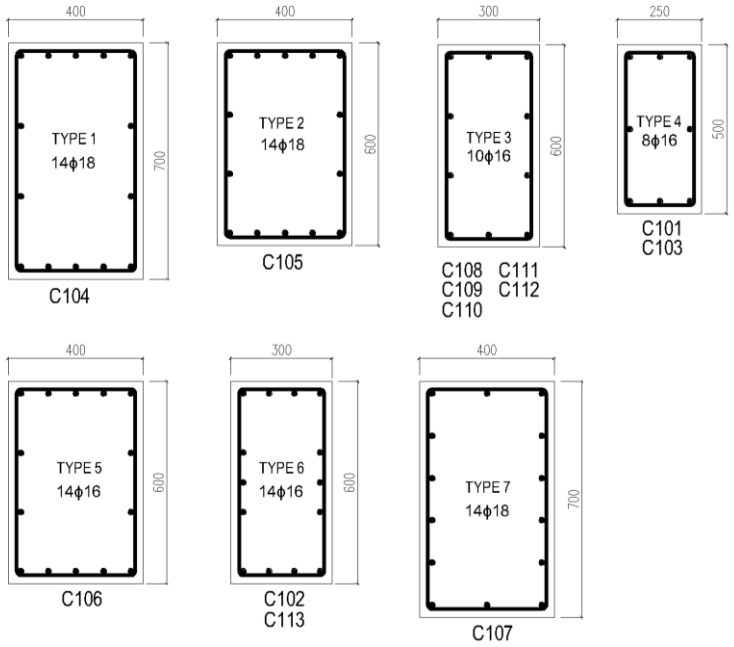

Fig. 4. The geometry and structural details of column cross sections.

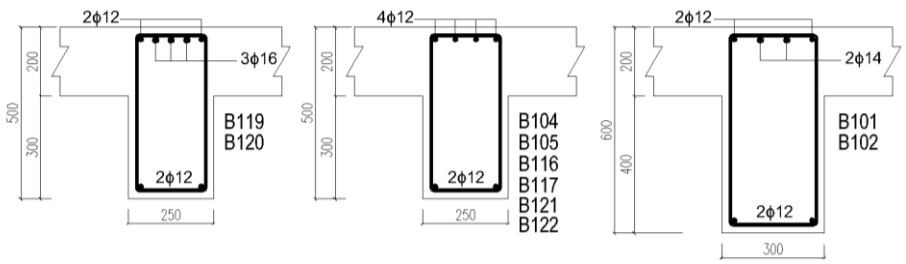

Fig. 5. The geometry and structural details of beam cross sections.

4. Damage Outline and Construction Errors

Damage outline of the collapsed building is presented under this chapter. Fig. 6 presents post-earthquake photographs of this collapsed building. Also, in Fig. 7, a close-up photograph of one of the failed shear walls in the building at first floor level is shown. It is observed that the shear walls were lacking all necessary conditions that are dictated by the related Turkish Seismic Design Code (TSC, 2007). These include inadequate lap splices, poor reinforcement details, insufficient concrete strength and the use of plain reinforcement bars. Some of these deficiencies can also be observed from the buildings in Kütahya region of Turkey after 2011 Simav earthquake (Yön et al., 2013).

Fig. 6. Photos of the collapsed school building.

As will be demonstrated in the following pages, the nonlinear static analysis of the building carried out by assuming the project member sizes and reinforcement details has revealed that the structural system appears to be adequate, in terms of stiffness and strength, to withstand these moderate-level earthquakes without total collapse. However, the deficiencies in reinforcement detailing such as insufficient anchorage of the beam longitudinal bars into the shear walls (see Fig. 6), low stirrup spacing and the lack of hooks of lateral reinforcement, and inadequate lap splices of the longitudinal bars of the shear walls seem to have impaired the efficiency of the shear walls, remarkably (see Fig. 7). The collapse mechanisms encountered in this observation can be compared and discussed with the study on the seismic behavior of a reinforced concrete building collapsed during the 2009 L'Aquila earthquake (Palermo et al. 2014). In 2009 L'Aquila earthquake, some of the buildings were totally collapsed building revealed that most of the columns at the ground story level failed in shear with some evident buckling of the longitudinal bars (no transverse reinforcement in the joint region).

5. Nonlinear Static Analysis

Seismic assessment of existing structures are complicated work which generally requires more sophisticated analyses than performing a new design (Ni, 2014). Carvalho et al. (2013) have compared different modelling approaches for nonlinear static and dynamic analyses of reinforced concrete buildings. In this study, three dimensional analyses were conducted using the structural analysis program SAP2000 (CSI, 2016) for static and dynamic analysis of structure. The cross-section properties like moment-curvature capacities for beam ends and normal force – moment (P-M) interaction curves for shear wall ends were calculated by using the XTRACT software (IMBSEN software systems, 2004). A description of the modelling details is provided as follows. A three-dimensional model of the structure which is shown in Fig. 8 was created with the software to carry out the nonlinear static analysis. Beam and column elements were modelled as nonlinear frame elements with lumped plasticity by defining plastic hinges at both ends of the beams and both ends of the columns. Theoretical

zero distances were assumed for the plastic hinge locations. Shear walls are modelled like frame members by defining the geometric properties of shear walls. The user defined flexural hinge properties were determined by the moment–curvature and P-M interaction analyses of each structural element by means of the section analysis software. Moment – rotation diagrams of beams and P-M interaction diagrams of shear-walls are gathered from the analysis by XTRACT software. And for columns, SAP2000's sectional plastic analysis configuration is used.

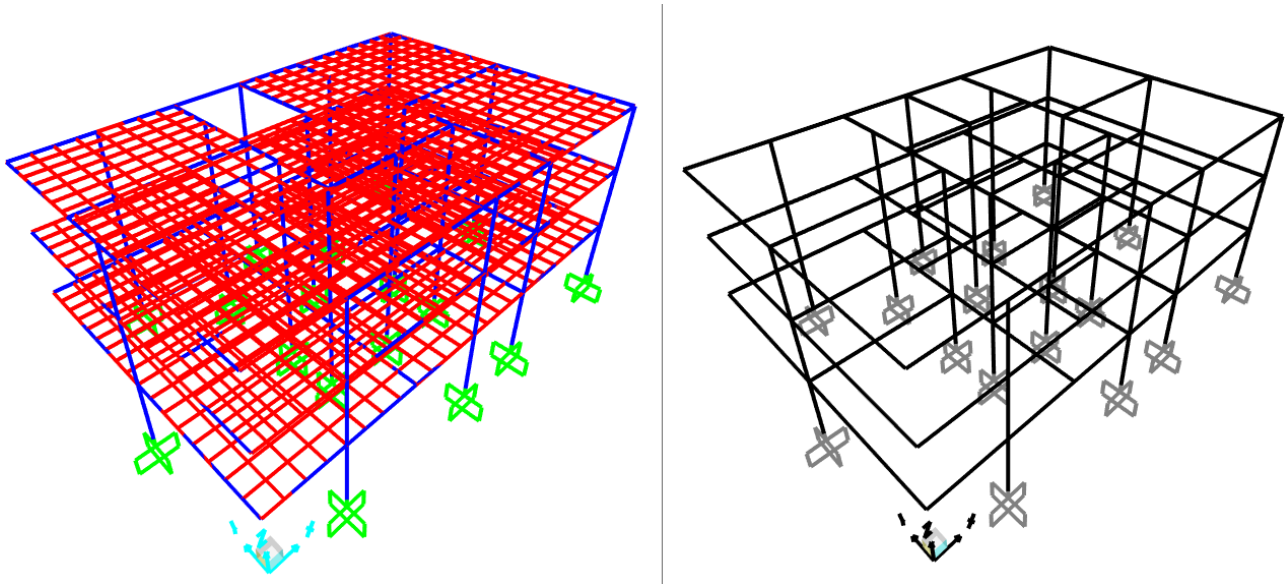

Fig. 8. 3D model of the structure.

The nonlinear behavior of columns and beams are taken into consideration through the defined plastic hinges at the critical locations where moments are maximum. The inelastic moment-rotation relationships of columns and beams are obtained through fiber analysis using build-in SAP2000 tools and XTRACT software, respectively. The reason of using SAP2000 built-in tool for determination of moment-rotation relationship of columns is the variation of axial loads on the columns, which was not possible to take into consideration for moment-rotation relationships to be obtained using XTRACT software, which takes into account a constant axial load for the member. On the other hand, use of XTRACT software for the moment-rotation relationships of the beams does not pose any problem since axial loads on the beams are marginally small. The moment-rotation relationships for beams are obtained through XTRACT software rather than SAP2000 due to more practical data input interface of XTRACT. It should also be noted that after determination of P-M relationship for columns, SAP2000 assumes a bilinear moment-rotation relationship with a horizontal branch after yielding. The material models for the unconfined concrete (f_c=10 MPa), confined concrete and the typical steel stress–strain model with strain hardening for steel (f_y=220 MPa) used in the moment–curvature analyses is given in Figs. 9 and 10. These material models are specified in related TSC (2007) code which states to use Mander and Priestley's material model for confined concrete (Mander et al., 1988). Live load on the structure is defined as 3.5 kN/m^2 and 2.0 kN/m^2 floor covering load is defined. Dead load is automatically calculated by the software.

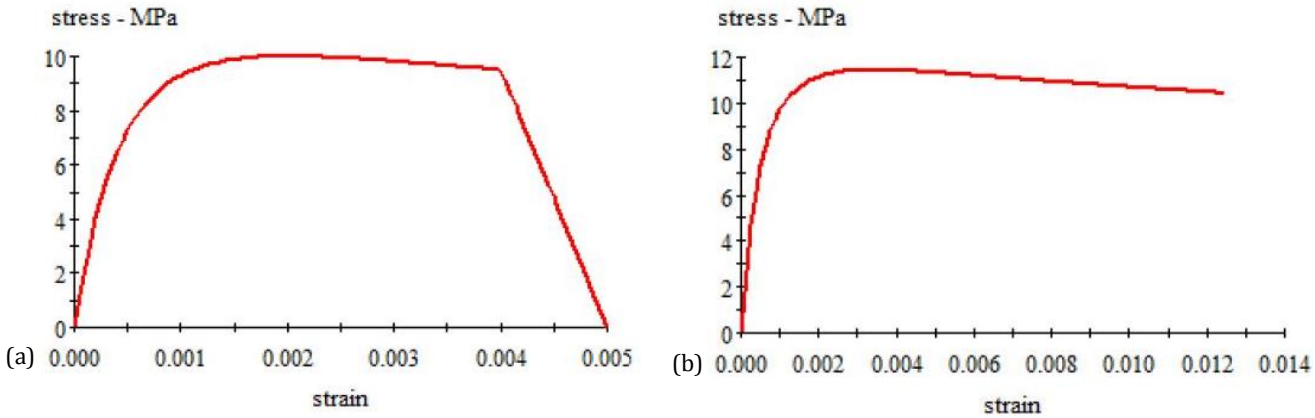

Fig. 9. (a) Unconfined and (b) Confined concrete material models used in the analysis for C10.

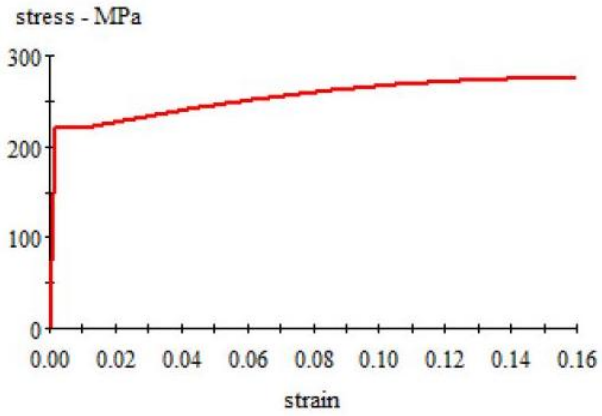

Fig. 10. Stress–strain model with strain hardening for reinforcing steel (f_y=220 MPa).

The cracked section stiffness for RC beams was assumed as 0.4 times of EI (flexural rigidity of cross section) according to TSC (2007). As stated in TSC (2007), live load participation for school buildings is given as "0.6" and the cracked section stiffness for RC columns should be calculated after analysis of structure under "Dead Load + (live load participation factor) x (Live load)" combination. Cracked section stiffness values for RC columns are dependent on the axial load of those members under the combination mentioned above. Cracked section stiffness of each column and shear wall is calculated and defined in the software. Related rule in TSC (2007) is given below:

If $N_D / (A_c f_{cm}) \leq 0.10$ then $(EI)_c = 0.40\ (EI)$
If $N_D / (A_c f_{cm}) \geq 0.40$ then $(EI)_c = 0.80\ (EI)$
If $0.10 < N_D / (A_c f_{cm}) < 0.40$ then Interpolation for $(EI)_c$

where: N_D = axial force on member; A_c = cross sectional area of member; f_{cm} = compressive strength of concrete; EI = flexural rigidity of cross section; $(EI)_c$ = the cracked section stiffness.

In the nonlinear static (pushover) analysis, the behavior of the structure is characterized by the capacity curve that represents the relationship between the base shear force and top displacement. This is a very convenient representation in practice, and can easily be visualized by structural engineers. It is recognized that the structure's roof displacement is used for the capacity curve because it is widely accepted in practice. The structure is investigated in both orthogonal horizontal directions. Analysis case for x direction was named PushX while PushY was used for y direction. As analysis results, "pushover curves of both cases are converted to modal capacity diagrams and superposed with design earthquake spectrum with bilinear curves. Deflection demand curves for both cases are given in Figs. 11 and 12.

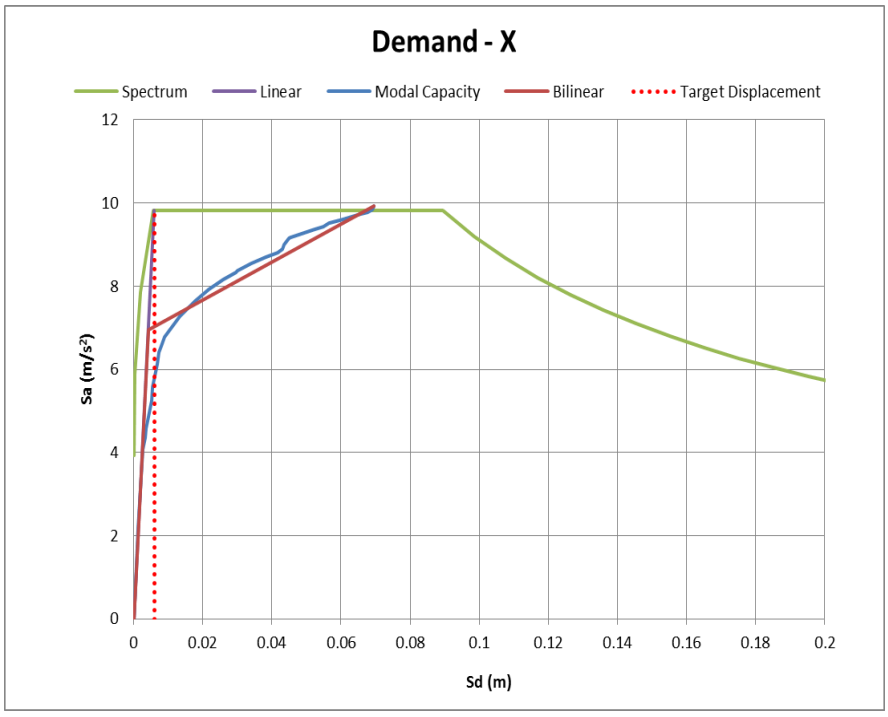

Fig. 11. Deflection demand for PushX case.

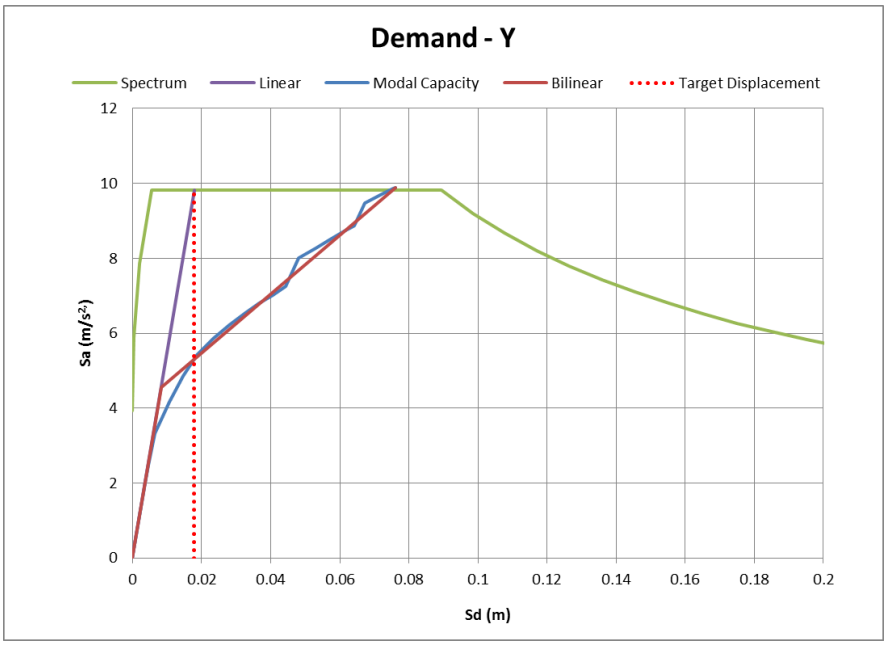

Fig. 12. Deflection demand for PushY case.

TSC (2007) specifies that the target displacement (S_{di}) gathered from the graph should be increased by multiplying the S_{di} value with modal participation factor (Γ_{i1}) and mode shape roof displacement (Φ_{iN1}) of related mode. The target roof displacements calculated for PushX case was calculated as 0.014 m and it was calculated as 0.040 m for PushY. The structure is re-pushed until target displacement values are reached and plastic hinge mechanisms in last step of both directions (PushX and PushY cases) are investigated. Plastic hinge formation pattern for the initial hinges and the hinges at target displacement state (PushX and PushY cases) are shown in Fig. 13.

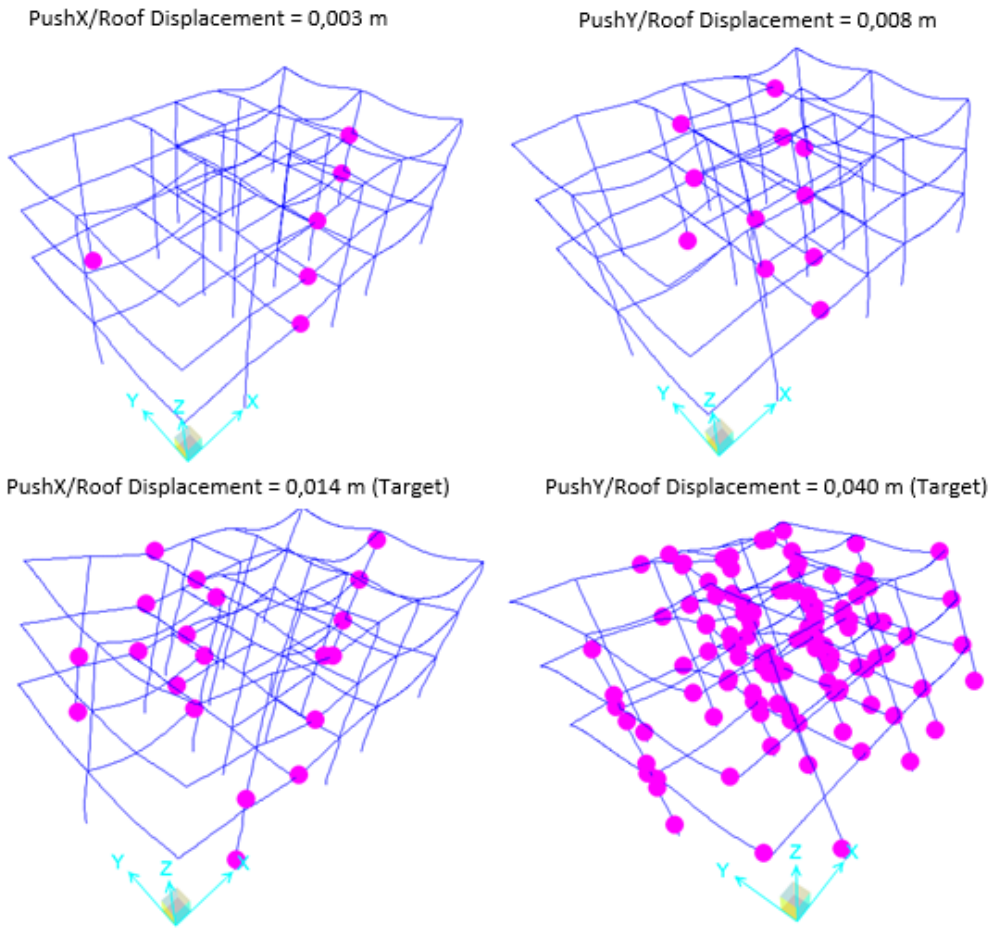

Fig. 13. Plastic hinge formation pattern for PushX and PushY cases.

As seen in these figures, according to design approach followed, plastic hinges occur on columns and beams. Therefore, it is obvious that the current capacity design principles were not followed properly during the design phase leading to weak columns and strong beams. Nevertheless, at target drift, the building is still in life safety performance level. Plastic hinge formation mechanisms were obtained at displacement points corresponding to the global yielding and ultimate displacements. The global yielding point corresponds to the displacement along the capacity curve in which the system starts to soften. No shear failure of structural members was detected in both cases. This was primarily due to the assumed low compressive strength of concrete and weak joint detailing. Thus, the overall behavior was dominated by the flexure and joint shear.

After the pushover analysis, plastic rotation of each hinge mechanism is checked for the rules given in TSC (2007). In the current Turkish Seismic Code, three different damage limits are defined in terms of plastic strain of concrete and steel for the evaluation of structural performance. Details of these damage limits are given in Table 1.

The code describes four different performance levels: Light Damage, Moderate Damage, Heavy Damage and Collapse, as shown in Fig. 14.

Table 1. Section damage limits given in TSC (2007).

Section Damage Limit	Unconfined Concrete		Confined Concrete	
	Strain of Concrete (ε_c)	Strain of Steel (ε_s)	Strain of Concrete (ε_c)	Strain of Steel (ε_s)
Minimum Damage Limit (MN)	0.0035	0.01	0.0035	0.01
Safety Limit (SL)	0.0035	0.04	0.0135	0.04
Failure Limit (FL)	0.0035	0.06	0.0180	0.06

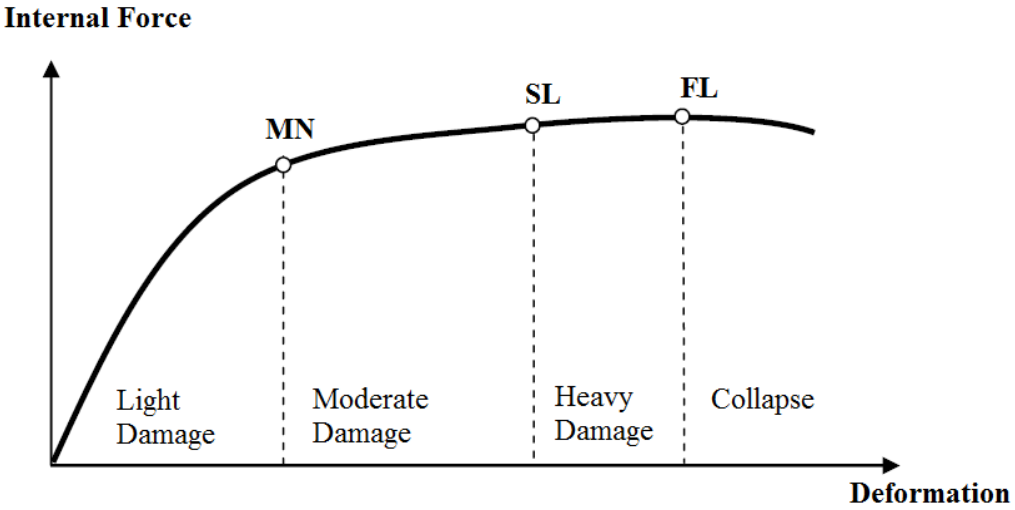

Fig. 14. Performance levels for structural members given in TSC (2007).

According to TSC (2007), plastic curvature demand of a structural member is found as;

$$\phi_p = 9\,\theta_p / L_p\,, \quad (1)$$

where; L_p is the plastic hinge length of member which is depth/2, θ_p values are the plastic rotation of hinges in last step of pushover analysis.

Total curvature demand is calculated by Eq. (2) as;

$$\phi_t = \phi_p + \phi_y\,, \quad (2)$$

where; ϕ_y is the curvature at first yield, gathered from cross-section analysis in XTRACT program for each section.

After calculating the total curvature demand ϕ_t, the compressive strain of concrete (ε_c) and tensile strain of reinforcement bars (ε_s) at that total curvature is found by sectional analysis in XTRACT software.

Storey drift ratio checks for both cases were made. A story drift ratio of 0.02 is given for Life Safety limit in TSC (2007). Storey drift ratio checks are given in Table 2 for both PushX and PushY cases. It is observed that story drift ratios calculated for both directions meet the Life Safety performance limits.

Table 2. Storey drift ratio checks for PushX and PushY cases.

Storey	h (m)	Push X	Storey Drift Ratio		Life Safety Limit	Control
		$\delta i_{\max}$ (m)	$\delta i / h$			
1	3.2	0.0039	0.0012	<	0.02	OK
2	3.2	0.0049	0.0015	<	0.02	OK
3	3.2	0.0050	0.0016	<	0.02	OK
Storey	h (m)	Push Y	Storey Drift Ratio		Life Safety Limit	Control
		$\delta i_{\max}$ (m)	$\delta i / h$			
1	3.2	0.0116	0.0036	<	0.02	OK
2	3.2	0.0136	0.0043	<	0.02	OK
3	3.2	0.0136	0.0043	<	0.02	OK

Shear Capacity Control of structural members are carried under the maximum shear demand ($V_{\max}$) gathered from PushX and PushY cases for different sections. According to TSC (2007), following shear calculations are used for shear failure assessment.

Concrete's contribution to section's shear strength is calculated with Eq. (3) as;

$$V_c = 0.8 \cdot 0.65 \cdot f_{ctm} \cdot b_w \cdot d(1 + 0.07 \cdot N/A_c)\,, \qquad (3)$$

where; f_{ctm} = tensile strength of concrete = $0.35\sqrt{f_{cm}}$; b_w = width of section; d = effective depth of tensile reinforcement; N = axial force on member; A_c = area of section.

Steel reinforcement bars' (stirrups) contribution to section's shear strength is calculated with Eq. (4) as;

$$V_s = A_s \cdot f_{ys} \cdot (d/s)\,, \qquad (4)$$

where; f_{ys} = yield strength of stirrups; A_s = Total area of stirrups; s = spacing of stirrups.

TSC (2007) states that if total sectional shear strength of member ($V_r = V_c + V_s$) is greater than maximum shear demand ($V_{\max}$) under the last step of Pushover analysis, the section is safe against shear failure. In Table 3, shear capacity control of different cross-sections is presented.

Table 3. Shear capacity control of members.

Structural Member Type	V_c (kN)	V_s (kN)	V_r (kN)	$V_{\max}$ (kN)		Control
			($V_c + V_s$)	PushX	PushY	
25/50 Beams	66.96	40.83	107.79	41.14	86.64	OK
30/60 Beams	97.84	49.72	147.56	28.99	38.97	OK
30/70 Beams	114.98	58.43	173.41	130.99	129.17	OK
Type 1 Columns	176.99	72.93	249.92	86.52	137.82	OK
Type 2 Columns	132.14	61.93	194.07	107.36	92.87	OK
Type 3 Columns	118.89	62.04	180.93	31.50	129.58	OK
Type 4 Columns	87.18	51.04	138.22	16.28	64.68	OK
Type 5 Columns	133.80	62.04	195.84	61.87	79.68	OK
Type 6 Columns	111.54	62.04	173.58	45.66	104.51	OK
Type 7 Columns	186.71	72.93	259.64	161.95	139.66	OK

Maximum shear demand (V_{max}) values are obtained for each cross-section type among all structural members. In Table 6, shear capacity control of different cross-sections is presented. From the details in structural design project, beams and columns have single hoop stirrups (8 mm diameter) with 250 mm and 200 mm spacing as shear reinforcements, respectively. The results show that design shear forces do not exceed the calculated shear capacity for all the members considered.

The damage levels of beams under PushX and PushY cases are given in Tables 4 and 5. Abbreviations used are; "LD" for Light damage level, "MD" for Moderate damage level, "HD" for Heavy damage level and "CL" for collapse damage level.

It has been observed that for PushX case, all of the beams are in "Light Damage Level". In PushY case, B117, B217, B222 and B317 beams are in "Moderate Damage Level". Other beams are in "Light Damage Level".

Table 4. Performance level of beams under Push X case.

Member	B (m)	H (m)	Hinge No	L_p (m)	θ_p (rad)	ϕ_p	ϕ_y	ϕ_{tot}	ε_c	ε_s	Damage Level (Concrete)	Damage Level (Steel)	Result
B101	0.30	0.60	357H1	0.3	0.000678	0.002261	0.002250	0.004511	0.000248	0.002315	LD	LD	LD
			357H2	-	-	-	-	-	-	-	-	-	
B104	0.25	0.50	306H1	0.25	0.000182	0.000726	0.002727	0.003453	0.000207	0.001415	LD	LD	LD
			306H2	-	-	-	-	-	-	-	-	-	
B106	0.30	0.70	223H1	0.35	-	-	-	-	-	-	-	-	LD
			223H2	0.35	0.000883	0.002523	0.002185	0.004708	0.000567	0.002347	LD	LD	
B107	0.30	0.70	246H1	-	-	-	-	-	-	-	-	-	LD
			246H2	0.35	0.001368	0.003909	0.002185	0.006094	0.000902	0.005404	LD	LD	
B110	0.30	0.70	352H1	0.35	0.000837	0.002392	0.001859	0.004251	0.000330	0.005379	LD	LD	LD
			352H2	-	-	-	-	-	-	-	-	-	
B201	0.30	0.60	26H1	0.3	0.000857	0.002856	0.002250	0.005106	0.000248	0.002315	LD	LD	LD
			26H2	-	-	-	-	-	-	-	-	-	
B204	0.25	0.50	17H1	0.25	0.000208	0.000832	0.002727	0.003559	0.000207	0.001474	LD	LD	LD
			17H2	-	-	-	-	-	-	-	-	-	
B206	0.30	0.70	4H1	-	-	-	-	-	-	-	-	-	LD
			4H2	0.35	0.000808	0.002309	0.002185	0.004494	0.000567	0.002347	LD	LD	
B207	0.30	0.70	2H1	-	-	-	-	-	-	-	-	-	LD
			2H2	0.35	0.001232	0.003520	0.002185	0.005705	0.000567	0.002347	LD	LD	
B210	0.30	0.70	21H1	0.35	0.001057	0.003020	0.001859	0.004879	0.000330	0.005379	LD	LD	LD
			21H2	-	-	-	-	-	-	-	-	-	
B301	0.30	0.60	58H1	0.3	0.000665	0.002215	0.002250	0.004465	0.000248	0.002315	LD	LD	LD
			58H2	-	-	-	-	-	-	-	-	-	
B304	0.25	0.50	49H1	0.25	0.000078	0.000312	0.002727	0.003039	0.000189	0.001231	LD	LD	LD
			49H2	-	-	-	-	-	-	-	-	-	
B306	0.30	0.70	36H1	-	-	-	-	-	-	-	-	-	LD
			36H2	0.35	0.000042	0.000120	0.002185	0.002305	0.000380	0.001193	LD	LD	
B310	0.30	0.70	53H1	0.35	0.001052	0.003006	0.001859	0.004865	0.000330	0.005379	LD	LD	LD
			53H2	-	-	-	-	-	-	-	-	-	
B315	0.30	0.70	37H1	0.35	0.000107	0.000306	0.001895	0.002201	0.000181	0.001293	LD	LD	LD
			37H2	-	-	-	-	-	-	-	-	-	

In order to evaluate the seismic performance of columns, axial force-total curvature diagrams were established by indicating the previously mentioned damage limits. Seismic performance level of columns with axial force-total curvature diagrams is given in Fig. 15. From the pushover analysis, there is only one plastic hinge mechanism observed under PushX case at C307 column which is in Light Damage level. For PushY case, there are many plastic hinge mechanisms observed. Note that the figures represent results for seven different types of columns. The damage levels of columns under PushX and PushY cases are given in Table 6. As presented in Table 6, damage level for all the columns was determined as "Light Damage" level.

Table 5. Performance level of beams under Push Y case.

Member	B (m)	H (m)	Hinge No	L_p (m)	θ_p (rad)	ϕ_p	ϕ_y	ϕ_{tot}	ε_c	ε_s	Damage Level (Concrete)	Damage Level (Steel)	Result
B101	0.30	0.60	357H1	0.3	0.000248	0.000827	0.002250	0.003077	0.000205	0.001537	LD	LD	LD
			357H2	0.3	0.000066	0.000220	0.002424	0.002644	0.000284	0.001247	LD	LD	
B102	0.30	0.60	358H1	-	-	-	-	-	-	-	-	-	LD
			358H2	0.3	0.000164	0.000547	0.002250	0.002797	0.000195	0.001394	LD	LD	
B104	0.25	0.50	306H1	0.25	0.000904	0.003616	0.002992	0.006608	0.000437	0.002379	LD	LD	LD
			306H2	0.25	0.001407	0.005628	0.002727	0.008355	0.000365	0.005446	LD	LD	
B105	0.25	0.50	307H1	0.25	0.000220	0.000880	0.002727	0.003607	0.000214	0.001510	LD	LD	LD
			307H2	0.25	0.001050	0.004200	0.002992	0.007192	0.000437	0.002379	LD	LD	
B113	0.30	0.70	390H1	0.35	0.001875	0.005357	0.001859	0.007216	0.000330	0.005379	LD	LD	LD
			390H2	0.35	0.000850	0.002429	0.002458	0.004887	0.000860	0.002412	LD	LD	
B114	0.30	0.70	391H1	0.35	0.001311	0.003746	0.001859	0.005605	0.000330	0.005379	LD	LD	LD
			391H2	-	-	-	-	-	-	-	-	-	
B115	0.30	0.70	294H1	0.35	0.001937	0.005534	0.001895	0.007429	0.000400	0.005386	LD	LD	LD
			294H2	0.35	0.002883	0.008237	0.002099	0.010336	0.000831	0.006372	LD	LD	
B116	0.25	0.50	295H1	0.25	0.002145	0.008580	0.002727	0.011307	0.000365	0.005446	LD	LD	LD
			295H2	0.25	0.001062	0.004248	0.002992	0.007240	0.000437	0.002379	LD	LD	
B117	0.25	0.50	296H1	0.25	0.002835	0.011340	0.002727	0.014067	0.000444	0.008643	LD	LD	MD
			296H2	0.25	0.004958	0.019832	0.002992	0.022824	0.000991	0.011800	LD	MD	
B118	0.30	0.70	132H1	0.35	0.002461	0.007031	0.001895	0.008926	0.000400	0.005386	LD	LD	LD
			132H2	0.35	0.002320	0.006629	0.002099	0.008728	0.000831	0.006372	LD	LD	
B119	0.25	0.50	86H1	0.25	0.000306	0.001224	0.002860	0.004084	0.000462	0.005497	LD	LD	LD
			86H2	-	-	-	-	-	-	-	-	-	
B120	0.25	0.50	299H1	0.25	0.001055	0.004220	0.002860	0.007080	0.000462	0.005497	LD	LD	LD
			299H2	0.25	0.001833	0.007332	0.003320	0.010652	0.000930	0.005446	LD	LD	
B121	0.25	0.50	300H1	0.25	0.002075	0.008300	0.002727	0.011027	0.000365	0.005446	LD	LD	LD
			300H2	0.25	0.000783	0.003132	0.002992	0.006124	0.000437	0.002379	LD	LD	
B122	0.25	0.50	301H1	0.25	0.002403	0.009612	0.002727	0.012339	0.000365	0.005446	LD	LD	LD
			301H2	0.25	0.004586	0.018344	0.002992	0.021336	0.000810	0.008653	LD	LD	
B123	0.30	0.70	392H1	0.35	0.002224	0.006354	0.001859	0.008213	0.000330	0.005379	LD	LD	LD
			392H2	0.35	0.000586	0.001674	0.002458	0.004132	0.000765	0.002049	LD	LD	
B124	0.30	0.70	393H1	0.35	0.001519	0.004340	0.001859	0.006199	0.000330	0.005379	LD	LD	LD
			393H2	0.35	0.000501	0.001431	0.002458	0.003889	0.000728	0.001890	LD	LD	
B201	0.30	0.60	26H1	0.3	0.000331	0.001103	0.002250	0.003353	0.000215	0.001682	LD	LD	LD
			26H2	0.3	0.000191	0.000637	0.002424	0.003061	0.000299	0.001450	LD	LD	
B202	0.30	0.60	27H1	-	-	-	-	-	-	-	-	-	LD
			27H2	0.3	0.000300	0.001000	0.002250	0.003250	0.000202	0.001643	LD	LD	
B204	0.25	0.50	17H1	0.25	0.000691	0.002764	0.002992	0.005756	0.000422	0.002281	LD	LD	LD
			17H2	0.25	0.001230	0.004920	0.002727	0.007647	0.000365	0.005446	LD	LD	
B205	0.25	0.50	18H1	0.25	0.000121	0.000484	0.002727	0.003211	0.000197	0.001324	LD	LD	LD
			18H2	0.25	0.000887	0.003548	0.002992	0.006540	0.000437	0.002379	LD	LD	
B213	0.30	0.70	29H1	0.35	0.001673	0.004780	0.001859	0.006639	0.000330	0.005379	LD	LD	LD
			29H2	-	-	-	-	-	-	-	-	-	

Table 5 contd. Performance level of beams under Push Y case.

Member	B (m)	H (m)	Hinge No	L_p (m)	θ_p (rad)	ϕ_p	ϕ_y	ϕ_{tot}	ε_c	ε_s	Damage Level (Concrete)	Damage Level (Steel)	Result
B214	0.30	0.70	30H1	0.35	0.000085	0.000243	0.001859	0.002102	0.000157	0.001277	LD	LD	LD
			30H2	-	-	-	-	-	-	-	-	-	
B215	0.30	0.70	5H1	0.35	0.001878	0.005366	0.001895	0.007261	0.000400	0.005386	LD	LD	LD
			5H2	0.35	0.002291	0.006546	0.002099	0.008645	0.000831	0.006372	LD	LD	
B216	0.25	0.50	6H1	0.25	0.001841	0.007364	0.002727	0.010091	0.000365	0.005446	LD	LD	LD
			6H2	0.25	0.000691	0.002764	0.002992	0.005756	0.000422	0.002281	LD	LD	
B217	0.25	0.50	7H1	0.25	0.002268	0.009072	0.002727	0.011799	0.000365	0.005446	LD	LD	MD
			7H2	0.25	0.005033	0.020132	0.002992	0.023124	0.000991	0.011800	LD	MD	
B218	0.30	0.70	1H1	0.35	0.002259	0.006454	0.001895	0.008349	0.000400	0.005386	LD	LD	LD
			1H2	0.35	0.001707	0.004877	0.002099	0.006976	0.000831	0.006372	LD	LD	
B219	0.25	0.50	3H1	0.25	0.000138	0.000552	0.002860	0.003412	0.000319	0.002364	LD	LD	LD
			3H2	-	-	-	-	-	-	-	-	-	
B220	0.25	0.50	10H1	0.25	0.000804	0.003216	0.002860	0.006076	0.000462	0.005497	LD	LD	LD
			10H2	0.25	0.001268	0.005072	0.003320	0.008392	0.000930	0.005446	LD	LD	
B221	0.25	0.50	11H1	0.25	0.001911	0.007644	0.002727	0.010371	0.000365	0.005446	LD	LD	LD
			11H2	0.25	0.000648	0.002592	0.002992	0.005584	0.000422	0.002281	LD	LD	
B222	0.25	0.50	12H1	0.25	0.002098	0.008392	0.002727	0.011119	0.000365	0.005446	LD	LD	MD
			12H2	0.25	0.004629	0.018516	0.002992	0.021508	0.000991	0.011800	LD	MD	
B223	0.30	0.70	31H1	0.35	0.001752	0.005006	0.001859	0.006865	0.000330	0.005379	LD	LD	LD
			31H2	-	-	-	-	-	-	-	-	-	
B224	0.30	0.70	32H1	0.35	0.000602	0.001720	0.001859	0.003579	0.000215	0.002158	LD	LD	LD
			32H2	-	-	-	-	-	-	-	-	-	
B301	0.30	0.60	58H1	0.3	0.000201	0.000670	0.002250	0.002920	0.000197	0.001495	LD	LD	LD
			58H2	0.3	0.000068	0.000227	0.002424	0.002651	0.000284	0.001247	LD	LD	
B304	0.25	0.50	49H1	0.25	0.000529	0.002116	0.002992	0.005108	0.000413	0.002009	LD	LD	LD
			49H2	0.25	0.001223	0.004892	0.002727	0.007619	0.000365	0.005446	LD	LD	
B305	0.25	0.50	50H1	0.25	0.000106	0.000424	0.002727	0.003151	0.000186	0.001284	LD	LD	LD
			50H2	0.25	0.000945	0.003780	0.002992	0.006772	0.000437	0.002379	LD	LD	
B313	0.30	0.70	61H1	0.35	0.001075	0.003071	0.001859	0.004930	0.000330	0.005379	LD	LD	LD
			61H2	-	-	-	-	-	-	-	-	-	
B315	0.30	0.70	37H1	0.35	0.001432	0.004091	0.001895	0.005986	0.000400	0.005386	LD	LD	LD
			37H2	0.35	-	-	-	-	-	-	-	-	
B317	0.25	0.50	39H1	0.25	0.000839	0.003356	0.002727	0.006083	0.000243	0.002292	LD	LD	MD
			39H2	0.25	0.004504	0.018016	0.002992	0.021008	0.000991	0.011800	LD	MD	
B318	0.30	0.70	33H1	0.35	0.001037	0.002963	0.001895	0.004858	0.000400	0.005386	LD	LD	LD
			33H2	0.35	-	-	-	-	-	-	-	-	
B322	0.25	0.50	44H1	0.25	0.000867	0.003468	0.002727	0.006195	0.000243	0.002292	LD	LD	LD
			44H2	0.25	0.004188	0.016752	0.002992	0.019744	0.000810	0.008653	LD	LD	
B323	0.30	0.70	63H1	0.35	0.000792	0.002263	0.001859	0.004122	0.000330	0.005379	LD	LD	LD
			63H2	-	-	-	-	-	-	-	-	-	

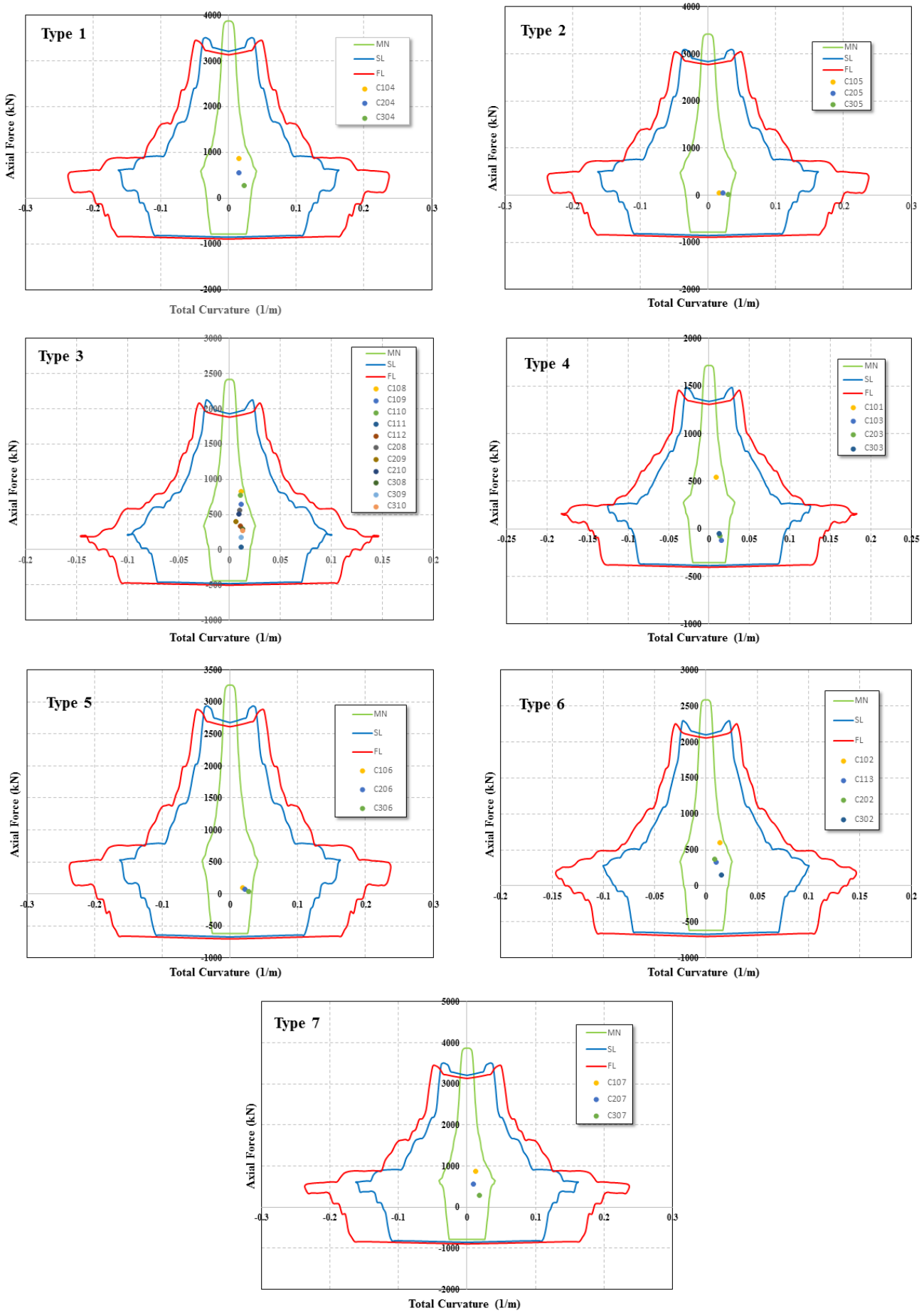

Fig. 15. Performance level evaluation of columns.

Table 6. Performance level of columns.

Member	P (kN)	B (m)	H (m)	Hinge No	L_p (m)	θ_p (rad)	ϕ_p	ϕ_y	ϕ_{tot}	Result
C101	538.93	0.25	0.50	270H1	0.25	0.001164	0.004656	0.004277	0.008933	LD
				270H2	-	-	-	-	-	
C102	595.59	0.30	0.60	274H1	0.15	0.000736	0.004907	0.008646	0.013553	LD
				274H2	-	-	-	-	-	
C103	117.48 (T)	0.25	0.50	266H1	0.25	0.003177	0.012708	0.002762	0.015470	LD
				266H2	0.25	0.002377	0.009508	0.002762	0.012270	
C104	860.18	0.70	0.40	250H1	0.20	0.001934	0.009670	0.006110	0.015780	LD
				250H2	0.20	0.000015	0.000075	0.006110	0.006185	
C105	55.93	0.60	0.40	254H1	0.20	0.002467	0.012335	0.004374	0.016709	LD
				254H2	0.20	0.002267	0.011335	0.004374	0.015709	
C106	93.52	0.60	0.40	258H1	0.20	0.002563	0.012815	0.004337	0.017152	LD
				258H2	0.20	0.002802	0.014010	0.004337	0.018347	
C107	877.94	0.70	0.40	262H1	0.20	0.001294	0.006470	0.006159	0.012629	LD
				262H2	-	-	-	-	-	
C108	825.90	0.30	0.60	237H1	0.30	0.002397	0.007990	0.003323	0.011313	LD
				237H2	-	-	-	-	-	
C109	641.76	0.30	0.60	241H1	0.30	0.002207	0.007357	0.004013	0.011370	LD
				241H2	-	-	-	-	-	
C110	770.62	0.30	0.60	245H1	0.30	0.002224	0.007413	0.003491	0.010904	LD
				245H2	-	-	-	-	-	
C111	39.15	0.30	0.60	225H1	0.30	0.002553	0.008510	0.002679	0.011189	LD
				225H2	-	-	-	-	-	
C112	334.01	0.30	0.60	229H1	0.15	0.000504	0.003360	0.007244	0.010604	LD
				229H2	-	-	-	-	-	
C113	326.97	0.30	0.60	233H1	0.15	0.000370	0.002467	0.007391	0.009858	LD
				233H2	-	-	-	-	-	
C202	366.22	0.30	0.60	275H1	-	-	-	-	-	LD
				275H2	0.15	0.000086	0.000573	0.007593	0.008166	
C203	74.62 (T)	0.25	0.50	267H1	0.25	0.002603	0.010412	0.002942	0.013354	LD
				267H2	0.25	0.002425	0.009700	0.002942	0.012642	
C204	560.89	0.70	0.40	251H1	0.20	0.000504	0.002520	0.005323	0.007843	LD
				251H2	0.20	0.001928	0.009640	0.005323	0.014963	
C205	43.53	0.60	0.40	255H1	0.20	0.002636	0.013180	0.004354	0.017534	LD
				255H2	0.20	0.003489	0.017445	0.004354	0.021799	
C206	76.31	0.60	0.40	259H1	0.20	0.003264	0.016320	0.004307	0.020627	LD
				259H2	0.20	0.003618	0.018090	0.004307	0.022397	
C207	558.21	0.70	0.40	263H1	-	-	-	-	-	LD
				263H2	0.20	0.000777	0.003885	0.005334	0.009219	
C208	558.36	0.30	0.60	238H1	0.15	0.000002	0.000014	0.008392	0.008406	LD
				238H2	0.15	0.000262	0.001747	0.008392	0.010139	
C209	403.17	0.30	0.60	242H1	0.30	0.000006	0.000020	0.003497	0.003517	LD
				242H2	0.30	0.000732	0.002440	0.003497	0.005937	
C210	509.00	0.30	0.60	247H1	-	-	-	-	-	LD
				247H2	0.15	0.000215	0.001433	0.008138	0.009571	

Table 6 contd. Performance level of columns.

Member	P (kN)	B (m)	H (m)	Hinge No	L_p (m)	θ_p (rad)	ϕ_p	ϕ_y	ϕ_{tot}	Result
C302	155.33	0.30	0.60	276H1	-	-	-	-	-	LD
				276H2	0.15	0.001248	0.008320	0.006641	0.014961	
C303	48.62 (T)	0.25	0.50	268H1	0.25	0.001958	0.007832	0.003053	0.010885	LD
				268H2	0.25	0.002389	0.009556	0.003053	0.012609	
C304	272.12	0.70	0.40	252H1	0.20	0.002105	0.010525	0.004728	0.015253	LD
				252H2	0.20	0.003594	0.017970	0.004728	0.022698	
C305	22.89	0.60	0.40	256H1	0.20	0.003827	0.019135	0.004306	0.023441	LD
				256H2	0.20	0.005194	0.025970	0.004306	0.030276	
C306	38.52	0.60	0.40	260H1	0.20	0.003404	0.017020	0.004181	0.021201	LD
				260H2	0.20	0.004685	0.023425	0.004181	0.027606	
C307	288.91	0.70	0.40	264H1	0.20	0.001154	0.005770	0.004774	0.010544	LD
				264H2	0.20	0.002676	0.013380	0.004774	0.018154	
C308	291.96	0.30	0.60	239H1	0.30	0.000256	0.000853	0.003225	0.004078	LD
				239H2	0.30	0.002950	0.009833	0.003225	0.013058	
C309	179.03	0.30	0.60	243H1	0.30	0.000469	0.001563	0.002992	0.004555	LD
				243H2	0.30	0.002586	0.008620	0.002992	0.011612	
C310	266.88	0.30	0.60	248H1	0.15	0.000088	0.000587	0.006918	0.007505	LD
				248H2	0.15	0.000918	0.006120	0.006918	0.013038	

6. Conclusions

A school building was totally collapsed during the 2011 Van earthquake. In this paper, a numerical model was created considering projects and in-situ investigations made after earthquake. In accordance with Turkish Seismic Code (TSC, 2007), pushover analyses were performed and expected member by member damage levels and overall structural damage were determined. According to numerical results, the expected member damage levels of columns, beam and shear walls are less than or equal to the moderate damage level given in the code. Additionally, the expected overall structural earthquake performance according to Turkish Seismic Code (TSC, 2007) is life safety. These numerical results are completely different from the actual case. The analyses carried out in this study, clearly showed that the school building would not have partially collapsed, if it had been properly constructed as planned during design phase. As explained in detail above, the violation of reinforcement detailing rules as well as use of poor quality of concrete seem to be the main reason of actual damage. It should be noted that available earthquake performance assessment methodologies do not consider this type of local deficiencies that can cause partial or total collapse. In order to prevent similar potential future catastrophic consequences, it is strongly recommended that local problems should be taken into consideration in the seismic performance assessment procedures. For doing that, more information is needed on the behavior of substandard existing structural members and their connections which fail through various mechanisms due to poor reinforcement detailing and low-quality concrete. Since there are only limited studies on this type of behavior, the inclusion of effects of these local deficiencies on structural modelling is not taken into the scope of the current study.

Acknowledgements

Our sincere appreciations and gratitude go to our colleagues Nilgün Merve ÇAĞLAR and Alper İLKİ for their supports during the construction of this study.

References

AFAD (n.d.). Turkish Prime Ministry Disaster and Emergency Management Presidency. Retrieved from http://www.afad.gov.tr

Bedirhanoglu I, Ilki A, Pujol S, Kumbasar N (2010). Behavior of deficient joints with plain bars and low-strength concrete. *ACI Structural Journal*, 107(3), 300–310.

Carvalho G, Bento R, Bhatt C (2013). Nonlinear static and dynamic analyses of reinforced concrete buildings – comparison of different modelling approaches. *Earthquakes and Structures, An Int'l Journal*, 4(5), 451–470.

Cosgun C, Dindar AA, Seckin E, Onen Y (2013). Analysis of building damage caused by earthquake in Eastern Turkey. *Gradevinar*, 65(8), 743–752.

CSI (2016). SAP2000. Analysis Reference Manual. CSI: Berkeley (CA, USA): Computers and Structures INC.

Ilki A, Demir C, Bedirhanoglu I, Kumbasar N (2009). Seismic retrofit of brittle and low strength RC columns using fiber reinforced polymer

and cementitious composites. *Advances in Structural Engineering*, 12(3), 325–347.

IMBSEN software systems (2004). XTRACT V3.0.1.: Cross sectional structural analysis of components.

Inel M, Meral E (2016). Seismic performance of RC buildings subjected to past earthquakes in Turkey. *Eartquakes and Structures, An Int'l Journal*, 11(3), 483–503.

Isik E, Kutanis M (2015). Performance based assessment for existing residential buildings in Lake Van basin and seismicity of the region. *Earthquakes and Structures, An Int'l Journal*, 9(4), 893–910.

Mander JB, Priestley MJN, Park R (1988). Observed stress-strain behavior of confined concrete. *Journal of Structural Engineering*, 114(8), 1827–1849.

Ni P (2014). Seismic assessment and retrofitting of existing structure based on nonlinear static analysis. *Structural Engineering and Mechanics*, 49(5), 631–644.

Palermo P, Hernandez RR, Mazzoni S, Trombetti T (2014). On the seismic behavior of a reinforced concrete building with masonry infills collapsed during the 2009 L'Aquila earthquake. *Earthquakes and Structures, An Int'l Journal*, 6(1), 45–69.

Tapan M, Comert M, Demir C, Sayan Y, Orakcal K, Ilki A (2013). Failures of structures during the October 23, 2011 Tabanlı (Van) and November 9, 2011 Edremit (Van) earthquakes in Turkey. *Engineering Failure Analysis*, 34, 606–628.

TSC (2007). Turkish Earthquake Resistant Design Code (TSC). Ministry of Public Works and Settlement. Ankara.

Turk M, Comert M, Cosgun C (2013). Seismic upgrade of RC buildings using CFRP sheets. *Gradevinar*, 65(5), 435–448.

Yön B, Sayın E, Köksal TS (2013). Seismic response of buildings during the May 19, 2011 Simav, Turkey earthquake. *Earthquakes and Structures, An Int'l Journal*, 5(3), 343–357.